RICE UNIVERSITY

Studies of Low Luminosity Active Galactic Nuclei with Monte Carlo and Magnetohydrodynamic Simulations

by

Guy Louis Hilburn

A THESIS SUBMITTED
IN PARTIAL FULFILLMENT OF THE
REQUIREMENTS FOR THE DEGREE

Doctor of Philosophy

APPROVED, THESIS COMMITTEE:

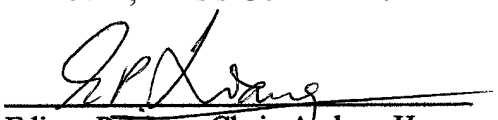

Edison P. Liang, Chair, Andrew Hays Buchanan Professor of Astrophysics and Department Associate Chair

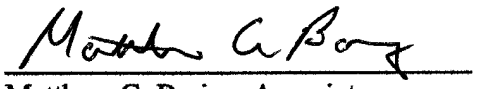

Matthew G. Baring, Associate Professor of Physics and Astronomy

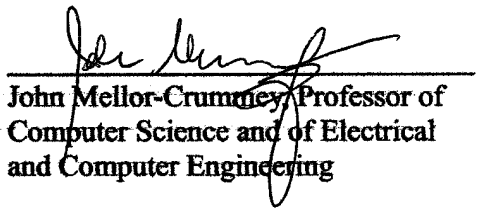

John Mellor-Crummey, Professor of Computer Science and of Electrical and Computer Engineering

HOUSTON, TEXAS
APRIL 2012

Abstract

Studies of Low Luminosity Active Galactic Nuclei with Monte Carlo and Magnetohydrodynamic Simulations

by

Guy Hilburn

Results from several studies are presented which detail explorations of the physical and spectral properties of low luminosity active galactic nuclei. An initial Sagittarius A* general relativistic magnetohydrodynamic simulation and Monte Carlo radiation transport model suggests accretion rate changes as the dominant flaring method. A similar study on M87 introduces new methods to the Monte Carlo model for increased consistency in highly energetic sources. Again, accretion rate variation seems most appropriate to explain spectral transients. To more closely resolve the methods of particle energization in active galactic nuclei accretion disks, a series of localized shearing box simulations explores the effect of numerical resolution on the development of current sheets. A particular focus on numerically describing converged current sheet formation will provide new methods for consideration of turbulence in accretion disks.

Acknowledgments

First and foremost, I must thank my advisor, Professor Edison Liang. For six years, he has dealt with my ignorant questions, strange hours, and remarkable ability to make all things more difficult than they should be. His patience, guidance, and compassion make him a wonderful professor, and I am incredibly proud to call him my advisor and friend. I am very grateful to each member of my graduate and dissertation committees, Edison Liang, Matthew Baring, Frank Geurts, and John Mellor-Crummey. The amount of time they have taken to ensure I remained on the right track, up until my thesis submission, has been extraordinary, and their patience and criticisms helped shape this work almost as much as my own efforts have.

My friends and family have stoically dealt with all of the hardships that graduate student life can bring about, and haven't faltered a step in supporting me. My wife Kelsey, mother Alma, father Jack, sister Beth, and extended family Daniel, James, Linda, Layne, Elissa, and Greg, have all played roles more central to my well-being than I could have ever imagined. They are my support group, and I love them all dearly.

Within the field, I've been helped by a number of individuals, through discussions, sharing of techniques and data, and inspiration. This list includes Xuhui Chen, Charles Gammie, Markus Böttcher, Justin Finke, Dan Harris, Francesco Massaro, Feng Yuan, and many others. I owe particular thanks to Hui Li, for inviting me to work at Los Alamos and Siming Liu, who started me on the path that led to these projects.

Table of Contents

List of Tables

List of Figures

Preface

Chapters 3 and 4 have been published in *Montly Notices of the Royal Astronomical Society* and *Astrophysical Journal*, respectively, in slightly different formats (Hilburn et al. 2010; Hilburn and Liang 2012).

This work was supported in part by NSF under Grant AST-0909167, by the Data Analysis and Visualization Cyberinfrastructure funded by NSF under Grant OCI-0959097, by the Cyberinfrastructure for Computational Research funded by NSF under Grant CNS-0821727, by the Shared University Grid at Rice funded by NSF under Grant EIA-0216468, and by a partnership between Rice University, Sun Microsystems, and Sigma Solutions, Inc.

Chapter 1

Introduction - Historical and Background Information on Active Galactic Nuclei

This dissertation will present modeling projects undertaken to explain the physical and radiative phenomena associated with low luminosity active galactic nuclei (LLAGN). This process involves the consideration of two specific sources, Sagittarius A* (Sgr A*), our Galactic Center, and M87, also known as Virgo A or NGC 4486. Modeling tools include a general relativistic magnetohydrodynamic (GRMHD) code to describe the global physical properties of active galactic nuclei (AGN) surroundings, a Monte Carlo (MC) radiation transport code to calculate a region's emissions based on its physical parameters, and an MHD shearing box simulation to study the local properties of these sources.

Within this introductory chapter, Section 1.1 lays out the historical background of AGN theory and observations. Section 1.2 discusses the two specific LLAGN that are modeled in detail in later chapters. Section 1.3 then explains the state of AGN modeling and its progression through the years. Finally, Section 1.4 will present the projects in this dissertation and elaborate on its layout.

1.1 Historical Literature on Active Galactic Nuclei

The studies of active galactic nuclei, radiative sources commonly associated with accretion onto and outflow from supermassive black holes in the centers of galaxies, have been ongoing for about a century. Early studies demonstrated that galactic nuclei could show distinct emission-line spectra, which led to a number of attempts to classify these

peculiar sources before the physical properties of their origins were completely understood. The true birth of AGN studies came with the advent of radio astronomy, as early as the 1930's, and progressed with each advancement in telescope technology that allowed the investigation of new radiative regimes, such as infrared and X-ray.

Fath (1909) constructed a new spectrograph to be used at Lick Observatory with the intent of studying distant galaxies, or "spiral nebulae", to determine whether they showed continuous spectra, suggesting they were a collection of discrete stars, or bright line spectra, as gaseous nebulae do. Most of these sources displayed spectra which were consistent with that of a collection of stars, but NGC 1068 showed bright emission lines and absorption lines, as would be seen in a nebula. This was confirmed by Slipher (1917) at Lowell Observatory, with a more resolving spectrograph which showed the emission lines were spread over a range of wavelengths, though at the time, he didn't connect this phenomena with radial velocity dispersion. These studies of galaxies with emission-line nuclei continued, with, for instance, Hubble (1926) noting that spirals with stellar nuclei showed a spectrum similar to that of a planetary nebula, including several now known to harbor AGN: NGC 1068, 4051, and 4151.

The notable survey conducted by Seyfert (1943) found six of these type of sources, which displayed a variety of greatly broadened forbidden and/or permitted lines. This was attributed to Doppler shifts which reached ~ 8500 km/s for the broadest lines. Though this didn't directly lead to the study of AGN as a major topic, these galaxies with high-excitation lined nuclear emission came to be known as "Seyfert galaxies".

In the 1930's, in order to try to pinpoint sources of static which interfere with radio transmissions, Karl Jansky (1932, 1933, 1935) constructed the first basic radio

telescope. His findings showed a constant source of "static" from the disk of the Milky Way, which was strongest toward the Galactic Center. This led to some interest in using radio instruments to conduct observations of the sky, with Reber (1940a, 1940b, 1944) mapping the radio sky, noting several radio sources which stood out compared to their environment. He also found that in general, the ratio of radio to optical radiation was much greater for the rest of the Milky Way, than for the sun.

These findings caused a number of academic groups to take notice of the possibilities associated with radio astronomy. Bolton (1948) cataloged several discrete radio sources and gave them now-familiar names, such as Cygnus A, a source now associated with an AGN, and Cassiopeia A, the strongest radio source on the sky outside of our solar system, a supernova remnant. His group went on to publish optical identifications of discrete sources for the first time, from previously detected radio sources, including M87 (Virgo A) and NGC 5128 (Centaurus A), important AGN for current study (Bolton, Stanley, and Slee 1949).

In the early 1950's, the group of Ryle, Smith, and Elsmore (1950) produced a radio survey with more accurate measurements than was previously done, leading to Smith (1951) publishing better positions for several specific sources: Taurus A, Virgo A, Cygnus A, and Cassiopeia A. This allowed Baade and Minkowski (1954) to locate these sources with optical techniques. Their observations suggested that Cygnus A was an irregularly shaped source. They calculated emission line spectra, leading to redshift and distance figures which implied huge radio and optical luminosities of $\sim 8 \times 10^{42}$ erg/s and $\sim 6 \times 10^{42}$ erg/s, respectively. This was the first hint that these sources may be of previously unobserved strength.

Around this same time, Hanbury Brown, Jennison, and Das Gupta (1952) studied Cygnus A with a new type of interferometer, which again showed an elongated shape. This was clarified by Jennison and Das Gupta (1953) showing that it was actually two radio components spaced around an optical center - a shape which was shown later to be common for these extragalactic radio sources. Later in this decade, the same group began to suggest categorizing these radio sources as 'Class I', which were associated with the plane of the Milky Way, and 'Class II', which were uniformly distributed on the sky, and therefore possibly extragalactic (Hanbury Brown 1959). Some of the Class II sources had very small angular sizes, which encouraged the thinking at the time that they may be "radio stars" in the Milky Way.

As these observing campaigns were underway, other groups were attempting to explain both the source of the Galactic radio background and the strength of observed radio sources. After a number of papers on the subject, Kiepenhauer (1950) extended a basic suggestion that both may be due to synchrotron emission, to a theory that the Galactic radio background may be due to synchrotron emission by the general Galactic magnetic field. The idea that the dominant radio emission mechanism is synchrotron was discussed and then widely accepted by the end of the decade. For the double-lobed radio galaxies discussed previously, this would suggest enormous amounts of energy, up to ~ 10^{60} ergs (Burbidge 1959). De Young and Axford (1967) postulated that these shapes arose due to ram pressure as streams of material tried to expand into the intergalactic medium, a predecessor of the jet idea.

1.1.1 Quasar Discovery and Study

The further study of "radio stars" led to an important step in the theoretical framework of AGN. Matthews et al. (1961) reported on one of these, 3C 48, which showed a degree of variability, an excess in the UV, and broad emission lines, though at wavelengths which were unfamiliar. This was found to be similar to several other star-like sources which were coincident with radio sources. Due to these features, these "radio stars" became known as quasi-stellar radio sources (QSRS), or quasars. At the time there was general agreement that these were nearby stars, though with strange properties.

One of these, 3C 273, was studied more closely by Hazard, Mackey, and Shimmins (1963), who found that the source seemed to have two components: a star-like object, with a faint jet component. Schmidt (1963) obtained more detailed spectra, which again showed unfamiliar broad lines, at different wavelengths than those in 3C 48. Further study revealed that these lines were spaced very similarly to the hydrogen Balmer series, which would suggest a redshift of $z = 0.16$ for the source. The same process was quickly applied to the spectrum of 3C 48, which yielded a redshift of $z = 0.37$ (Greenstein and Matthews 1963; Oke 1963; Hazard, Mackey, and Shimmins 1963). These results could be due to redshifts from galactic stars with very high densities, though this didn't explain the width of the lines. The most reasonable explanation was therefore that the redshifts were due to Hubble expansion, which would make the objects extragalactic. Using this theory, the redshift of 3C 273 suggested a nuclear region less than 1 kpc in diameter, with a jet 50 kpc away, and a total radiative energy above 10^{59} ergs. Some of the mysteries of quasars had been solved, though many questions were still open about the nature of these curious sources.

The following year, Greenstein and Schmidt (1964) conducted a more thorough study of 3C 48 and 3C 273, analyzing several possibilities for the observed redshift. They used the lack of observed proper motions to rule out the likelihood of movement within the Milky Way causing the phenomenon, and the strongly symmetric emission lines to discount gravitational redshifts. This left the possibility that the objects were extragalactic, with cosmological expansion causing the redshifts. Assuming this, other constraints would suggest objects of at least 10^9 solar masses. They went on to suggest a model with a compact source of optical continuum surrounded by emission-line regions, and an even larger region of radio emission. These sources could be strong enough to swamp emissions from their host galaxies. These are all important features in modern theories of AGN.

The following years brought a huge amount of new literature analyzing the properties of quasars and similar objects. Sandage (1965) reported on the discovery of objects which are radio quiet but generally are spectrally similar to quasars, which included "blue stellar objects" (BSO) or "quasi-stellar galaxies" (QSG), which seemed to outnumber quasars dramatically. Importantly for theory, Greenstein and Schmidt (1967) observed multiple redshifts within single objects, which they postulated could be due to a composition of in-falling and out-flowing matter.

The advent of X-ray observations quickly showed that they would be vital for studies of AGN. Friedman and Byram (1967) started this with the first X-ray AGN discovery, observing M87. Subsequent papers by Bowyer et al. (1970), Gursky et al. (1971), and Tananbaum et al. (1979) demonstrated the importance of studying AGN in X-rays, with luminosities in the band for sources ranging from $\sim 10^{42}$ to 10^{47} erg/s. Marshall

et al. (1981) showed an important facet of X-ray emission from AGN, observing that it tended to vary more than other energy bands. Some sources showed variance on times of one to five days, up to a factor of two, which suggested emissions were from a very compact region near the nucleus.

By the early 1970's, astronomers had generally accepted that quasars were cosmological objects and that Seyfert galaxies and quasars likely had a common physical connection. Literature has attempted to tie these populations together and determine the physical mechanisms at play in generating their immense, multi-wavelength emissions.

1.1.2 Literature Leading to our Current Understanding of AGN

Early in the study of Seyfert galaxies and quasars, some of the pieces of the physical parts of the AGN puzzle began to be assembled. The 1963 papers by Hoyle and Fowler (1963 a,b) seemed to gather a variety of important AGN details before they were widely accepted. They suggested the possibility of a "supermassive star" which would be able to accelerate particles to the kinds of energies required for Seyfert galaxy emissions. These would depend upon a magnetic field threaded through a surrounding disk to provide energy for radiation and jets. Similarly, far ahead of their time, both Salpeter (1964) and Zel'Dovich (1964) proposed that energy production in quasars may be due to accretion onto a supermassive black hole, including the suggestion of a mechanism for turbulent transport of angular momentum. This idea gained support when Lynden-Bell (1969) suggested that black holes should be common in galactic nuclei, and their accretion disks could explain a large amount of the high energy phenomena in astronomy, including Seyfert galaxies, quasars, and other objects associated with galactic nuclei.

Similarly, the ideas leading to our current spectral knowledge of AGN came piecemeal over several decades. Hoyle, Burbidge, and Sargent (1966) pointed out that the broadband continuum could be explained by synchrotron photons being inverse Compton scattered by the hot electrons which produce them originally. In an early example of the development of the unified model, Khachikian and Weedman (1974) proposed separation of the Seyfert galaxies into two classes - 'Seyfert I' having broad wings on nuclear emission lines, and 'Seyfert II' lacking these. In the next decade, Edelson and Malkan (1987) studied the importance of variability in these sources. They showed that in the far infrared, quasars and Seyfert galaxies had variations typically less than 15%, while blazars, a newer class of object dominated at all wavelengths by a strongly polarized, nonthermal continuum, showed variations up to a factor of two.

By this time, the scientific community in general was in acceptance of AGN phenomena being attributed to black holes. As Rees (1984) pointed out, this was due to an accumulation of observational and theoretical arguments, and, specifically, the lack of other viable options.

This time also saw the development of the idea of a Unified Model of AGN classes, which proposes that the variety of objects now classified as AGN can appear dramatically different, largely due to our observation angle to them.

For instance, Blandford and Rees (1978) proposed that BL Lac objects, a subtype of the blazar class, were radio galaxies which were observed down a relativistic jet, rather than from an angle more nearly edge-on. In a similar scenario, Rowan-Robinson (1977) suggested that the broad line-producing region of Seyfert 2 galaxies may be obscured, rather than absent, perhaps by a dusty torus. This, again, would suggest that the

differences may be primarily due to direction of observation.

More tellingly, Antonucci and Miller (1985) showed that the polarized flux of NGC 1068, which is the prototypical Seyfert 2, had the same appearance as a normal Seyfert 1 spectrum. Their interpretation of this was that the broad line region and central source of the continuum were obscured by a dusty torus.

All of these, and many more, pieces of literature served to support a paper by Osterbrock (1978), which proposed these various scenarios in a toroidal geometry, which could then describe radio galaxies, Seyfert galaxies, quasars, and blazars, by simple changes in orientation. It is now generally accepted that this is the true view of AGN, as a broad class which has distinct subclasses due to observation angle. The typical model is of a supermassive black hole surrounded by a dusty torus, flowing into an accretion disk onto the black hole, with axial jets erupting in the polar directions.

The AGN studied within this dissertation are part of a specific subset of AGN known as low luminosity active galactic nuclei. These sources display distinct characteristics largely due to a very low accretion rate. This causes several effects, due to a lack of particle density in the accreting region, with the accretion disks for these objects tending to be less optically thick than similar objects accreting more strongly. Most importantly, the radiative loss is sufficiently low that it can be ignored, to first order, when modeling accretion dynamics. This greatly simplifies the modeling of such objects as radiative output can be modeled by post-processing of radiationless accretion flows. The emerging bremsstrahlung and Compton emissions may be weaker, relative to that of the synchrotron process, due to their larger dependence upon particle density. The actual accretion process can also be largely affected, with plasma having less of a tendency to

build up, and being more strongly advected onto the black hole once coming within its proximity. These differences will be discussed in the context of various models in the modeling Section 1.3.

A number of excellent reviews of AGN literature exist and are highly recommended for a more broad, general overview of the topic. These include papers by Trimble (1992), Urry and Padovani (1995), and Shields (1999), and books by Peterson (1997), Krolik (1998), and Osterbrock and Ferland (2005).

1.2 Observations and Theory of Specific AGN

At this point, focus shifts to specific AGN and their properties. The modeling projects described in Chapters 3 and 4 are focused on Sagittarius A* and M87, respectively, and it is useful to consider how previous literature has developed our current understanding of these objects' spectral and physical properties.

1.2.1 Sagittarius A*

The source at our Galactic Center, Sagittarius A*, is widely accepted to be related to the accretion flow, and possibly outflows, due to a supermassive black hole whose mass is about 4 million solar masses (Ghez et al. 2003; Schödel et al. 2007; Melia 2006).

Sgr A* was first discovered by Balick and Brown (1974) in the radio and near infrared. This started a huge interest in studying this source, as it is clearly the closest AGN available for observations. In radio, groups making measurements included Davies et al. (1976), Backer and Sramek (1982), and Zhao et al. (1989). In the microwave regime, observations have been taken by groups such as Yusef-Zadeh, Morris, and Ekers

(1990), Wright et al. (1987), and Rogers et al. (1994). At higher energies, early groups doing X-ray and gamma ray measurements included Goldwurm et al. (1994) and Merck et al. (1996). Clearly, there are no listings of optical observations. The extinction due to dust along the Galactic plane is so high that optical measurements are essentially impossible. The most interesting and useful measurements of Sgr A* have been taken since the turn of the century. Baganoff et al. (2001, 2003) presented data from the *Chandra* X-ray observatory which described clear variability in the X-ray, suggesting flaring and quiescent states for the source. Also, as data taken during different epochs is hard to reconcile into a full spectrum, groups have also begun conducting multi-wavelength observing campaigns, with the intent of providing contemporaneous data in a number of different energy bands (Eckart et al. 2004, 2006; Bélanger et al. 2005). These campaigns have generally supported the previously suggested spectral states. Xu et al. (2006) postulated that the quiescent state X-ray emission can likely be attributed to thermal emission from the large scale accretion flow.

The general spectral shape is typical of AGN, with a low energy curve which is indicative of synchrotron emission, and a high energy bump in the X-ray, which variability data suggests is of synchrotron origin, upscattered by hot electrons (Liu and Melia 2001; Markoff et al. 2001; Dodds-Eden et al. 2009). A more full depiction of the broadband spectrum, based on these data, is shown in Chapter 3.

Our understanding of the physical parameters of Sgr A* are based on dynamical observations, as well as spectral. Schodel et al. (2002) initially reported on observations of the orbital path of a star near the Galactic Center. Based on 10 years of astrometric data on this star with a 15.2 year orbital period, they suggested a central mass of ~ 3.7 x

10^6 solar masses. This essentially ruled out any explanation aside from a black hole for the concentrated central object. This type of work was refined by Gillessen et al. (2009) who conducted the same type of astrometric research over 16 years. They refined the suggestion for Sgr A*'s mass to ~ 4.3 x 10^6 solar masses, as well as estimating its distance at ~ 8.33 kpc.

True to our understanding of Sgr A* as an LLAGN, its luminosity is about 10^{36} erg, or less than 10^{-8} L_{Edd} (Yuan 2007), and its accretion rate is similarly quite low, around $\dot{m} = \dot{M}/\dot{M}_{Edd} = 10^{-5}$. The Eddington limit is calculated as the point at which radiative pressure outward balances gravitational force inward, and is the typical reference of these sources' luminosity and accretion rate. L_{Edd} and $\dot{M}_{Edd}$ are the luminosity and mass accretion rate, respectively, calculated at this limit.

Until recently, the spin of Sgr A* was thought to be very low, around the minimal a/M = 0 (where 1 indicates a maximally rotating black hole). Recent estimates have varied considerably on this point, with, for example, Broderick et al. (2011) suggesting a/M = 0, Shcherbakov and Penna (2011) finding a/M = 0.7 as the most likely spin fit by their models, and Moscibrodzka et al. (2011) suggesting a spin as high as a/M = 0.9 as the most likely.

1.2.2 M87

Conversely to Sgr A*, M87 has been studied nearly since the birth of radio astronomy. Recent measurements have estimated its mass at about six billion solar masses (Gebhardt and Thomas 2009), and its distance at 16.7 Mpc (Mei et al. 2007). Interestingly, despite being so much more distant than our Galactic Center, its immense

size means it has a very similar angular size to Sgr A*.

The most familiar feature of M87 is its spectacular, kiloparsec-scale jet. Observations of the superluminal motion of features within it have tied the jet viewing angle to $< 19^{o}$ and bulk Lorentz factor $\gamma > 6$, at HST-1, the brightest, and therefore most studied "knot", within the jet (Biretta et al. 1999). This would imply HST-1 is located about 5.3×10^{5} R_s along the jet, where for M87, $R_s = 1.8 \times 10^{15}$ cm (Hardee 2010).

As with Sgr A*, M87's spectrum suggests it is a fairly typical AGN - more specifically, a misaligned BL Lac. Recent years have yielded a greater variety of multi-wavelength collaborations (Acciari et al. 2008, 2010), and, unlike Sgr A*, optical observations are possible. Both optical and x-ray bands show common flaring transients with variability around a factor of two, on timescales of months (Perlman et al. 2003; Harris et al. 2009). As expected, higher energy emissions show greater variability, with gamma rays tending to flare on timescales of days (Aharonian et al. 2006).

The luminosity of M87 is about 10^{-6} L_{Edd}, and there have been a variety of estimates of its accretion rate (Ho 1999). Based on its Compton spectrum, Di Matteo et al. (2003) suggested an upper limit around $\dot{m} = 1.6 \times 10^{-3}$, while Levinson and Rieger (2011), with a calculation based on their calculation of the jet's power and the possible jet power for a maximally accreting source, suggested $\dot{m} = 10^{-4}$.

The spin of M87 has long been thought to be quite high, largely due to the prominence of its jet. Wang et al. (2008) use the gamma ray variability to calculate a spin rate $a/M > 0.65$, and Li et al. (2009) end up with an even higher estimate based on a relativistic hydrodynamic model of $a/M = 0.8$.

1.3 AGN Modeling

Modeling of AGN has progressed from somewhat naive, simplistic accretion disk models calculated analytically, based on a variety of unknown or misunderstood disk properties, to high resolution, highly-consistent, three dimensional simulations which require vast multi-processor facilities to calculate results.

There were several assumptions which were expected to be part of a successful accretion disk model from the beginning of its study. Accreting matter must lose gravitational energy as well as angular momentum, and would be heated viscously, causing it to radiate. It was unclear exactly how angular momentum would be lost by in-falling matter, as that meant angular momentum must be gained by more distant matter, by conservation.

The best-known early model of AGN accretion disk structure was the standard-disk idea, proposed by Shakura and Sunyaev (1973). They suggested that angular momentum transport within the disk was due to turbulence leading to enhanced viscosity, and characterized this viscosity by a dimensionless parameter α. The model was appropriate for sources accreting close to the Eddington limit, leading to an optically thick disk. This encompassed a number of ideas which are still considered integral to AGN studies today, but was hindered by missing knowledge in the actual behavior of a plasma accreting onto a compact object, and is generally unsuitable for application to LLAGN.

1.3.1 Magnetorotational Instability

The answer to the viscosity problem was largely solved by Balbus and Hawley

(1991), who recognized that work done much earlier by Chandrasekhar (1960) and Fricke (1969) had been overlooked by those seeking an explanation for angular momentum transport in accretion disks. These papers had described a strong instability in magnetized fluid with differential motions, which Balbus and Hawley connected to accretion disks, where fluid elements connected by field lines would gain angular momentum when displaced outward, and vice versa. These requirements for this instability are simple to satisfy, needing only a tiny poloidal magnetic field and differential rotation, with rate decreasing from the center, and the growth rate and onset of the instability are largely insensitive to the strength of the field. Due to this, it is likely a ubiquitous process throughout the range of astrophysical accretion disks.

The magnetorotational instability (MRI) is now widely accepted as being responsible for the development of turbulence and, therefore, the turbulence-based "viscosity", which had previously been characterized, but unexplained, in accretion models (Hawley and Balbus 2002; Hawley 2001; Balbus 2003). The models used in this thesis will be MRI-based.

1.3.2 Radiatively Inefficient Accretion Flow

As accretion disk physics is very different from the standard-disk approach when accretion rates are very low, appropriate models were developed for this situation. Largely, they are members of a class referred to as the radiatively inefficient accretion flow (RIAF). In these situations, plasma is likely to be optically thin and diffuse, and emission timescales will be too long to allow for efficient conversion of thermal energy to radiation.

A popular subtype of the RIAF class is known as the advection dominated accretion flow (ADAF), which proposes that in these situations the thermal energy possessed by the plasma is largely advected through the black hole's horizon, without being given time to radiatve significantly (Ichimaru 1977; Rees et al. 1982). These accretion flows would be optically thin and extremely hot, and could likely lead to strong outflows from a significant radius. Outside of the advection zone, the disk is expected to resemble a standard disk, extending for, perhaps thousands of gravitational radii. This type of situation is very likely applicable to Sgr A* and M87, and other LLAGN (Narayan and Yi 1994; Abramowicz et al. 1994; Yuan 2003). Specifically, Narayan, Yi, and Mahadevan (1995) found that this model could fit the spectral energy distribution (SED) of Sgr A* well.

1.3.3 Magnetohydrodynamic Modeling

With the development of computing systems capable of running large-scale two and three dimensional simulations, purely analytic models yielded way to complex magnetohydrodynamic models. Considering the equations of MHD, it is a fairly simple matter to make a single calculation of the behavior of a plasma, based on the equations of fluid dynamics combined with Maxwell's equations, which yield a set of differential equations which can be solved numerically. This becomes problematic when dealing with 2D or 3D grids extending over a number of cells in each dimension, and having to generate solutions over many timesteps.

A number of MHD codes have been developed over the years which are either delivered in a form ready to calculate AGN accretion disk solutions, or can be set up

through problem generators to do so. Those which are used for the projects here, as well as some which led to their development, are briefly described here.

Soon after the important rediscovery of the MRI instability, a series of papers detailing the newest version of the 2D Fortran MHD code ZEUS was released (Stone and Norman 1992a,b; Stone, Mihalas, and Norman 1992). This code underwent several iterations, including the development of 3D and parallel versions (Norman 2000).

The team which created ZEUS later turned their attention to the development of a new MHD code. Athena was created in both C and Fortran95, and was fully 3D and multi-processor capable from its beginning (Stone et al. 2008). As these capabilities were included, it has advantages in efficiency over its predecessor, and is generally more powerful, portable, capable, and user-friendly. For its use within Chapter 5, the shearing box approximation is invoked (Stone and Gardiner 2010) to consider a localized region of an accretion disk (Hawley, Gammie, and Balbus 1995).

For the global accretion disk simulations described in Chapters 3 and 4, which extend down to the event horizon, a modern code which takes into account the impact of general relativity is useful. Gammie et al. (2003) and Noble et al. (2006) describe the one used, HARM, a 2D GRMHD accretion evolution tool written in C, which is extendable to a large number of sources by simple changes in parameters. For the projects described within, with the intent of simulating global spectra, a 2D code captures the necessary details while being much more time-efficient than a fully 3D code.

1.3.4 Radiation Transport Modeling

Generation of radiative spectra from physical parameters can be accomplished

analytically or through a radiative simulation tool. For the projects in Chapters 3 and 4, a radiative transport code based on the Monte Carlo method is used. It is described fully in Chapter 2. This is a 2D cylindrical code which uses random number sampling of probability distributions to calculate emissions, and subsequently, scattering events, as photons are tracked through the simulation volume (Canfield et al. 1987; Liang and Dermer 1988; Böttcher et al. 2998; Böttcher and Liang 1998; Böttcher et al. 2003; Finke and Böttcher 2005; Finke 2007; Böttcher and Liang 2001). The MC method is fairly ubiquitous for these types of models, and codes which use it vary primarily in their set-up and capabilities. The chosen model allows for non-thermal and thermal hybrid distributions, Fokker-Planck (FP) distribution evolution, pair processes, multi-processor use, and time-dependent spectra consideration, making it a very powerful and useful tool for the study of astrophysical objects.

The modeling tools which have been briefly described are discussed in much greater detail in Chapters 2, 3, and 4. As similar codes which simulate physical and radiative conditions in astrophysical sources tend to differ mainly in details, only the tools which are used for the projects within this dissertation are mentioned here. It should be noted that these techniques have evolved over a number of decades and there are a plethora of available models which could be applicable to Sgr A* and M87. Within their respective chapters, more focus is placed on similar modeling pursuits by other groups.

1.4 Dissertation Motivation and Thesis

Modeling projects typically suffer from a series of drawbacks. This is usually due

to assumptions or simplifications which limit the impact of results. Often, an advanced technique may be coupled with a less-developed method, such as a full-scale MHD model producing high-resolution results that are then radiatively modeled with a simple, analytic emission model.

This dissertation's thesis is that modeling projects which make use of the most advanced tools available at each critical step are of significant use in motivating the understanding of physical processes which produce the considered data. Emphasis is placed on intelligent use of physics knowledge to lead to minimization of open parameters. Dedication to this philosophy ensures results are as consistent as possible and enables the most useful consideration of further changes, both in data and technique.

This approach leads to an initial modeling project on Sgr A*, using one of the most advanced global accretion GRMHD codes available, coupled with an MC radiation transport code which fully considers emission, scattering, and absorption. Results from this suite suggested some shortcomings to the MC code's consideration of bulk plasma flow anisotropic magnetic fields, which are then addressed prior to another full modeling project on M87. Analysis of the methods used in these two projects makes it clear that the most inconsistent component of the models is the unrealistic portrayal of electron distributions as purely thermalized. This leads to a study of localized turbulence and current sheet development in order to motivate particle-in-cell (PIC) trials to attempt to accurately model energized particle distributions, largely due to magnetic dissipation.

1.5 Thesis Roadmap

Chapter 2 details the MC radiation transport code used extensively for these

models, including modifications for specialized use. Chapters 3 and 4 discuss the full modeling projects to describe emissions and kinematics of Sgr A* and M87, respectively. Chapter 5 delves into the localized properties of AGN accretion disks with local shearing box simulations. Chapter 6 then recaps the work presented, with discussion and notes on possibilities of future progress. Finally, an Appendix has been included to describe the use of the MC code, with the intent to provide a user an easy-to-follow description of the methods to configure and run the code.

Chapter 2

Monte Carlo Radiation Transport Code

This Chapter will fully describe the Monte Carlo (with Fokker-Planck capabilities) radiation transport code used to simulate emissions from accretion disks in the detailed projects contained within this dissertation. In Section 2.1, the code is addressed from a historic standpoint, with large-scale changes to the code discussed. Section 2.2 contains a much more in-depth and comprehensive explanation of the code's inner workings, intended to provide a user with an understanding of the actual process, to allow further changes and personalization. To better describe emissions from accretion disks, modifications detailed in Section 2.3 separate velocities and magnetic fields into their constituent components, for consideration of anisotropy. Finally, see this dissertation's Appendix for a full explanation how to use the code, primarily from the standpoint of the parameters set by the basic input files.

2.1 Basic Summary and History

This Section details the major historical advances in the lifetime of this code, then briefly discuss its function, use, and layout.

Originally, the MC code was based on a much earlier time-dependent MC code developed at Los Alamos and Lawrence Livermore National Laboratories (Pozdnyakov et al. 1983). This basic idea was adapted by Canfield et al. (1987) into a Compton scattering code for astrophysical applications. At this point, it was used to study gamma-ray spectra of upscattered soft photons by relativistic electrons in idealized Maxwellian

distributions. The scattering electron population was allowed to be anisotropic. The one dimensional case was used to simulate regions of strong magnetic field to restrict flow perpendicular to field lines. These trials were compared to results from isotropic (in three dimensions) distributions of electrons.

Liang and Dermer (1988) further modified this initial code to include the effects of pair annihilation and production. This was used to model the gamma-ray bump of Cygnus X-1 as the result of a relativistic pair-balanced plasma in an accretion disk.

The next year brought the most far-reaching changes to the code thus far. Dermer and Liang (1989) published results which used the Fokker-Planck equation (Fokker 1914; Planck 1917) to describe the evolution of electron distributions in a thermal Maxwell-Boltzmann plasma, where electrons and protons may have different temperatures, as would likely be found in AGN or x-ray binary (XRB) accretion disks. For this to be useful, they also detailed these dispersion coefficients for a thermalized plasma, with the first due to the heating or cooling rate by radiation, and the second from Coulomb interactions between electrons and protons, and electrons and other electrons. Finally, as it was necessary to quantify heating or cooling due to radiation, the code was upgraded to include emissions, by bremsstrahlung, cyclotron, or synchrotron processes.

The next major re-work of the code came when Böttcher and Liang (1998) rewrote it to allow the model volume's one dimensional division into either spherical or slab geometries, with each zone in the grid containing different particle parameters. In this form, Böttcher et al. (1998) coupled the code with the XSTAR photoionization and line-transfer model to simulate XRB x-ray spectra. Later, this was used to model a cool blob moving inward through a hot disk or corona (Böttcher and Liang, 1999). The

simulated power density spectra and time lags were found to be viable to explain some temporal features of Cygnus X-1 and GX 339-4.

Earlier, Nayakshin and Melia (1998) had recalculated the Fokker-Planck coefficients to enable use with arbitrary electron distributions, including non-thermal, or composite thermal/non-thermal distributions. These advances were coupled to the code by Böttcher and Liang (2001), during a near-complete rebuild. This included adding stochastic acceleration by Alfven waves to the particle energization routines, simulating bremsstrahlung, cyclotron, and synchrotron emission within the volume, and the accompanying absorption mechanisms. In this form, it was used to model a spherical accretion shell around a weakly magnetized neutron star. Furthermore, Böttcher et al. (2001) modeled soft flares from disks sandwiched by hot coronae. This problem was reanalyzed by Böttcher et al. (2003) with the code's grid extended to two dimensions. This is the basic format of the MC code now - a 2D axially-symmetric, cylindrically-zoned grid.

The primary advancement following these references, and prior to this dissertation's projects, was the parallelization of the code using the Message Passing Interface (MPI). Finke (2007) describes this change in detail in his Ph.D. dissertation, documenting speed increases up to two-and-a-half times that of the serial code, when running with ten processors. On new equipment, the code has shown to continue to run faster, though not linearly, while using up to 128 processors. Around this point, the processor communication time starts to dominate and adding more processors maintains similar speeds.

Chen et al. (2011) first introduced several modifications to the code for projects

involving the modeling of blazars, with a particular emphasis on time-dependent phenomena. This included a revamping of the FP scheme to allow implicit coupling of MC and FP processes, which leads to more exact high energy distribution calculations. On the MC side of the code, a splitting method was applied to scattering calculations. In effect, this increases the statistical likelihood of scattering events, increasing further for repeated scatterings. This proves vital for obtaining accurate Compton scattering spectra (Chen et al. 2011; Chen 2012)

2.2 Detailed Code Flow

The progression through the code's routines follows the flowchart presented in Figure 2.1. This starts with the *main* routine, in compton2d.f, calling the *reader* routine (reader.f). This has the basic task of reading in the main input file (input.dat), which contains general information on the problem, such as total volume size, grid size, and output options. Following this, *reader* scans the input file for each separate zone (input_01_01.dat, etc.), which contains zone-specific parameters, such as particle distribution, temperature, density, and magnetic field. See the Appendix for specific examples of input files and a closer examination of each individual variable which can be adjusted through these.

Following the call to *reader*, *main* calls *setup* (setup2d.f). This is only called at the beginning of the run and is responsible for initializing the problem. This involves loading Compton cross-sections and energy exchange data from *imcdate* (imcdate2d.f), for ease of access throughout the run, and calling routines *Pref_calc* and *Wref_calc* (ref_matrix.f) which calculate Compton reflection matrix elements and information.

Setup continues on to initialize time data, such as the initial timestep, and spatial information, such as the grid spacing and zone surface specifications. Next, each zone's electron distribution is calculated by calling *gam_min* (gamma1_2d.f) and *P_nontherm* (nontherm2d.f). These combine the information given regarding thermal and non-thermal distribution parameters to calculate a total distribution within a zone. The final tasks for *setup* are initializing a number of arrays, such as the energy grid, census, energy loss and gain arrays, angle-dependent outputs, light curves, temperature distributions, and a table of inverse Compton loss kernel values (*IC_loss*, in icloss2d.f).

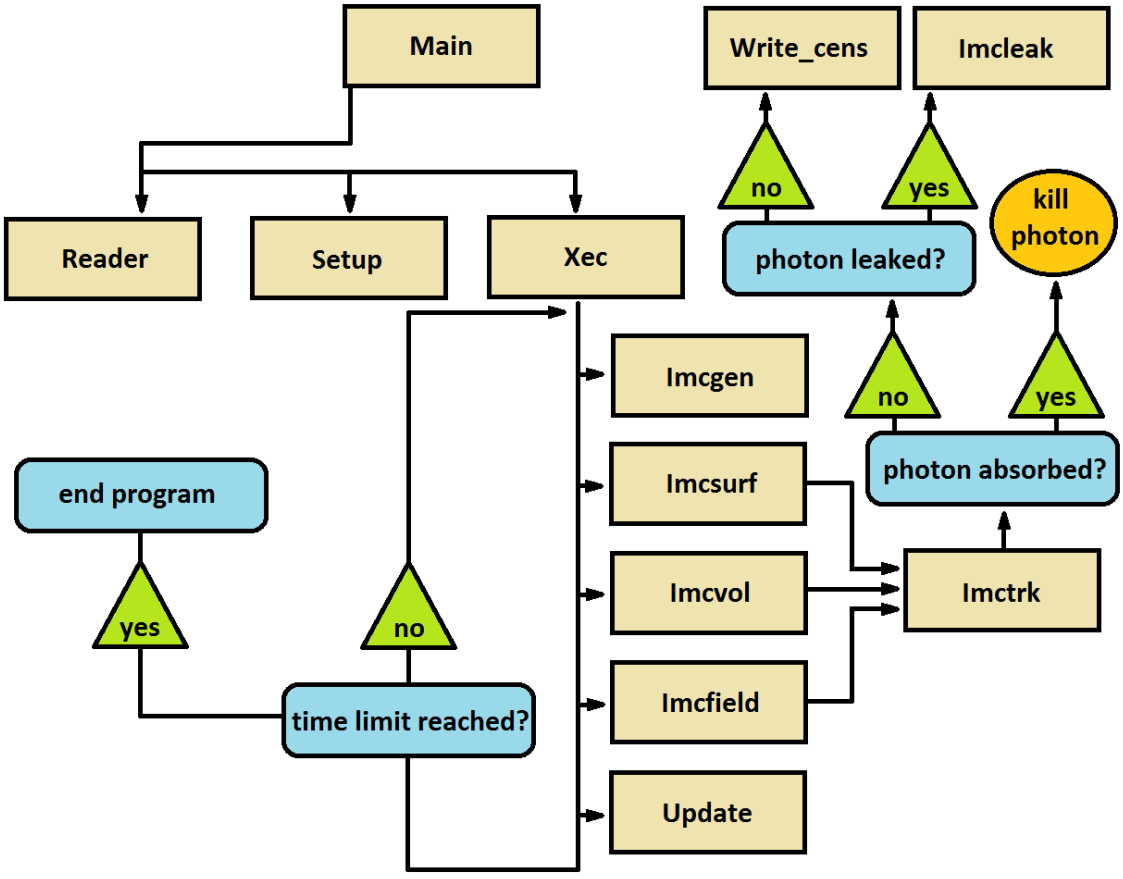

Figure 2.1: A flowchart depicting the macroscopic logic flow through the MC radiation transport code.

Once returning to *main*, the code advances into the main loop routine *xec*

(xec2d.f), which is responsible for iterating through time until a specified limit is reached. This concludes the *main* routine's responsibilities. Within *xec*, the loop calls a number of routines each timestep. These are, in order: *imcgen2d* (imcgen2d.f), *imcsurf2d* (imcsurf2d_para.f), *imcvol2d* (imcvol2d_para.f), *imcfield2d* (imcfield2d.f), *update* (update2d.f), and *graphics_collect* (graphics2d.f). The first, *imcgen2d*, is responsible for determining the total energy loss in each zone and from each surface (if surface emission is enabled and specified as an externally input spectrum) and converting this into an appropriate fraction of the volume's total emissions, represented by Monte Carlo photons. A Monte Carlo photon represents a large number of actual photons, due to the obvious difficulties in simulating a realistic photon field. The number of Monte Carlo photons is user-defined, so the code sets a weight for each which suggests the total energy (or number of actual photons) it represents.

The routine *volume_em* (volume2d.f) calculates the overall weight for each zone, according to its emission. This involves computing a full spectrum of cyclotron, synchrotron, bremsstrahlung, and (if enabled) pair-annihilation emission, based on the electron density, temperature, and magnetic field. This is stored as a probability distribution, so that later photons can be created accordingly, after the total number of photons assigned to each zone is determined. Along with emission properties, appropriate absorption opacities are found – notably that of synchrotron self-absorption, which constrains the synchrotron spectrum below the frequency where the plasma becomes optically thick, to a pure power law, $S(\nu) \sim \nu^{5/2}$. Once the total emission weight for each zone is determined, the following routines create the appropriate individual Monte Carlo photons.

First of these is *imcsurf2d*, which converts energy from an external source at a surface into photons. This is in direct contrast to the routines which consider electron parameters to determine emission, as photons are created here according to a user-defined spectrum. Having an external source of photons is optional, but is useful in situations where the intent is to see how the region will process a specified input spectrum. The bulk of this routine determines the amount of emission which occurs at each zone boundary along the grid - inner and outer, for r, and upper and lower, for z. The default setup randomizes the direction of photon propagation from the surface, obviously directed into the volume, rather than out of it. Another option is to specify that photons enter the volume with parallel trajectories, as though arriving from some distant external source. At this point, for the first time, we come across a call to *imctrk2d*. This routine tracks each MC photon, determining whether it is absorbed, scattered, or propagates freely. The tracking routine will be discussed in further detail following the volume calculation routine.

The *xec* loop continues with *imcvol2d*, which calls *vol_calc*. This routine takes the spectral probability distributions calculated by *volume_em* and uses them to create the appropriate number of photons for each zone, determined by the individual zone's emissive weights. This routine relies strongly on the Monte Carlo method, where random numbers are generated and compared to probability distributions in order to determine a number of parameters. In general, these include the photon energy, by the volume's emission spectrum, and the photon's initial location, which is random within the volume, and trajectory, which is selected randomly, prior to the changes which are discussed in Section 2.3. This emulates an isotropic electron distribution which is evenly distributed

through the emitting volume. As previously, once photons are generated, they are sent to *imctrk2d* for tracking.

The last photon routine called by *xec* is *imcfield2d*. This process is responsible for dealing with photons which were not generated this timestep, but were still in the volume after being tracked during the last step in the loop. The routine is basic, with its purpose being to read photon parameters from the census and then send them to *imctrk2d*.

During each timestep, all photons that were created, as well as any that existed previously, are tracked through the simulation volume by *imctrk2d*. This routine calculates three distances intially: (1) how far a photon will travel if unscattered, (2) how far a photon can travel before being scattered (randomly drawn from a distribution around its mean free path, calculated by *comtot*, in comtot2d.f), and (3) the distance to the nearest boundary along the photon's trajectory. The routine then acts on the shortest of these three distances. If this is (1), the photon is allowed to propagate unobstructed, and its position is updated within the zone and stored for the next step. For (2), the photon's position is updated until the scattering event, and then its parameters are sent to *compb2d* (compb_2d.f) which determines the resultant photon energy and direction, following its scattering. For (3), the photon propagates to the zone boundary and is sent to the corresponding adjacent zone. With the second and third possibilities, following either the scattering event or zone transition, *imctrk2d* effectively restarts and calculates the quantities again for whatever is left of the initial timestep, then acts upon the photon as appropriate. While each photon propagates, its energy weight, which is an effective measure of how many real photons the Monte Carlo photon represents, is adjusted according to the absorption properties of the particular zone it is traveling through. If this

weight drops below a threshold value, the photon is killed and removed from the census without being written to an output file. If the photon remains in the simulation volume after being followed through the entire timestep, its information is stored in the census for the next iteration.

If a photon reaches a boundary of the total volume while being tracked, it is sent to *imcleak*. This routine determines what happens at this point. The most basic possibility is that the photon has reached an outer boundary and is removed from the census and written to the appropriate output files. The event file records all information regarding the photon, such as its trajectory and position when it leaves the volume, its energy and energy weight, and the time that it left the volume. This allows for reconstruction of angle-, time-, and position-dependent spectra. The photon information is also added to the total, time-independent spectrum file. This may contain more than one spectra, for separate angular bins, if the user has defined more than one in the input file. Lastly, leaked photon information is recorded in the light curve files. These are user-defined according to minimum and maximum energies and show the total energy leaked in each band over time. If a photon reaches an inner boundary, or the user has defined the outer boundaries to not purely leak photons, there are other possibilities for how the code will deal with it. A boundary may be purely or partially reflecting, or purely absorbing, so the photon is simply killed and not leaked. These options may be useful for specific problems of interest, such as when one boundary represents the surface of a star.

The final step in the main loop of *xec* is to call *update2d*. This routine is responsible for evolving the electron distribution in each zone according to the Fokker-

Planck equation. As the photon distribution evolves significantly more slowly than the electron distribution, there are usually several, or many, FP iterations during each photon timestep. Though the projects described in this dissertation use a constant temperature assumption, and therefore FP evolution is disabled, it is useful to briefly consider how the routine evolves an electron distribution. Initially, each zone's electron distribution may be described as a combination of a thermal Maxwellian at a specified temperature and a non-thermal power-law, with low- and high-energy cut-offs. This will often be a thermal component with non-thermal high-energy tail.

The FP equation takes the form:

$$\frac{\partial n_e(\gamma,t)}{\partial t}=\frac{-\partial}{\partial \gamma}[n_e(\gamma,t)\frac{d\gamma}{dt}]+\frac{1}{2}\frac{\partial^2}{\partial \gamma^2}[n_e(\gamma,t)D(\gamma,t)]$$

where n_e is the electron density, γ is the particle's Lorentz factor, $d\gamma/dt$ is the heating or cooling rate, representing the average rate of energy exchange due to emission and scattering, and

$$D(\gamma,t)=\frac{d(\Delta\gamma^2)}{dt}$$

is the energy dispersion coefficient, at an average rate for a test particle. These two coefficients are combinations of a number of those due to specific processes. The dispersion coefficient takes the form:

$$D=D_{ee}+D_{ep}+D_A$$

and the energy exchange coefficient becomes:

$$\frac{d\gamma}{dt}=(\frac{d\gamma}{dt})_{ee}+(\frac{d\gamma}{dt})_{ep}+(\frac{d\gamma}{dt})_{sy}+(\frac{d\gamma}{dt})_{br}+(\frac{d\gamma}{dt})_{A}$$

The subscripts are as follows: *ee* for electron-electron elastic Coulomb scattering, *ep* for electron-proton elastic Coulomb scattering, *sy* for synchrotron emission, *br* for

bremsstrahlung emission, and *A* for Alfven wave acceleration. The dispersion coefficients for synchrotron and bremsstrahlung are insignificant in comparison to the other components. All pertinent coefficients have been compiled as libraries, both to save computation time, and as a service to the scientific community, as described by Finke (2007) and Finke and Böttcher (2005).

The system of equations is solved implicitly for each FP timestep. The coefficients are representative of a purely thermal distribution, so to begin the following timestep, the distribution is fit to a Maxwellian, giving it an overall temperature. This is a basic assumption, but following the initial calculation, the coefficients for Coulomb (electron-proton) and Moller (electron-electron) scattering are used to calculate the actual distribution. The coefficients due to other sources evolve slowly, and their value at the beginning of the step is used throughout. Clearly, this relies on the distribution remaining similar to a Maxwellian, with the non-thermal component describing a high-energy tail.

The parallelization of the code is fully described by Finke (2007). In general, these changes allowed the code to be run on multi-processor machines using Message Passing Interface (MPI). The routines from MPI have been applied at several points in the code: *imcsurf2d*, *imcvol2d*, and *update2d*. When the master process reaches these points, it uses an MPI broadcast routine to send each slave process a zone job. That is, each slave processor will be responsible for one zone within the simulation grid at a time. When it has finished with this zone, it returns the appropriate information to the master process, then receives another zone, if there are still some waiting to be operated on. The files vol_mpi.f and fp_mpi.f contain the MPI broadcast routines. They are also responsible for defining which variables need to be transferred from the serial portions of

the code to each slave process for the parallel portions. Because of how the zones are distributed to each slave, there is no benefit to using more processors than there are zones within the simulation grid.

2.3 Upgrades by this Author

As is detailed in Section 4.7, there are many astrophysical sources whose magnetic and velocity fields are anisotropic. For situations where this is important, such as in accretion disks, where the azimuthal component of the magnetic field dominates, and the bulk flow is in the orbital direction, the effect of isotropizing emission and scattering calculations can lead to inconsistent results. It is useful, therefore, to improve upon the method of these calculations to allow for these anisotropies.

For isotropic magnetic fields and particle distributions, the resulting synchrotron emission is also isotropic. However, when this is not the case, the synchrotron emission is strongly biased perpendicular to the magnetic field direction. Petrosian (1981) calculated the angle-dependent emissivity for a thermal Maxwellian of semi-relativistic particles to be:

$$j_\nu(\theta) \propto \exp\{-\frac{\nu}{\nu_b}[\frac{4.5}{\sin\theta}(\frac{\nu_b}{\nu kT})^2]^{1/3}\}$$

while for non-relativistic particles, it is:

$$j_\nu(\theta) \propto (\frac{1+\cos^2\theta}{\sin^2\theta})\exp[-(\nu/\nu_b)\ln(2\nu_b/e\nu kT\sin^2\theta)]$$

In these formulae, ν is frequency of emission, $\nu_b = eB/2\pi m_e c$ is electron gyrofrequency, T is the distribution's temperature, B is magnetic field magnitude, and θ is the angle relative to the magnetic field. The transition between these two regimes occurs

around $\nu kT/\nu_b = 1$, with lower temperatures leading to a non-relativistic calculation.

To institute this effect of anisotropic magnetic fields in the MC code, first *volume_em* had to be modified to track the amount of synchrotron vs. bremsstrahlung emission which is produced within each zone for each frequency bin. This information is drawn upon in *vol_calc* (called by *imcvol2d*), when a photon is assigned a specific frequency. If the photon is determined to be synchrotron in origin, the following block of pseudo-code demonstrates the method of calcuation of its angle of emission relative to the direction of the magnetic field, and then its assignment to a specific direction.

- Calculate pertinent variables, including the test value $\nu kT/\nu_b$.
- Loop: 0 to 2π
  - If test < 1, only calculate the non-relativistic value.
  - If test > 100, only calculate the semi-relativistic value
  - Else, calculate both values.
    - Calculate the appropriate argument for required exponentials.
    - Store the value of the maximum argument.
- Loop: 0 to 2π
  - Use the results from the preceeding if/else

statements.

- Subtract the maximum argument from each, to normalize the distribution and avoid unrealistically small values.
- Complete the calculation.

- Draw a random number and compare to the probability distribution to select an emission angle.
- Randomize the actual emission angle from the possible cone of emission around the magnetic field line.

The additions to the code rely upon the MC method, where possible. To determine if the photon is synchrotron in nature, a random number is drawn to compare to the fraction of emission in a frequency bin which is calculated to be due to synchrotron. Similarly, to determine the angle of emission relative to the direction of the magnetic field, a probability distribution is set-up and compared to a randomly drawn number. This supplies what is essentially a hollow "cone" of possible emission directions, around the magnetic field vector. Another random number draw determines at what position along the surface of this cone the photon actually propagates. This simulates an isotropic distribution of electrons in an area of anisotropic magnetic field.

An example of spectral changes due to the magnetic field modifications is shown in Figure 2.2. For a single-zone, hollow cylindrical trial, with a nearly purely radial field configuration, the results are just as expected. Synchrotron emission in a narrow cone around the polar direction is substantially stronger than in a similar angular bin around

the equator, due to the field lines being perpendicular to the polar direction. Also expected is the isotropizing effect of Compton scattering, with scattered photons emerging more isotropically than the synchrotron emission.

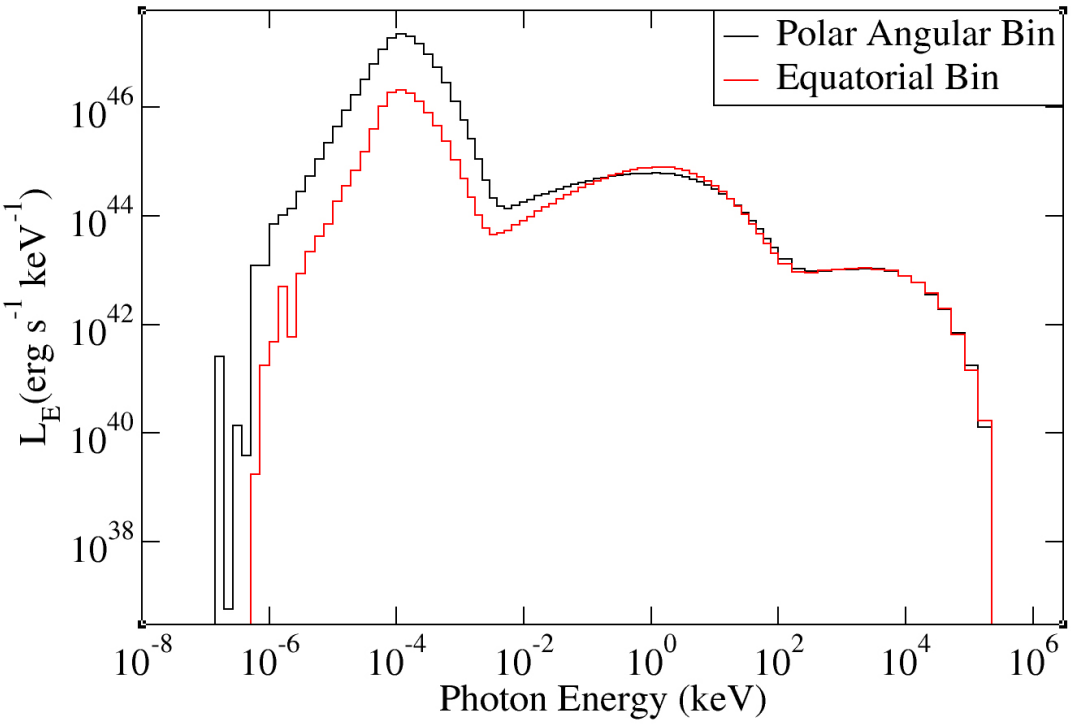

Figure 2.2: Trial of the anisotropic magnetic field modifications. This is a single zone run with nearly purely radial field, to best show the effect of the changes. As expected, the synchrotron emission is strongly biased toward the polar direction, which is always perpendicular to the radial magnetic field, while the Compton components are much more isotropized.

The second major change for more consistent modeling involves consideration of bulk electron flow. In regions where the distributions have a significant velocity, there are three modifications which need to be made at various points in the MC code:

1) First, when photons are emitted, they will be beamed and boosted in the direction of travel for the emitting population. This should occur after the previous change for anisotropic magnetic fields.

2) When calculating scattering depths and absorption, the bulk flow velocity must be

taken into account to reflect the larger or smaller effective column density for a photon traveling head-on or tail-on, respectively, to the distribution.

3) If a scattering event is determined to happen, the photon will not scatter from an isotropic distribution of electrons, if they are moving at a considerable velocity.

Naturally, as the MC code did not consider particle flow previously, all calculations are done in the rest frame of the grid, the lab frame. For the first step, the code is set up originally to allow isotropic emission when calculated in *vol_calc*, immediately after the synchrotron modifications. To consider emission that is beamed and boosted, it is simplest to let the code calculate the emission as though it is isotropic, then act upon the photon's direction and energy following that step. Rybicki and Lightman (1979) give simple formulae for beaming, or the aberration of light:

$$\cos\theta = \frac{\cos\theta' + \beta}{1 + \beta\cos\theta'}$$

and boosting, by the relativistic Doppler formula:

$$\omega = \omega'\gamma\left(1 + \beta\cos\theta'\right)$$

In these equations, θ represents the angle between the photon's direction and the direction of the inertial frame's motion. β and γ are the frame's velocity relative to the rest frame in units of the speed of light, and its Lorentz factor, respectively. ω is the frequency of the photon, or, equivalently, its energy. The primed frame is the frame in which the electron distribution is isotropic, while the unprimed frame is the rest frame, where the distribution is anisotropic. It is a simple matter to apply the Doppler formula to calculate the final energy, while to consider the photon's beaming in an arbitrary direction, the full Lorentz transform matrix must be used. This is defined as:

$$\Lambda = \begin{bmatrix} \gamma & -\beta_x\gamma & -\beta_y\gamma & -\beta_z\gamma \\ -\beta_x\gamma & 1+(\gamma-1)\frac{\beta_x^2}{\beta^2} & (\gamma-1)\frac{\beta_x\beta_y}{\beta^2} & (\gamma-1)\frac{\beta_x\beta_z}{\beta^2} \\ -\beta_y\gamma & (\gamma-1)\frac{\beta_y\beta_x}{\beta^2} & 1+(\gamma-1)\frac{\beta_y^2}{\beta^2} & (\gamma-1)\frac{\beta_y\beta_z}{\beta^2} \\ -\beta_z\gamma & (\gamma-1)\frac{\beta_z\beta_x}{\beta^2} & (\gamma-1)\frac{\beta_z\beta_y}{\beta^2} & 1+(\gamma-1)\frac{\beta_z^2}{\beta^2} \end{bmatrix}$$

where $R' = \Lambda(\beta) R$ and R is the four-vector representing the direction of travel of either a photon or an electron. For a photon, the spatial components make up a unit vector, while for an electron, the total vector's length is equal to β, its total velocity as a fraction of the speed of light. For the aberration of light, the following block of pseudo-code demonstrates the method of the boosting and beaming calculation.

- Allow the emission routine to run as originally intended, until a photon's trajectory is set, including the synchrotron changes.
- Adjust the photon's energy based on the simple Doppler boosting formula.
- Multiply the photon's initial trajectory, which is now assumed to be in the bulk flow rest frame, by the Lorentz transformation matrix, to return its trajectory in the lab frame.
- Calculate the new spherical emission angles from the new vector.

The second change needs to be made in *comtot*. This routine uses the rest frame density to determine a photon's travel distance to a scattering event, by using a random number to pick from a distribution around the photon's mean free path. As a photon will encounter less electrons if it is moving the same direction that the distribution is, and more if it is moving against the flow of electrons, we need to define an "effective density" to be used in the free path calculation. This takes a similar form to the Doppler formula, without the Lorentz factor. As the code calculates the free path based on density, simply changing this to the new effective density sets up the rest of the routine to make its calculation.

The last modification to allow the MC code to consider bulk electron flow is made in *compb2d*. This is the routine which determines the aftermath of a scattering event - the final direction and energy for a photon. It does this after a scattering event has been determined to take place, by choosing an electron for the photon to encounter from an isotropic distribution. Similarly to the photon beaming changes, the best way to go about this is to let the electron be selected as the code originally intended, then transform the electron's direction and velocity into the lab frame. The previously cited aberration of light formula is a specialized form of the general relativistic aberration formula:

$$\tan\theta = \frac{u'\sin\theta'}{\gamma\left(u'\cos\theta' + v\right)}$$

where u' represents the velocity of the particle in the primed frame, and v is the frame's velocity compared to the lab frame. The transformation is done very similarly to the block of code shown from *vol_calc*, but instead of using spatial components which add up to a unit vector, as the photon travels at the speed of light, it operates on spatial components whose magnitude is the particle's velocity. As the transform uses the same

form, it will not be reiterated.

The combination of these changes can been seen in Figure 2.3. This is, as before, a single-zone, hollow cylindrical trial, with several runs at different Lorentz factors, for the azimuthal velocity. As the Lorentz factor is increased, the strength of synchrotron emission also increases. Emission is now beamed in the general direction of travel for the plasma, so photons tend to scatter less frequently, causing the observed drop in amplitude for scattering spectra, but the increased energy due to bulk flow also leads to higher possible scattering energies.

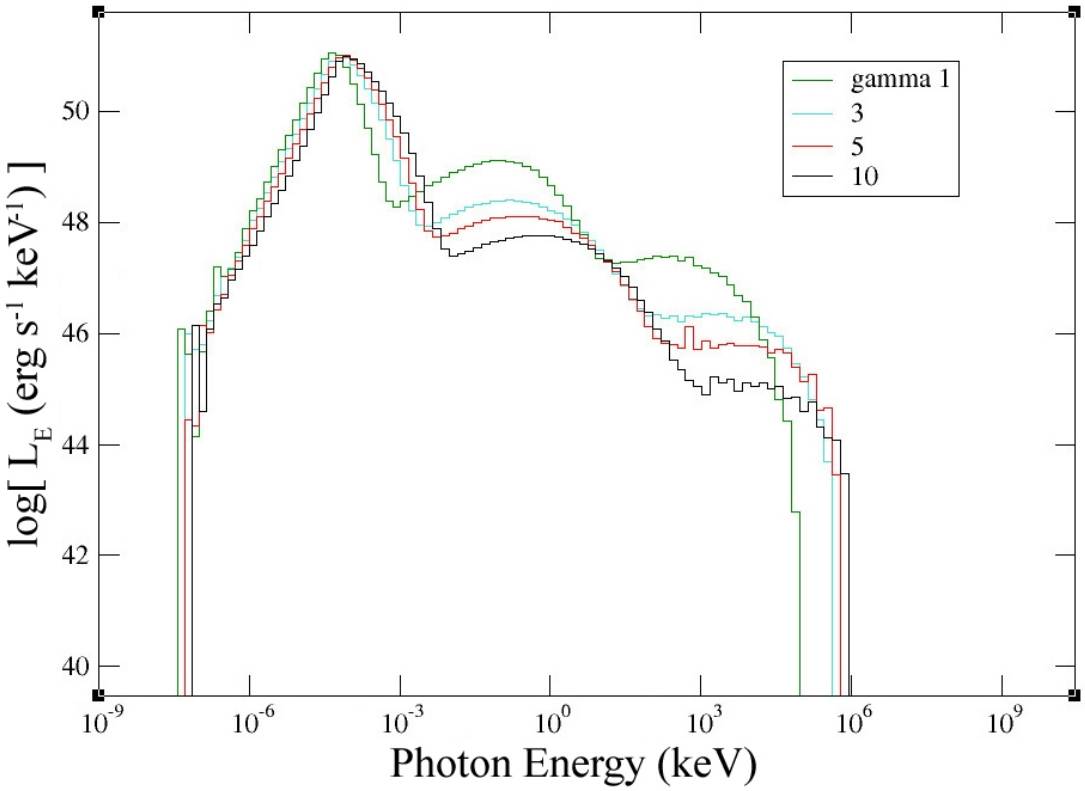

Figure 2.3: A single zone trial to illustrate the effects of the suite of velocity modifications. The general effects of higher Lorentz factor (γ) can be seen in the boosting to higher energies, the loss of scattering frequency, as photons are beamed in the direction of electron travel, and a possible increase in scattered energy.

It should be specifically noted that these modifications were not in place for our earlier study on Sagittarius A*, which is detailed in Chapter 3. They were included for

the M87 study, in Chapter 4.

Chapter 3

Monte Carlo Simulations of the Broadband Spectra of Sagittarius A* through the use of General Relativistic MHD

We present results of simulations of the spectrum of the accretion flow onto the supermassive black hole in our Galactic Centre, Sagittarius A*, generated with a coupling of Monte Carlo radiation transport and general relativistic magnetohydrodynamic codes. In our modeling, we use the 2D HARM GRMHD code to first model the physical parameters of the disk, then feed its results into our 2D MC photon transport code. We will discuss results obtained which fit radio, IR, and *Chandra*-obtained x-ray data points, assess the parameter scaling required to fit quiescent and flaring x-ray spectra, and comment on likely methods of emission and flaring.

3.1 Introduction

In recent years, a great deal of effort has been made to understand the complete picture of Sagittarius A*, a radio/IR/x-ray emission source at our Galactic Centre. It is widely accepted that this source is related to the accretion flow of a supermassive black hole whose mass we have taken to be 3.6 million solar masses (Ghez et al. 2003; Schödel et al. 2007; Melia 2006).

The spectrum of Sgr A* shows several important components or signatures. Balick and Brown (1974) first discovered the source in the radio/NIR, and ensuing observations by a number of researchers confirmed the strength of the source to be primarily in these regimes. Years later, Sgr A*'s x-ray spectrum was explored by

Baganoff et al. (2001, 2003), which found notable signatures higher than 10^{17} Hz, and also found a variability in this range, which suggests separate spectral states -- flaring and quiescent. Simultaneous multi-wavelength observations have generally supported this suggestion (Eckart et al. 2004, 2006; Bélanger et al. 2005).

A number of models have arisen to explain the mechanisms at work to produce the spectra of black holes. The standard-disk idea was first explored by Shakura and Sunyaev (1973) and proposes a situation in which gravitational energy is efficiently converted to radiation. This is most appropriate for optically thick disks with the flows on nearly Keplerian orbits. Sgr A*'s luminosity is less than 10^{-8} L_{Edd}. Sources with such low luminosities may be described by the standard-disk idea in cases where the disk remains cold and is optically thick, and the luminosity is low primarily due to a very low accretion rate. However, the accretion flow in Sgr A* must be very hot, and there is no evidence for a cold, optically thick disk component. The low luminosity is limited by both a low accretion rate and a low emission efficiency of the flow. In cases such as this, other accretion models need to be considered.

One developed model is called the advection dominated accretion flow (Ichimaru 1977). This model suggests that close to the horizon, much of the energy of the accretion flow was advected into the black hole, rather than being radiated away, and was explored by a number of groups, including Narayan and Yi (1994), Abramowicz et al. (1995), and Yuan et al. (2003). It was found that the ADAF solution can fit Sgr A* data well (Narayan et al. 1995), but while promising, this approach had several major drawbacks, namely its one dimensional approach and simplification of magnetic fields. The X-ray emission is produced primarily at large radii, which cannot account for the observed short-timescale

X-ray flares. In an attempt to consider an alternative approach, Yuan et al. (2003) suggested inclusion of nonthermal electrons and found satisfactory fits, but again with simple magnetic fields.

It became apparent that a more complicated treatment of magnetic fields would be important for a more accurate simulation, as the magnetorotational instability was found to be of vital importance in the development of turbulence that drives the accretion flow (Hawley and Balbus 2002; Hawley 2001; Balbus 2003). This instability ensures that in an accretion disk environment the necessity of outward angular momentum transport leads to the establishment of very complex flow and field patterns.

Models have since begun using magnetohydrodynamic codes to simulate accretion flows, with some measure of success. Ohsuga et al. (2005) ran emission simulations on an MHD model by Kato et al. (2004) and was able to fit data well, but had difficulties doing so without cutting out a large portion of their simulation volume. Goldston et al. (2005) calculated the radio spectrum based on MHD simulations done by Igumenshchev et al. (2003), but not other spectral bands.

This work explains and examines a simulation method which minimizes compromises on consistency via assumptions or simplifications by using the best tools available to present a more realistic accretion disk picture.

The approach to Sgr A* modeling using GRMHD and MC methods is presented in Section 3.2, with the results from these methods shown in Section 3.3. Section 3.4 then revisits the most important revelations and conclusions made within.

3.2 Simulation Method

Our modeling method involves the coupling of two very different codes which complement each other to provide a consistent view of the physical and spectral conditions in the accretion disk of Sagittarius A*. Detailed in the appropriate sections below are descriptions of the codes, discussions of their appropriateness for our work, and the manner in which they were coupled to provide an overall model.

3.2.1 HARM GRMHD Physical Space Modeling

The GRMHD code selected to determine the model's physical space is the 2D HARM code presented and detailed in Gammie et al. (2003) and Noble et al. (2006). It is not within the scope of this paper to completely detail the HARM code's inner workings, so readers should see these referenced papers for further information.

The code solves hyperbolic partial differential equations in conservative form -- uniquely suiting it to a number of astrophysical problems, specifically those involving magnetohydrodynamics in areas where general relativity is important. As the code evolves the space through time, conserved variables are converted to primitive variables at each step, to calculate a set of fluxes, given a set of sources. Use of primitive variable calculations allows the code to work with analytic solutions, rather than finding solutions numerically -- leading to much faster calculation time.

In this case, the variables tracked include density, total energy, internal energy, flow velocities, and magnetic fields. The last two are calculated both as 3-component and 4-component tensor quantities.

3.2.1.1 Model Set-up for our Work

As imported, HARM was set-up quite appropriately for our purposes. It was configured to evolve an accretion disk about a black hole, given a number of user-controlled parameters, on a 2D grid spaced (in spherical coordinates) radially and angularly, and assumed to be axially symmetric about the black hole's spin axis. The cells are assumed to be uniformly spaced with regard to a set of coordinates X1 and X2, which can be converted then to r and theta, respectively. This conversion leads to a logarithmic spacing in r, with cells closer to the horizon having greater resolution (and smaller size), and more concentrated cells closer to the equator. This effectively increases resolution in the plane of the accretion disk and close to the black hole, where the detail is most useful due to the much smaller length scales of interest in these regions. The resolution increase toward the horizon is vital to the successful running of the code, as it helps maintain proper cell aspect ratios on the polar grid. A graphical representation of HARM's grid layout can be seen in Figure 3.6, where it is compared to the MC code's grid.

At the start, HARM seeds an equilibrium torus around the black hole with density as detailed by Fishbone and Moncrief (1976), and defined according to:

$$\ln h = \frac{1}{2}\ln\left[\frac{1+\left[1+4\,l^2\Sigma^2\Delta/\left(A\sin\theta\right)^2\right]^{1/2}}{\Sigma\Delta/A}\right]+\frac{1}{2}\left[1+\frac{4\,l^2\Sigma^2\Delta}{\left(A\sin\theta\right)^2}\right]-\frac{2\,aMrl}{A}$$
$$-\frac{1}{2}\ln\left[\frac{1+\left[1+4\,l^2 r_i^2\left(r_i^2-2\,Mr_i+a^2\right)\left(r_i^3+r_i a^2+2\,Ma^2\right)^{-2}\right]^{1/2}}{r_i\left(r_i^2-2\,Mr_i+a^2\right)/\left(r_i^3+r_i a^2+2\,Ma^2\right)}\right]$$
$$+\frac{1}{2}\left[1+\frac{4\,l^2 r_i^2\left(r_i^2-2\,Mr_i+a^2\right)}{\left(r_i^3+r_i a^2+2\,Ma^2\right)^2}\right]^{1/2}+l\left[\frac{2\,aM}{r_i^3+r_i a^2+2\,Ma^2}\right]$$

Here, h represents enthalpy, which sets pressure. This is based on r_i, the inner torus radius, a, the black hole spin, l, the angular momentum, and Σ and Δ, physical parameters in a Kerr metric, and is appropriate for a relativistic, polytropic equation of state.

The torus is perturbed by adding a small poloidal magnetic field and allowed to

evolve around the black hole. We have not attempted runs with an initial toroidal, azimuthal field, though this is allowed by axial symmetry, and should serve to increase the total field at the end of simulation. The additional toroidal component should not influence the MRI development, instead only adding to the final field.

While most default parameters as included are appropriate for the simulation, several had to be adjusted for this project. To effectively simulate conditions near an a low luminosity Active Galactic Nuclei, where the nonrelativistic gas pressure presumably dominates, an adiabatic index of 5/3 was chosen. This is appropriate for a situation where matter is typically non-relativistic. In this case, ions dominate the total pressure and are non-relativistic, despite electrons possibly being semi-relativistic. As a first approximation, we have chosen a non-spinning black hole. Future work will study the effects of including black hole spin. The simulation volume ranges from just inside the horizon at 2 GM/c^2 to 40 GM/c^2 -- with the initial torus having an inner radius of 6 GM/c^2 and its pressure maximum at 14.7 GM/c^2. Our final trial was done on a grid of 512x512 -- that is, 512 radial cells by 512 angular cells. Output from the code is all scaled to M, the black hole mass, for near complete freedom.

3.2.1.2 Results and Interpretations

Our simulation was run to approximately 8000 timesteps, which equates to about 1.4×10^5 seconds, in physical time within the simulation. Figure 3.1 displays and explains four panels, which show density, internal energy, squared magnetic field, and bulk lorentz factor through the simulation volume. Of importance to note is that the images are shown evenly spaced in cell number. This creates a kind of stretching effect near the equator and

near the horizon -- causing the disk to appear much thicker than it actually is.

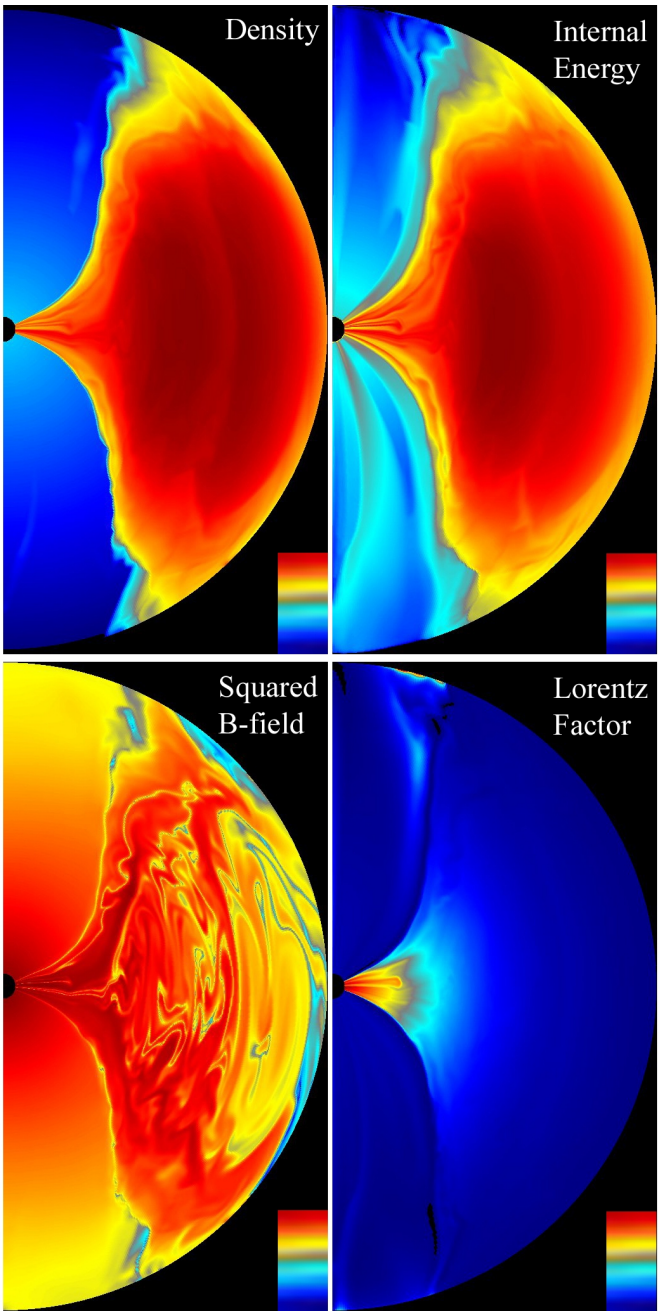

Figure 3.1: Panels from final timestep t = 8000 M (1.4x10^5 s) of HARM data, as labelled for different physical quantities. We show a cut-out in the r-z plane, with the black hole's horizon shown on left. As detailed in the text, the radial direction is scaled logarithmically, and angular dimension is scaled more finely toward the equator. Therefore, the finest resolution is obtained closest to the horizon and equator. This causes a "spreading" effect in the images, as they are shown evenly spaced by cell number, not physical value. Each quantity is shown on a logarithmic scale, with dark red being the highest values, black being the lowest.

As expected, the density concentrates itself around the equatorial plane, with the internal energy contours closely following. The magnetic field is strongest in the disk region, but saturates the region, generally being stronger nearer the horizon. More importantly, one can see how highly turbulent the field becomes after being seeded smoothly in the initial torus. As the turbulence is expected to provide the mechanisms for electron heating, in future work, the level to which the field is churned up will be important to analyze. The final panel shows the bulk gas Lorentz factor, which is, as expected, closely related to distance from the black hole.

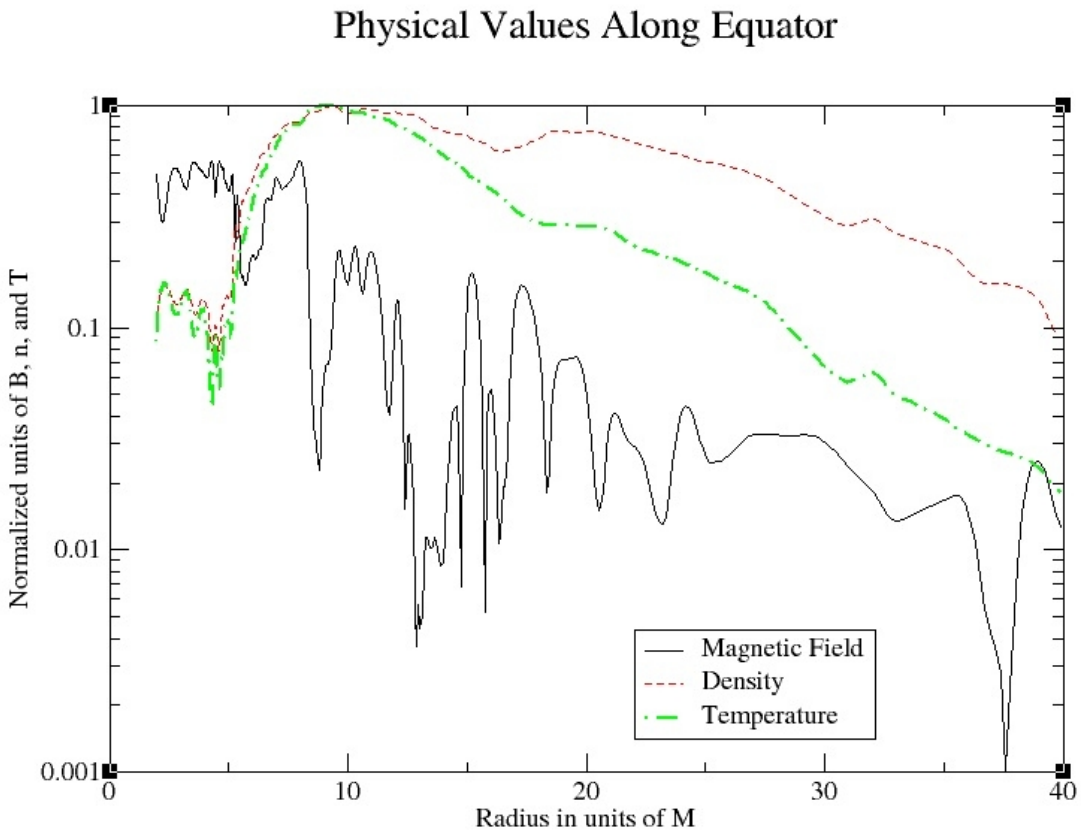

Figure 3.2: Profiles of magnetic field, density, temperature, along the equator, as a function of radius. These quantities are normalized to the maximum value for each. Of particular interest is the turbulent magnetic field, compared to the smoothness of other quantities.

Figure 3.2 shows profiles of density, temperature, and magnetic field along an

equatorial slice of the simulation volume. Again of note is the high level of turbulence in the magnetic field. Within 5 GM/c^2 (gravitational radii, which, with G = c = 1, becomes M, as shown in the Figure), the density and temperature drop to very low levels. This corresponds well with the flow velocities as this is expected to be where the flow becomes almost completely radial, and may be mostly a product of how quickly matter falls to the horizon at this point. Of some concern is how much these final profiles are due to the intial torus set-up. Further trials would be needed to compare initial torus location to final results.

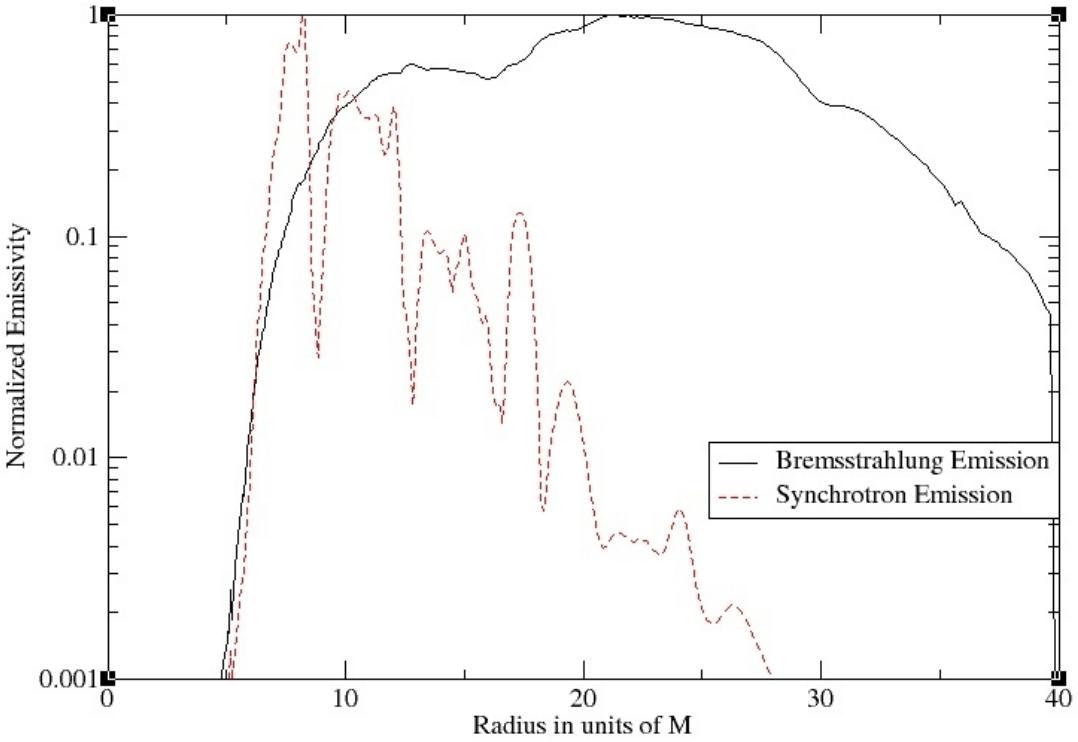

Figure 3.3: Profiles of optically thin synchrotron and bremsstrahlung emissivity. These values are normalized to the maximum for each set, so no comparisons should be made between the strength of the two components from this plot. These values are found by determining the emissivity within the closest cell and multiplying it by the radius and scale height at that radius.

Figure 3.3 also shows a profile of the synchrotron and bremsstrahlung emission as a function of radius. To calculate this value, we multiplied the optically thin synchrotron

emissivity and bremsstrahlung emissivity, respectively, by the radius and density scale height at that radius. The synchrotron emissivity was found by averaging the magnetic field over a number of zones near the equator -- this helps eliminate some of the high variability seen in the magnetic field. It should be noted that the overall shape did not change dramatically as this was averaged over a smaller or larger number of cells. It is apparent that the majority of emission emerges between radii of approxiately 8 M and 28 M. Areas inside and outside this region contribute decreasing amounts to the total emissivity. It is important to note the lack of contribution from the 28 - 40 M region to overall emission, as our simulation volume for the MC code only extends to 28 M (as is discussed below, in relation to the overlap of our two simulation grids).

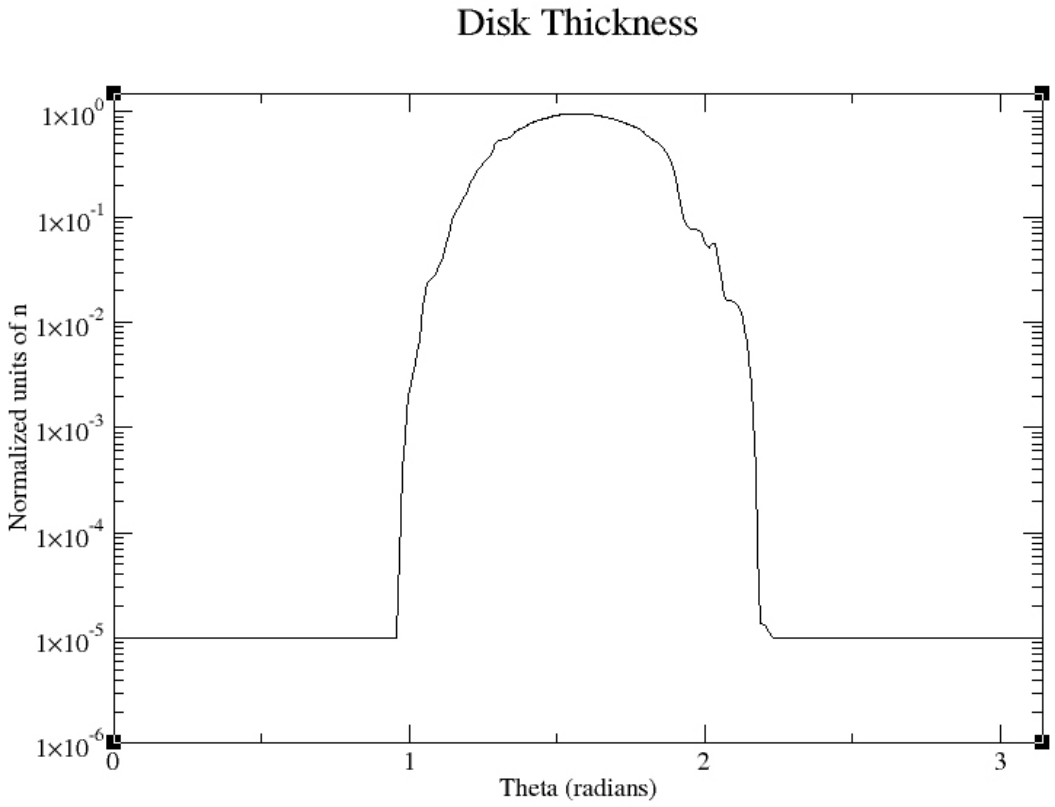

Figure 3.4: Profile of density along a constant radius r = 9 GM/c² slice over theta, from pole to pole. For reference, at this radius, the scale height is 2.7 GM/c².

To demonstrate actual disk thickness, Figure 3.4 shows density along a typical

slice through a constant radius r = 9 GM/c^2.

Our last HARM output figure, Figure 3.5, shows the variance of mass accretion onto the black hole through a surface at 28 M through time. When comparing parameters required to generate spectra at quiescent and flaring data points, the amount that accretion varies could be important in determining the appropriateness of the variation in values used between the two points. In general, at a late time, mass accretion varies up to a factor of two. The time scale of accretion variation, on an order of several hours, is reasonable for the observed variations in Sgr A*'s spectrum. As accretion variation is due not only to instabilities in the flow but also to changes in density of accreted matter, this factor of two is not considered a constraint on scaling.

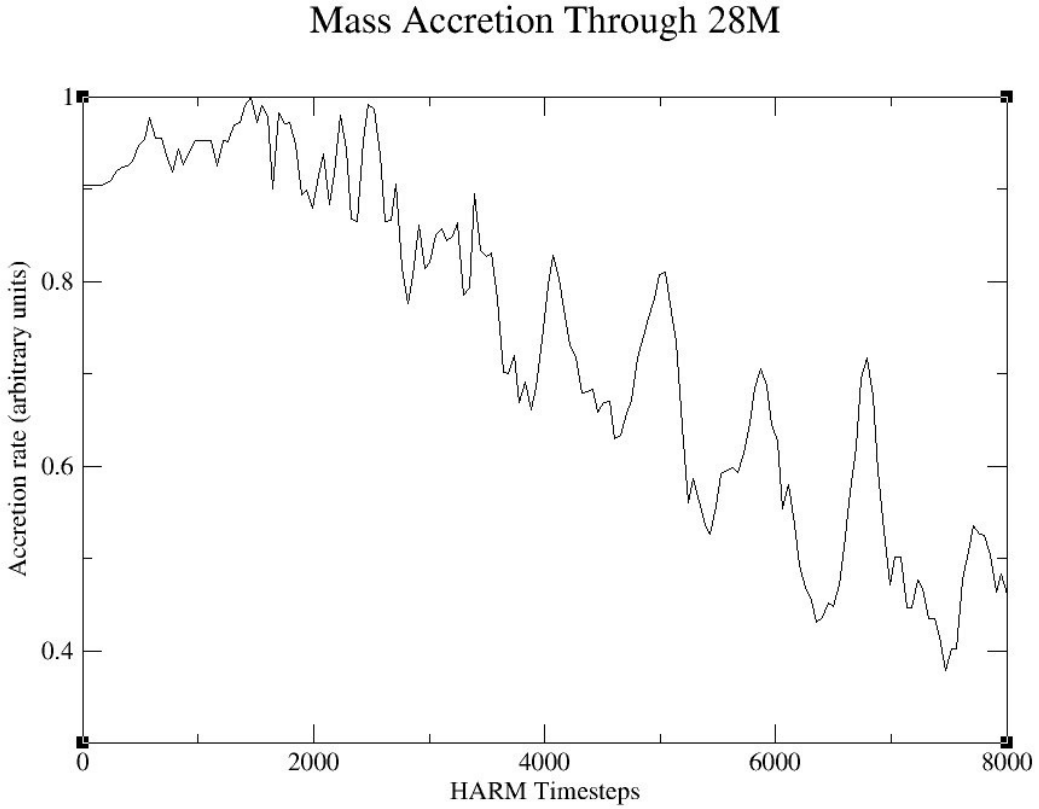

Figure 3.5: Mass accretion rates onto the black hole through a surface at 28 M as a function of HARM timestep - with each timestep being equal to about 17 physical seconds. Of interest is the amount of relative variation over short time scales.

3.2.2 Spectrum Determination with MC Code

The MC code used for photon emission and scattering has a long history and is discussed in a number of resources (Canfield et al. 1987; Liang and Dermer 1988; Böttcher et al. 2998; Böttcher and Liang 1998; Böttcher et al. 2003; Finke and Böttcher 2005; Finke 2007; Böttcher and Liang 2001). For a complete treatment, readers should see these papers.

In general, this code is a coupled MC/FP code. For our intents, the FP evolution of the electron distribution was unnecessary at this stage, as particle energization methods in accretion disks are not well-understood, so it was turned off to enforce a fixed temperature given by the HARM output. The code is set up on a 2D axially-symmetric cylindrical grid, creating a (hollow or solid, depending on whether the inner radius is set to zero) cylindrical shape. Each zone is assigned a density, ion and electron temperatures, magnetic field amplitude, and thermal and nonthermal distribution components. For our purposes, this is simply set to be a Maxwellian, but the code allows power law nonthermal distributions as well. The code allows emission from the volume and boundaries, and emitted photons are tracked and allowed to scatter or absorb.

This approach should be quite consistent, but it should be mentioned that the MC code does not include general relativistic effects. Close to the horizon, the photons' paths should be bent by the high gravity -- but this code does not include this effect. However, as was shown in the previous section, densities, temperatures, and emissivities are quite low, relatively, near the horizon. Because of this, it is expected that these GR curvature effects would be minimally important for computing the global spectrum.

3.2.2.1 Coupling GRMHD Output to MC Input

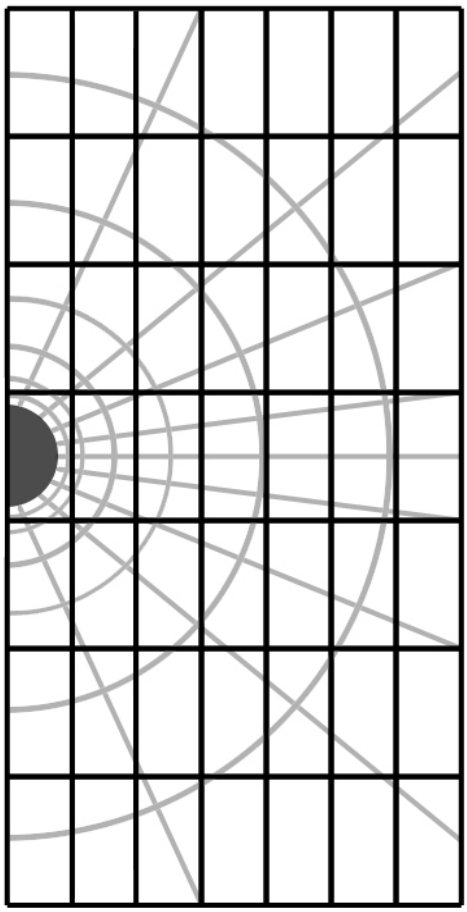

Figure 3.6: An exaggerated representation of the HARM and MC code grid overlays. The spherically spaced grid underneath is that of the HARM code. The rectangularly spaced grid overlaid is that of the MC code. Both grids are axially symmetric, with said axis on the left side in this image.

Shown in Figure 3.6 is an overlay of the grids for the two codes. It can be easily seen that regardless of how our MC grid is set up, it will almost invariably undersample and oversample the HARM grid at different locations. This is minimized as much as possible by making a very large MC grid -- in our trials, we use a 95x95 vertical by radial grid. The grid can actually be quite a bit coarser than this before one notices a significant deviation in spectrum. As we cannot cover the entire region with a rectangular grid, we have chosen a box which is 28 GM/c^2 radially and 56 GM/c^2 vertically. This box is

oriented so that its inner edge is at the horizon.

As noted previously, the output from HARM is completely scalable by black hole mass. For our trials, a rather well-accepted value of 3.6×10^6 solar masses was assigned. We also have the freedom to choose maximum initial density and have the other parameters scale with the density consistently. Density is scalable in this way since it only reflects a change in accretion rate.

In the HARM output, to determine temperature, we use internal energy. As almost all contributions to this come from ions, we can determine an ion temperature in each zone, but not an electron temperature. Coulomb coupling is very low due to the low densities expected in the accretion disk of Sgr A* (about 10^6 to 10^{10} particles/cm^3), and as the nonthermal heating and cooling mechanisms are not well understood, maximum electron temperature is kept as a free parameter for spectral fitting purposes in this paper. This means, in effect, we are setting a constant global ratio between T_i, the temperature of the ions, and T_e, the temperature of the electrons, and therefore assuming a two temperature flow, though this ratio is allowed to change between trials.

We consider the magnetic field given by the HARM data to be the MRI-saturated field. As mentioned previously, had we input an initial toroidal field, this would have contributed to the final total field. For this reason, we use the MRI-saturated field as a lower limit to our field value and allow scaling above this.

So, in effect, we set a maximum density, which in turn sets an ion temperature and lower limit to the magnetic field. The electron temperature is freely changed by changing the ratio between T_i and T_e, and the magnetic field can be scaled up from its initial value as necessary.

3.2.2.2 Trial and Fitting Procedure

Figures 3.7 - 3.11 show observational data points for Sagittarius A*, whose distance is taken to be approximately 8 kpc, and trial fits. Circles shown represent data points, upside down triangles are upper limit values, and the bowties are flaring and quiescent points from Chandra observations presented by Baganoff et al. (2001).

Data in the radio to IR range are fairly easy to fit on their own. This is typically done with synchrotron emission arising from the acceleration of moving charges by a magnetic field. When sufficiently energetic, these charges (electrons, in our case) produce a continuum spectrum whose flux and turnover frequency are directly related to the values of electron temperature, magnetic field, and density in this region.

In such a hot medium, synchrotron self-absorption becomes important. This phenomenon occurs when a photon interacts with a charged particle in a magnetic field and transfers its energy to the particle. The low energy positive slope of the synchrotron curve in each of the trials shown below is due to synchrotron self-absorption.

The difficulties arise in fitting the flaring or quiescent points in the x-ray simultaneously with the radio/IR data. The approach made in this paper is to initially try to fit the flaring point. Its flat slope in L_E suggests that it might be fit by several possible components of the spectrum:

1) Bremsstrahlung emission, or free-free emission, arises (usually, and in this case) from the acceleration of a free electron by a free nucleus, in a completely ionized plasma. This creates a relatively flat spectrum in L_E out to a cut-off point which corresponds with the temperature of the plasma. The flux of this component is directly related to the square

of the density, as it depends on the population of electrons and ions, and also to the square root of the temperature. Temperature also serves to locate the high energy cut-off in the spectrum. Magnetic field values do not affect bremsstrahlung emission.

2) Compton scattering is produced when photons interact with particles (in this case, electrons), leading to changes in energy for both photon and particle. Of interest for our work is inverse Compton scattering, where a less energetic photon gains energy in an interaction with a hot electron. In general, this tends to form a photon population whose shape is related to the initial photon distribution and the electron distribution it scatters from. This spectrum is typically shifted up in energy an amount approximately equal to the square of the Lorentz factor of the electron population, and drops in flux by an amount equal to the optical depth of the scattering medium. For our trials, the Compton spectrum of importance is mostly generated via synchrotron self-Comptonization (SSC), which refers to the Comptonization of a photon spectrum produced via synchrotron emission by the population of electrons responsible for emitting it to begin with. As the final spectrum resembles the electron distribution and initial (unscattered) synchrotron spectrum, it is possible to locate this spectrum so its flat top intersects the flat flaring x-ray point.

3) The second Compton scattering component, as its name suggests, is the spectral component created by the Compton scattering of an already scattered photon population. In this case, it shares the characteristics of the first scattered spectrum, and therefore is a viable component to fit the flaring x-ray point.

These individual components are labeled graphically in Figure 3.7. All information on emission processes can be found in Rybicki and Lightman (1979).

A large number of MC runs were done to find several sets of parameters which fit this point while remaining consistent with the order of magnitude estimate for total luminosity of 10^{36} erg/s suggested by Yuan (2007).

The second step in fitting was to attempt to fit the quiescent x-ray data point by varying parameters from those found to fit the flaring point. This was done, specifically, by using the same input values as the flaring point, but by dropping either the density or temperature until the spectrum went through the quiescent point. Depending on the component being fit to the x-ray data, one or both of these parameters could be changed to lower the luminosity to intersect the quiescent point. As we have data showing the variability of mass accretion by HARM, we can estimate reasonable changes in density. Due to the unknown nature of electron heating, it is not inconsistent to suggest that flaring and quiescent points may also arise due to brief moments of higher or lower heating, caused by dissipation of large current sheets in the MRI-turbulence cascade.

It should be noted that observations show a strong correlation between x-ray and radio/IR flux during flares. As it is generally accepted that the lower energy spectral component is due to synchrotron, this lends strength to the idea that the x-ray data is of synchrotron origin -- either as a self-Comptonization component, or an extended synchrotron component (Liu and Melia 2001; Markoff et al. 2001; Dodds-Eden et al. 2009).

3.3 Results

The results presented are shown first for fits to the flaring data (the higher x-ray point), then for fits to the quiescent data (the lower x-ray point). The HARM data used in

the MC runs are based on output at the last timestep (t = 8000 M). Fits are described by the component used to fit the x-ray data. However, this does not indicate that other spectral components were turned off during these runs. For instance, the bremsstrahlung spectrum can be seen to have both first and second Compton bumps, but the spectrum at the x-ray point is almost purely bremsstrahlung.

3.3.1 Flaring Results

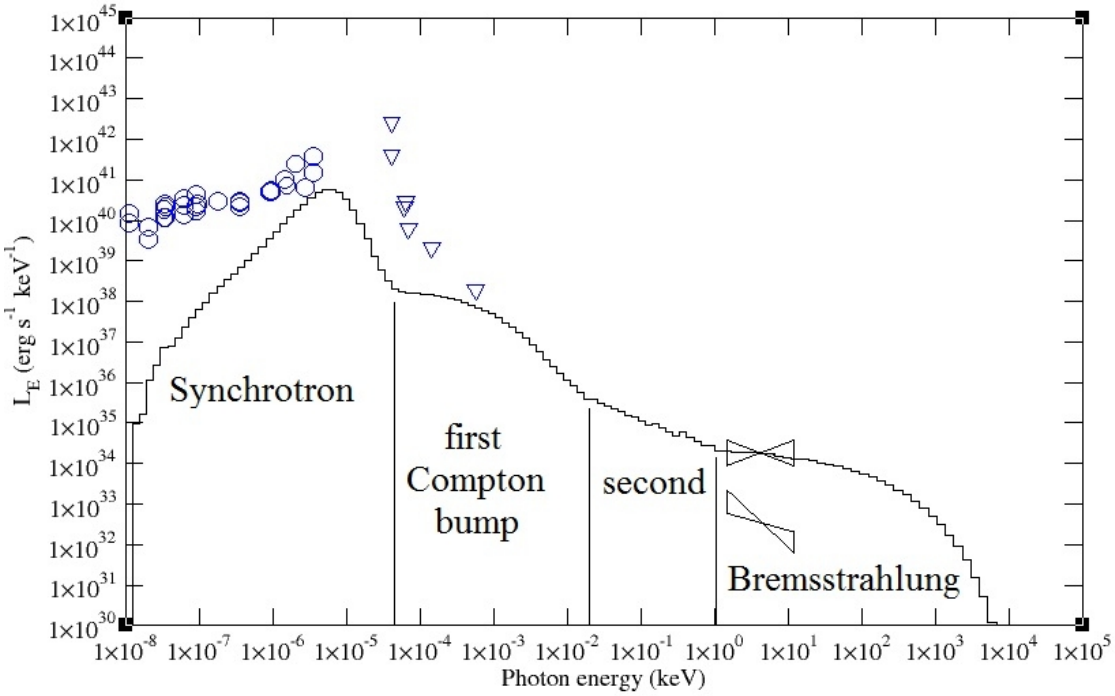

Figure 3.7: Fit to flaring data with bremsstrahlung component. Maximum values of the 95x95 cell grid are scaled to n = 4.3x10^9 particles/cm3, T = 1.2x10^3 keV, B = 9.9x10^2 G. Total luminosity is 3.4x10^{36} erg/s. The spectral components are labelled for clarity.

Figure 3.7 shows an attempt to fit the flaring data with the spectrum's bremsstrahlung component. This is similar to fits attempted by Ohsuga et al. (2005). Like their trials, we have found that the bremsstralung component is too high when the radio data are fit well by the synchrotron data. In this case, we have a simulation volume which

extends to 28 GM/c^2, while Ohsuga et al. (2005) has volumes which extend to either 10 R_S or 30 R_S (20 GM/c^2 or 60 GM/c^2, respectively). They found adequate fits with the smaller volume with a density maximum of 1x10^{10} particles/cm^3 and with the larger volume at 3.4x10^8 particles/cm^3. As would be expected, our trial lies somewhere between the two. However, it seems unlikely that any skewing of density or temperature will allow a fit to the slope of the quiescent data.

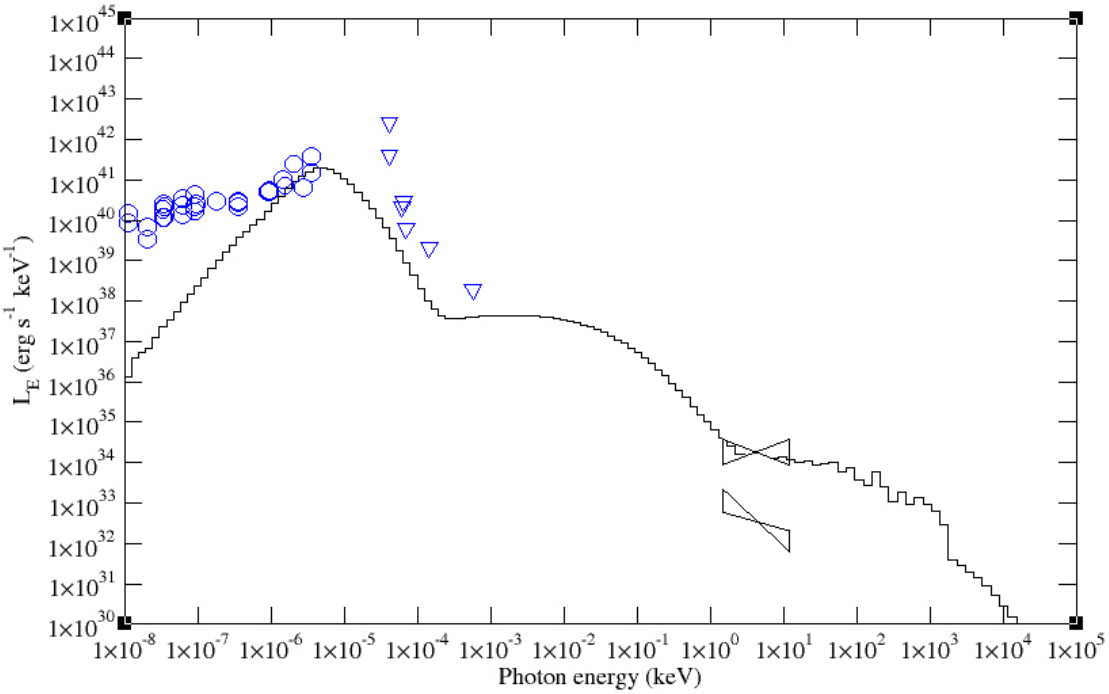

Figure 3.8: Fit to flaring data with second Compton bump component. Maximum values of the 95x95 cell grid are scaled to n = 3.4x10^8 particles/cm3, T = 8.2x10^3 keV, B = 1.6x10^2 G. Total luminosity is 7.5x10^{36} erg/s.

Figure 3.8 shows a fit by lowering density from the bremsstrahlung fit, but compensating by increasing temperature until the flat portion of the twice-scattered Compton bump fits the slope at the flaring point. Total luminosity and the spectral slope at the flaring point suggest this is a good fit -- and the shape of the spectrum seems to allude to a possible fit to the quiescent point's slope if density is allowed to drop. As with

the bremsstrahlung fit, we can compare the density maximum used in this trial to those of Ohsuga et al. (2005). The value here correlates to that group's lower density and higher volume value -- this is reasonable, as we have a significantly higher temperature now.

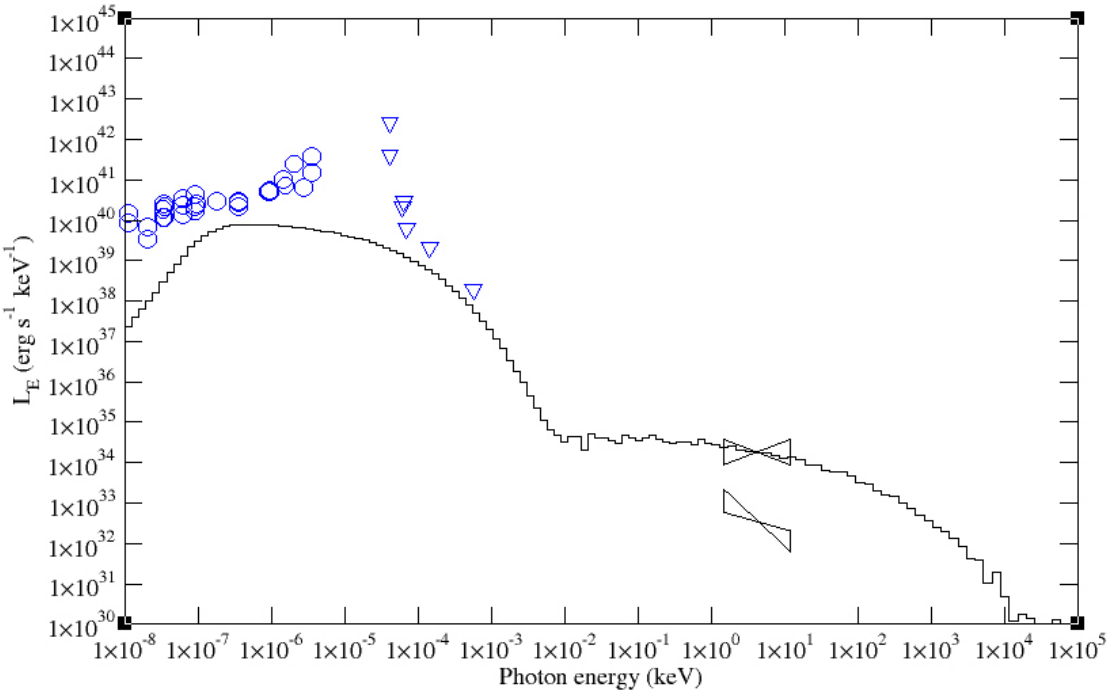

Figure 3.9: Fit to flaring data with first Compton bump component. Maximum values of the 95x95 cell grid are scaled to n = 5.2x10^6 particles/cm3, T = 1.8x10^5 keV, B = 13 G. Total luminosity is 2.6x10^{36} erg/s.

Figure 3.9 shows a fit with low density and high temperature, so the first Compton bump fits the flaring x-ray data point. The synchrotron/synchrotron self-Compton approach was used analytically by Liu et al. (2006), which, while a one zone approximation, found very similar values to our maximums for one of their trials: n = 2.3x10^7 particles/cm^3, T = 1.1x10^5 keV, B = 10.2 G. This fit, like the one above, is promising due to its shape. By lowering only temperature from this value, it appears the quiescent point may be fit with a similar slope.

3.3.2 Quiescent Results

As alluded to above, quiescent fits for the bremsstrahlung trial, second Compton trial by varying the temperature, and first Compton trial by varying the density could be found which intersect the point. However, all of these had nearly zero slopes in L_E, and were therefore unsatisfactory. We present the two quiescent fits which appeared most promising.

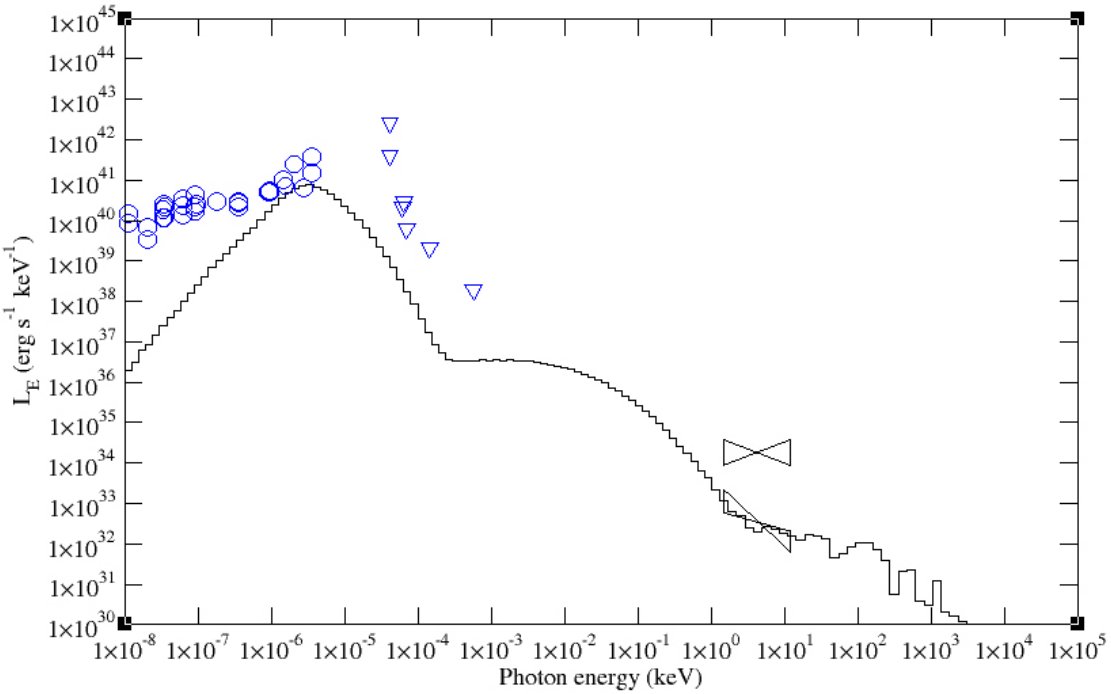

Figure 3.10: Fit to quiescent data with second Compton bump component. Maximum values of the 95x95 cell grid are scaled to n = 6.9x10^7 particles/cm3, T = 8.2x10^3 keV, B = 1.6x10^2 G. Total luminosity is 8.2x10^{35} erg/s.

Figure 3.10 shows a quiescent fit using the second Compton trial shown in Figure 3.8. It should be noted, first of all, that the choppiness in this spectrum is due to lack of statistics in the twice-scattered photons. Optical depth directly along the equator in this case is approximately 1x10^{-3}, leading to a very small population of scattered photons. The slope at the quiescent point is significantly steeper than the previous trial at the flaring point, and fits well the slope required at quiescence. In this case, we have dropped the density by less than a factor of five. This is slightly higher than the accretion variation of

HARM data, a factor of two, but is not extreme. As noted in the variation analysis, variations in the density of accreted matter are not considered by HARM, and therefore, changes of this level are not precluded. The results shown here can be changed greatly by small changes in input values, due to the combination of spectral components required to produce this spectrum.

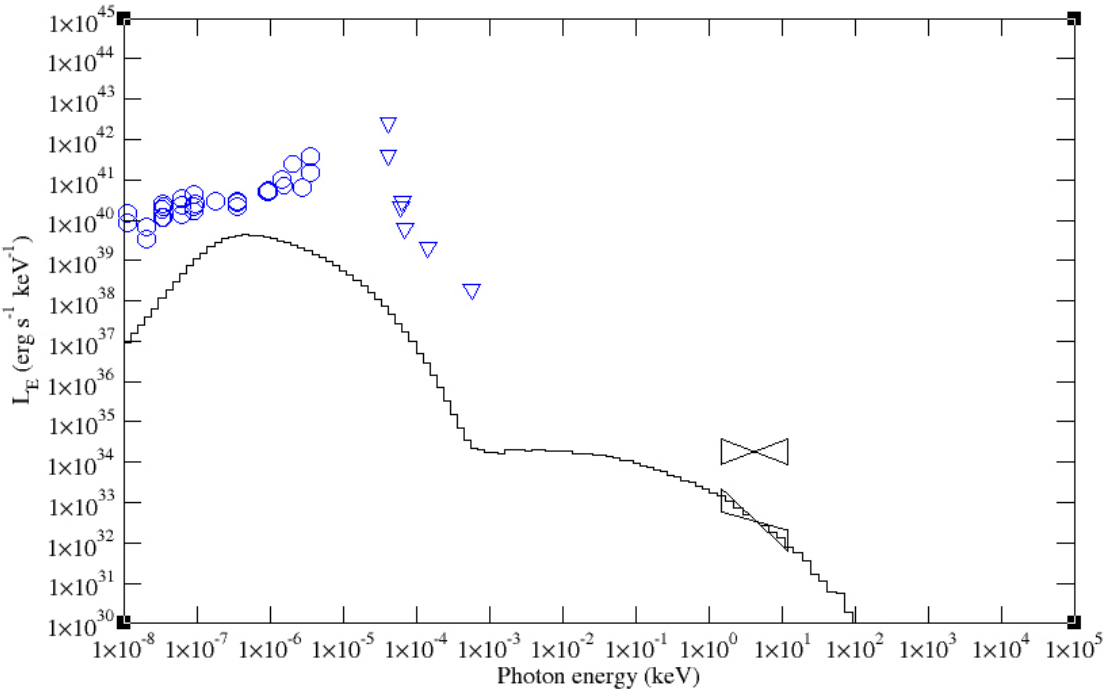

Figure 3.11: Fit to quiescent data with first Compton bump component. Maximum values of the 95x95 cell grid are scaled to n = 5.2x10^6 particles/cm3, T = 4.7x10^4 keV, B = 13 G. Total luminosity is 3.4x10^{34} erg/s.

Figure 3.11 shows the quiescent fit for the first Compton trial shown in Figure 3.9. This fit was obtained by dropping the temperature by about half an order of magnitude. As noted before, without better understanding of acceleration mechanisms, it is difficult to say whether global temperature changes of this scale are feasible or not. However, by this trial, this approach looks promising, and is closely in line with the idea that correlated low and high energy flares arise due to synchrotron radiation -- in this case, the x-ray being fit by an SSC component. This trial gives our best fit to the quiescent data

point's slope.

3.4 Conclusions

We have presented results for coupled physical and spectral simulations of the accretion disk of Sagittarius A*. Fits to flaring x-ray data are shown for three sets of parameters of an entirely thermal plasma, and these results are discussed, noting their similarities to two other recent models made for this same situation. The values used in our trials for all three sets of parameters are quite similar (respectively) to those used by Liu et al. (2006) and Ohsuga et al. (2005), but incorporate additional physics and complexity into modeling.

Of these, the trials which fit the flaring data point with the first Compton bump and second Compton bump show promise to allow fits to the quiescent x-ray data by only changing one physical value. The second Compton bump trial shows a promising fit which intersects the quiescent point by dropping the density, and may be at an appropriate slope. This trial is also the best fit to low energy data while fit to the x-ray points. While intersecting each x-ray point, some of the IR data are fit by the synchrotron bump. The first Compton bump trial shows a very good fit, both in slope and position, to the quiescent point by dropping the temperature, though these trials never match the IR or radio data points. The second Compton bump fit appears approximately valid in comparison to the variations in mass accretion onto the black hole suggested by the HARM output. It should be noted, as reported in Xu et al. (2006), the quiescent state X-ray emission can be attributed to thermal emission from the large scale accretion flow. For this reason, the data point we have fit here could be considered an upper limit.

Overall, we present our second Compton bump trials as our best explanation for the observed spectra of Sagittarius A*. Due to the combination of spectral components at the critical point in the x-ray, we are able to describe a large number of different slopes and locations -- with these being quite sensitive to input values. This may account for the observed variability in x-ray slopes and luminosities.

While our second Compton trial can fit the IR points, it is found that none of our fits can match the radio data well while also fitting x-ray data -- this suggests that a completely thermal approach using GRMHD and one-temperature electrons is lacking in ways that may be improved by using FP techniques or results suggested by recent kinetic simulations of turbulence-heated electron distributions (Liang 2009). It is also possible that a larger simulation volume must be enclosed to fit these points concurrently with the x-ray data.

In the future, this project will turn to some method of consistently introducing nonthermal particle acceleration to determine whether this can provide better fits to the joint radio/IR/x-ray data.

Chapter 4

Numerical Modeling of Multi-wavelength Spectra of M87 Core Emission

Spectral fits to M87 core data from radio to hard x-ray are generated via a specially selected software suite, comprised of the HARM general relativistic magnetohydrodynamic accretion disk model and a 2D Monte Carlo radiation transport code. By determining appropriate parameter changes necessary to fit x-ray quiescent and flaring behavior of M87's core, we assess the reasonableness of various flaring mechanisms. This shows that an accretion disk model of M87's core out to 28 GM/c^2 can describe the inner emissions. High spin rates show GRMHD-driven polar outflow generation, without citing an external jet model. Our results favor accretion rate changes as the dominant mechanism of x-ray flux and index changes, with variations in density of approximately 20% necessary to scale between the average x-ray spectrum and flaring or quiescent spectra. The best fit parameters are black hole spin $a/M > 0.8$ and maximum accretion flow density $n \leq 3 \times 10^7$ cm^{-3}, equivalent to horizon accretion rates between $\dot{m} = \dot{M}/\dot{M}_{Edd} \approx 2 \times 10^{-6}$ and 1×10^{-5} (with $\dot{M}_{Edd}$ defined assuming a radiative efficiency $\eta = 0.1$). These results demonstrate that the immediate surroundings of M87's core are appropriate to explain observed x-ray variability.

4.1 Introduction

It is generally accepted that the center of the Faranoff-Riley type I (FR-I) radio galaxy M87 harbors a supermassive black hole of mass $(6 \pm 0.5) \times 10^9$ M_o (Gebhardt and Thomas 2009) at a distance of 16.7 Mpc (Mei et al. 2007), which is associated with a

spectacular kiloparsec scale jet. Observations of superluminal motion in the jet require a jet viewing angle of $\theta < 19^{\circ}$ and bulk Lorentz factor $\gamma > 6$ at the prominent HST-1 jet knot, which would imply it is located 5.3×10^5 R_s downstream from the core (Biretta et al. 1999), where the Schwarzschild radius of the black hole $R_s = 1.8 \times 10^{15}$ cm (Hardee 2010). Due to its size, proximity, and orientation, M87 provides a unique opportunity for study of a central AGN environment, which can be probed to investigate particle energization in accretion disks, jet launching, and other astrophysical phenomena occurring in these extreme situations.

Its spectral energy distribution suggests that M87 is a misaligned BL Lac. It has been observed for a number of years from radio to gamma rays, and detailed information is available from multi-wavelength collaborations (Acciari et al. 2008, 2010). M87's core is variable, and optical and x-ray bands show common changes of about a factor of two, on timescales of months (Perlman et al. 2003; Harris et al. 2009). Very high energy (VHE) observations of variability on timescales of days (Aharonian et al. 2006) suggest very compact emission regions on the order of the size of the inner accretion disk (Neronov and Aharonian 2007), and concurrent VHE, radio, and x-ray campaigns have helped tie the gamma ray emission from M87, for specific events, to areas close to the core (Abdo et al. 2009).

A number of models have been proposed in recent decades to describe accretion disks in AGN systems with low luminosity, compared to their Eddington luminosity -- an idea which has been referred to as a radiatively inefficient accretion flow (Yuan et al. 2003). Popular among these is the advection dominated accretion flow model, which cites the idea that, close to the horizon, most of the gravitational energy gained by particles is

unable to radiate prior to them being advected onto the black hole (Narayan and Yi 1994). The luminosity of M87 is about $L \approx 10^{-6} L_{Edd}$. Di Matteo et al. (2003) suggests an upper limit to the accretion rate of M87 around $\dot{m} = \dot{M}/\dot{M}_{Edd} = 1.6 \times 10^{-3}$, the Bondi accretion rate, based on gas properties derived from the Compton spectrum, where $\dot{M}_{Edd}$ is the accretion rate at which the Eddington luminosity is reached, assuming a radiative efficiency $\eta = 0.1$, representing the fraction of energy radiated by a typical particle of its total energy. This would suggest that the efficiency of the source is $\eta \approx 10^{-5}$ if it accretes at $\dot{M}_{Edd}$, much lower than the canonical value $\eta = 0.1$ in a standard, efficient thin disk, making it a truly radiatively inefficient source. A more recent estimate by Levinson and Rieger (2011) based on calculated jet power and the capability of the system to extract power from a Kerr black hole suggests an accretion rate $\dot{m} = 10^{-4}$, for a maximally rotating black hole (a/M = 1). Smaller spin values would then suggest higher accretion rates, scaling as $\dot{m} \propto a^{-2}$. These rates may or may not be calculated at the black hole horizon, as some models choose other radii. These accretion rate estimates can help set particle densities in radiative models.

Models based on specific radiative mechanisms have been invoked recently to describe M87's spectrum. For instance, Neronov and Aharonian (2007) suggest a scheme where electrons are accelerated by vacuum gap electric fields, in the black hole magnetosphere, while another paper makes use of centrifugal acceleration to heat electrons which upscatter ADAF disk photons (Rieger and Aharonian 2008). Models such as these which propose novel acceleration methods are generally seeking to explain the heating of electrons to very high energies, which then, through the inverse Compton process, upscatter synchrotron photons to complete the x-ray and VHE spectrum (Hardee

2010).

Recent modeling work has attempted to restrict possible spin rates for M87 via a number of methods. These papers typically use the rapid TeV variability to probe the black hole angular momentum, as in Wang et al. (2008), where the TeV optical depth, assuming ADAF, is shown to strongly depend on the spin, and constrains it to greater than a/M = 0.65. Similarly, the same group, in Li et al. (2009), solve the relativistic hydrodynamical equations in the RIAF scheme to constrain the spin to greater than a/M = 0.8. Advanced TeV imaging is likely to provide a very useful tool to tie down black hole spins in the near future. For this paper, the lower limit on spin for M87 is assumed to be a/M = 0.65, to evaluate how well different spin rates fit the observed SED.

We consider a scenario in which the immediate surroundings of the central black hole are responsible for the radio, infrared, and x-ray emissions observed. This is due to emitting electron populations within the accretion flow and any GRMHD-driven outflows which HARM develops consistently. Moreover, this region may prove to be the origin of VHE emission, though due to the very high energy electrons necessary to produce these through inverse Compton scattering, and the very low photon counts, this is a very difficult part of the spectrum to simulate via Monte Carlo methods. Unlike other recent models focused on the radio-IR emissions, in this paper, we do not attempt to explain the energization method of electrons. Rather, we assume electron temperatures to be a free parameter proportional to the ion temperature due to the compressional heating inherent in MHD accretion methods. The focus for this paper is on the dynamics specific to spin and accretion rates which produce appropriate Compton spectra. This constant electron to ion temperature ratio is a common assumption (Goldston et al. 2005; Moscibrodzka et al.

2009), as there is no consensus on particle heating, and only work which is specifically related to heating mechanisms, such as Shcherbakov and Baganoff (2010), shows evidence against this.

To motivate this constant temperature ratio assumption, recent PIC simulations (Zenitani and Hoshino 2005, 2007; Liang 2009; Liu et al. 2011) demonstrated that magnetic reconnection and current sheet dissipation, which are believed to be the dominant kinetic processes dissipating turbulence driven by the magnetorotational instability, efficiently convert magnetic energy into hot electron thermal energy even in the absence of collisions. Since the saturated MRI magnetic pressure given by MHD simulations scales with ion pressure, it is reasonable to expect the electron pressure heated by collisionless processes to scale with ion pressure. Hence, as discussed above, for our models the electron temperature scales with ion temperature.

This chapter will focus on fitting data in the radio, IR, optical, and x-ray regimes (Section 4.2), particularly the *Chandra*-band x-ray variability, of the SED by calculating physical properties via a GRMHD accretion disk evolution scheme (Section 4.3.1) and applying output to a specialized MC radiation transport code (Section 4.3.2) by our specific modeling method (Section 4.4). Discussion (Section 4.5) and Summary and Conclusions (Section 4.6) will contain interpretations of the data presented, detailing ramifications of results for clarifying the picture of M87's nucleus. Suggestions regarding likely spin rate, accretion rate, and the mechanism of flaring will be presented, and reasonable modeling tasks for the future, based on the results, will be discussed. Finally, Section 4.7 details modifications to the MC code for these types of sources, with highly anisotropic magnetic and velocity fields.

4.2 Observations

M87 has been extensively observed throughout its energy range for decades. Collected here is a full spectrum of data to describe its emissions, all plotted in Figure 4.1. In the radio regime, data is available from the *IRAM* Plateau de Bure interferometer (Despringre et al. 1996) and the *NRAO/VLA* (Biretta et al. 1991). At slightly higher energies, in IR, data is shown from *Gemini Observatory*/OSCIR (Perlman et al. 2001), the *Subaru Observatory*/COMICS, and *Spitzer Space Telescope*/IRS/MIPS/IRAC (Perlman et al. 2007). Next, in optical, Biretta et al. (1991) presented data from the *Palomar* telescope. These lower energy data are all represented as open circles in Figure 4.1.

TABLE 4.1
TABLE OF *Chandra* X-RAY SPECTRA

Label	Date	Flux ($10^{40} erg/s$)	Spectral Index[a]
Flare1	2008-2-16	8.24±0.13	0.62±0.031
Flare2	2008-6-24	5.29±0.11	0.64±0.035
Average	-	2.59±0.055	0.92±0.044
Quiescent	2007-7-31	1.31±0.047	1.08±0.062

NOTE.—*Chandra* data is taken from the 0.2 to 6 keV band.
[a]Index α for a power-law fit: $F_\nu \propto \nu^{-\alpha}$

In hard x-ray, *Swift/BAT* has provided upper limits from observations from 2005-2009 (Ajello et al. 2008, 2009) which are shown as inverted triangles in Figure 4.1. Observations in VHE have also been collected, by HEGRA (Aharonian et al. 2003, 2004), H.E.S.S. (Aharonian et al. 2006), and *Fermi*-LAT (Abdo et al. 2009), with flaring behavior shown from H.E.S.S. LAT data is shown as squares while H.E.S.S. flaring and quiescent data are depicted as diamonds.

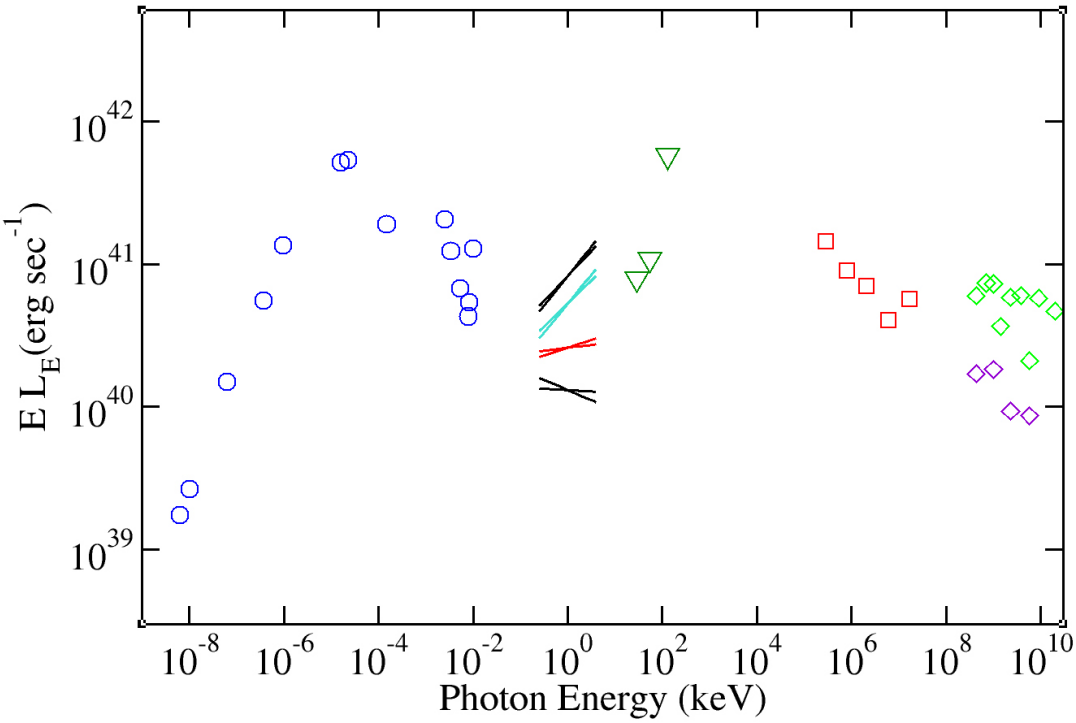

Figure 4.1: SED of M87 in EL_E, to depict the variety of Chandra *x-ray indices. Inverted triangles are* Swift *long-term monitoring upper limits. They will only be used to restrict fits to the average* Chandra *spectrum (shown as the red bowtie), as flares are short-term transients. Lower energy data are shown from* IRAM, NRAO, Gemini, Spitzer, *and* Subaru.

The most important data collected are from the *Chandra* x-ray telescope, which are shown in Figure 4.1 as bowties. Results were first given by Wilson and Yang (2002), and variability data and descriptions of the observations and data used here is presented in Harris et al. (2009). Private communications with Dan Harris, Francesco Massaro, and their group yielded spectral details which allowed for consideration of a variety of quiescent and flaring x-ray spectra. Shown in Figure 4.1 and Table 4.1 are two flaring *Chandra* x-ray spectra, a quiescent spectrum, and an average spectrum obtained by averaging the flux and power law spectral index (α for $F_\nu \propto \nu^{-\alpha}$) of all *Chandra* data. The highest flaring spectrum is significantly greater in flux than any other data point, so this paper will focus on fitting the second flaring point, which is more in line with the

general trend of data. So, any mention of the flaring *Chandra* x-ray spectrum from this point on will refer to the second highest flaring point (Flare2 in Table 4.1). The Flare1 bowtie will be left out of any further figures.

4.3 Simulation Tools

4.3.1 HARM GRMHD Code

The physical values of the accretion disk system are calculated with the 2D axisymmetric HARM GRMHD code, which evolves an accreting black hole system based on a number of simple user-adjustable parameters as described in Gammie et al. (2003) and Noble et al. (2006). From an initial torus perturbed from equilibrium by a small poloidal magnetic field, HARM integrates the GRMHD equations in a conservative scheme to consistently calculate parameters of the accretion flow.

Conserved variables are tracked by evaluating fluxes between simulation cells, and, from these, primitive physical variables such as particle density, internal energy, magnetic field, and velocity, are calculated. For a full description of HARM'S algorithms and method, please see the cited papers (Gammie et al. 2003; Noble et al. 2006).

For our purposes, HARM is set-up with a small number of user-defined parameters, including adiabatic index, black hole spin value, simulation box size, torus position, and a small poloidal magnetic field to seed the torus. From these initial parameters, the accretion disk evolves, governed largely by the MRI, which describes the outward transport of angular momentum in the disk, and generates turbulence in the magnetic field from an initially poloidal field. The physical space is divided into a spherical radial/angular grid, with cells spaced logarithmically in radius, and concentrated

equatorially in the angular dimension. This gives the highest resolution along the equator, at the horizon, where the shortest length scales of importance are located. Figures 4.2 and 4.3 detail results for two trials, differing only in spin rate.

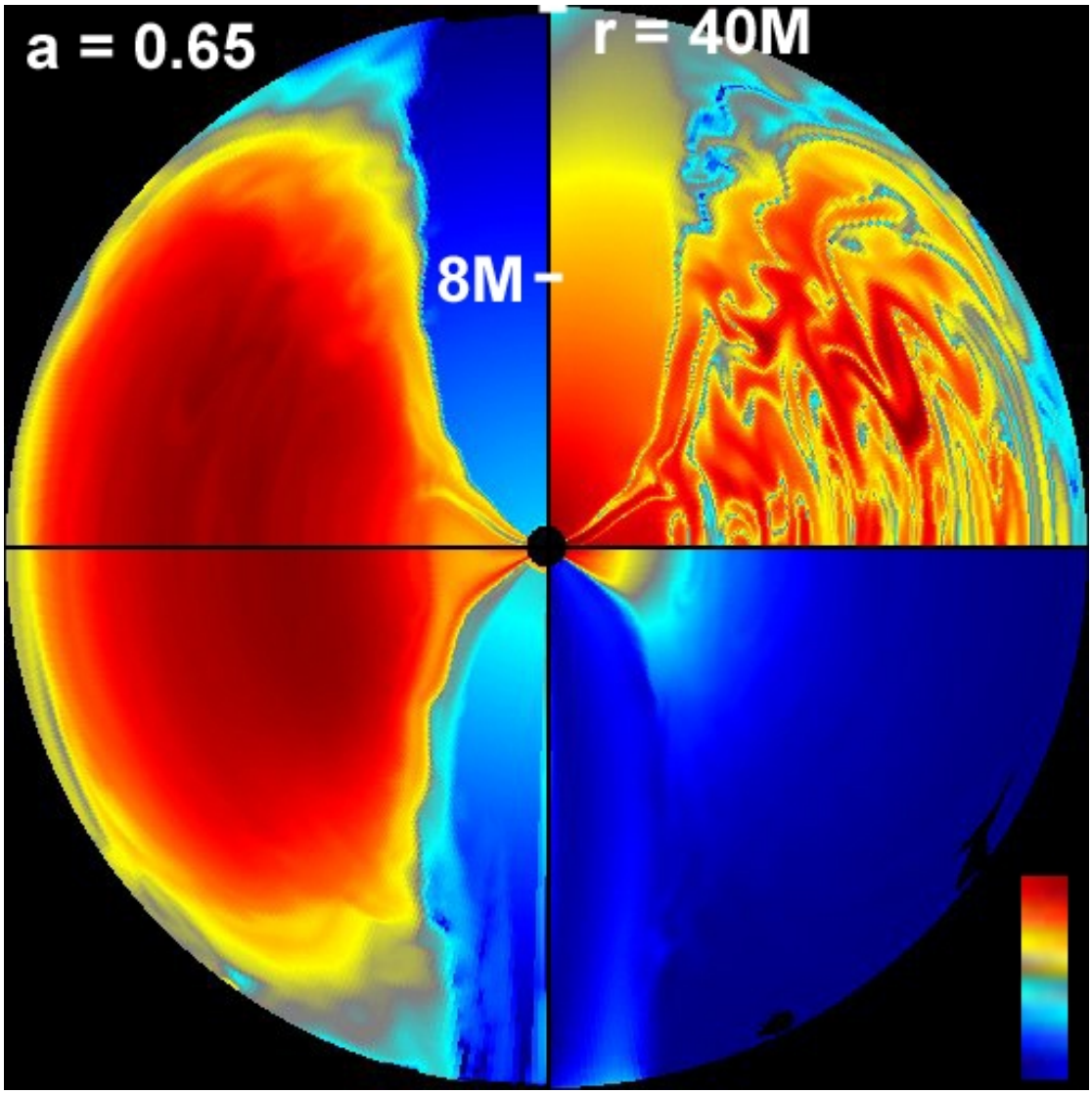

Figure 4.2: Composite image of HARM output, showing data from runs with black hole spin a/M = 0.65, at time t = 2000M. The top and bottom on the left show density and internal energy (temperature times density) plots, respectively. Top and bottom on the right are magnetic field squared and bulk Lorentz factor, respectively. Dark red corresponds to the highest normalized value for each, dark blue to the lowest. Included are marks to depict the radial logarithmic spacing.

In order to construct a useful library of LLAGN results from HARM, we have made a number of overlapping runs, all with an adiabatic index of $\gamma = 5/3$, on grids of

resolution 256x256 and 512x512. These runs span a range of black hole spin value a/M = 0.65, 0.8, 0.9, and 0.99, the last being a near-maximally rotating black hole.

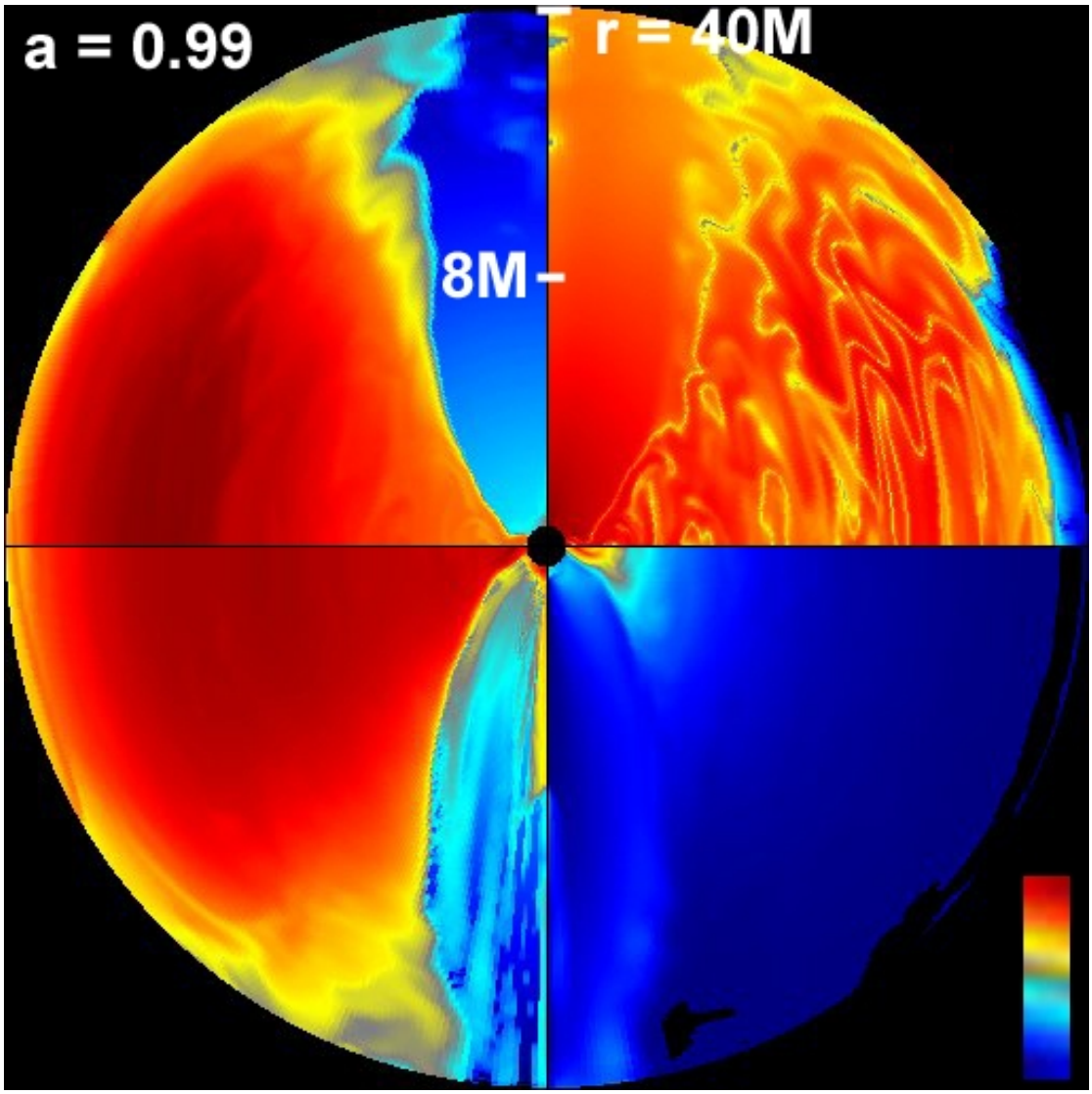

Figure 4.3: Composite image of HARM output, as above, for a run of a/M = 0.99, at time t = 2000M. Important to note is the dramatically stronger polar outflows, particularly visible in the internal energy (lower left) plot. Only the higher spin runs show considerable emission contributions from this region.

To check the effect of including larger simulation volumes, we have also made runs whose outer radii (in GM/c^2) range from 40 to 200. Multiple simulation volumes can also be used to test for convergence of results given by the radiation transport code, given different volumes enclosed. Emissivity curves are shown in Figure 4.4, to give an idea of

the location of peak emission for different radiative mechanisms. Important to note is that the bremsstrahlung curve peaks within r = 22 M, whether larger volumes are considered or not, so most of the region's emissions will be reasonably modeled by using the smaller, better resolved, volume.

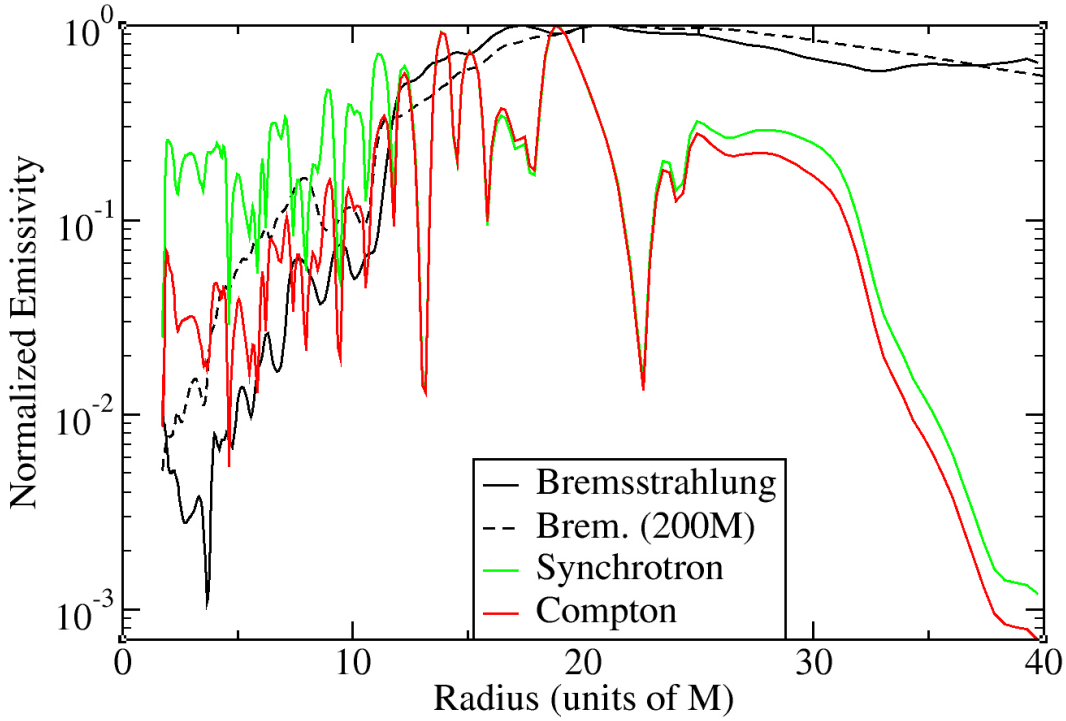

Figure 4.4: Normalized emissivities for a typical a/M = 0.65 run. Shown for comparison as the dashed line is a bremsstrahlung emissivity curve from a HARM run encompassing a volume out to r = 200M. The curve labelled "Compton" is the generalized Compton emissivity, the synchrotron emissivity multiplied by the electron density.

A brief note on the appropriateness of using 2D GRMHD for the problems being investigated: we contend that for our purposes of creating broadband spectra and constraining global parameters, the details of azimuthal modes would be averaged out even if included in full 3D, due to the rapid disk rotation in most of the relevant emission region. That is, the global spectra of a 2D trial should look approximately the same as a 3D trial, given matching parameters. This was noted by Ohsuga et al. (2005) in regard to

Sgr A*, who stated that they checked that final MC-generated spectra were not significantly changed by averaging 3D MHD parameters over azimuth, implying that 3D effects may not be vital to conduct global spectral studies. A primary difference in 3D and axially symmetric simulations is that MRI turbulence decays due to Cowling's anti-dynamo theorem throughout axially symmetric simulations. Due to this, care is taken to select data at t = 2000 M (in black hole units) during the optimally turbulent time following initial in-fall, before the decay phase of the 2D turbulence.

4.3.2 Monte Carlo Radiation Transport Code

The emission spectra based on physical parameters from HARM simulations are calculated by feeding the GRMHD data into our 2D axisymmetric Monte Carlo relativistic radiation transport code (Canfield et al. 1987; Liang and Dermer 1988; Böttcher et al. 2001; Finke and Böttcher 2007; Chen et al. 2011). This simulation scheme allows bremsstrahlung and synchrotron emission, based on the radiative weight of each zone. Emissions are then tracked through the simulation volume, with their energies and photon weights adjusted by absorption and scattering.

All MC runs presented are on a 95x95 cell cylindrical grid, evenly spaced radially and vertically, in constrast to the spherical grid used by HARM (Figure 4.5). The 95x95 grid is much finer than, for instance, 50x50 MC runs which present very similar results. Based on a number of different mesh trials, the data are convergent at this scale. The mapping procedure for physical values, from the HARM grid to the MC code grid, relies on averaging the values for all HARM cells that lie within each (usually much larger) MC code cell. The number of MC photons (each representing a huge number of actual

photons, reflecting the actual emission level of the zone) used for each run is 1 to 10 million. Runs which needed more Compton scattering statistics relied on the photon splitting technique developed by Chen et al. (2011). This significantly increases the quality of scattering statistics, allowing for both more consistent and shorter runs.

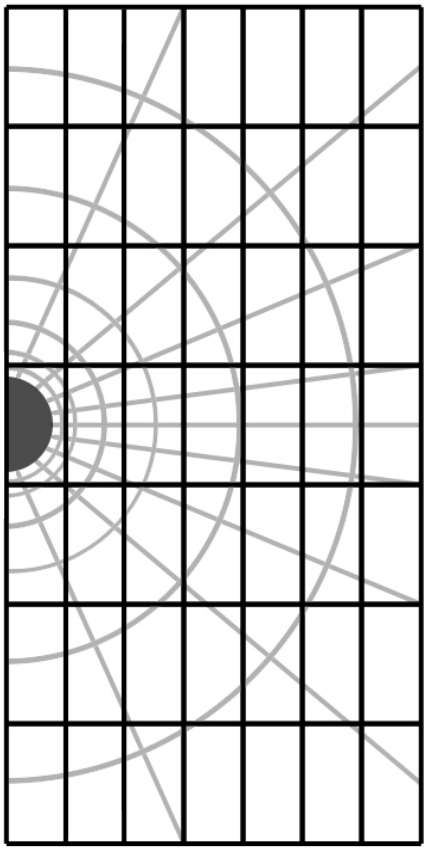

Figure 4.5: Schematic depiction of the MC code (cylindrical, axisymmetric) grid overlaid on the HARM (spherical, axisymmetric, logarithmic) grid. The HARM grid is much finer than the MC grid close to the horizon (shown as a solid semi-circle), and somewhat larger at large radii. In this image, the respective grids are at appropriate ratios to one another through the simulation volume, though the horizon is exaggerated compared to the grid size. In actual simulations, about seven MC cell lengths fit inside a Schwarzschild radius. To model the horizon in the MC code, any cells within its radius are purely absorbing.

This code has the capability to evolve electron distributions based on the Fokker-Planck (FP) equation. Given that the electron-heating mechanism in LLAGN accretion disks is poorly understood and most likely due to collisionless plasma processes, we feel

it is inappropriate to use the FP equation, so it is turned off for all trials. As a first estimate, electrons are assumed to be thermal at a set temperature proportional to ions. Future work will use particle-in-cell (PIC) simulation results on the nonthermal heating of electrons by magnetic turbulence (Liang 2009; Liu et al. 2011).

In order to better model these types of sources, with highly anisotropic magnetic and velocity fields, modifications to the emission and scattering methods of the code were necessary and are detailed in Section 4.7.

4.4 Modeling

Evaluating HARM output to supply input data to the radiation transport code requires several steps, as described in Hilburn et al. (2010):

1) All HARM units scale with a specified black hole mass, so the same runs may be applied to various astrophysical sources. Specifying the black hole mass and a maximum density for the accretion flow yields values throughout the grid for MRI-saturated magnetic field components, ion temperatures due to adiabatic compressional heating, particle densities, and velocity components.

2) The MRI-saturated magnetic field values output by HARM are considered lower limits, as they do not include additional primordial fields (largely azimuthal) that may have been present in the plasma before its accretion. Despite starting with a purely poloidal field, the azimuthal component of the field dominates due to the MRI evolution. When scaling the magnetic field values for MC input, the amplitude is increased and components retain their respective ratios. Because the azimuthal component is dominant to begin with, this approximation is equivalent to adding a primordial azimuthal field.

3) As the electron-heating mechanism in LLAGN accretion disks is poorly understood, a parametrized globally uniform electron-to-ion temperature ratio is applied, as in Goldston et al. (2005) and Moscibrodzka et al. (2009). This ratio is ultimately determined by collisionless (anomalous) heating processes, more efficient than Coulomb collisions. This is acknowledged as a first approximation, and implies that the level of compressional heating of ions is proportional to the total heating of electrons, likely largely from magnetic dissipation. In the future, for more advanced models, we will add a small nonthermal (power-law) component to the thermal population to model the VHE data.

So, given a black hole mass, maximum density, magnetic field value (over the MRI-saturation value), and electron-to-ion temperature ratio, HARM output can be used to compute radiation output. In this case, the maximum value of each parameter is set, and each other cell's value scales accordingly.

4.4.1 Spectral Modeling Results

Typical HARM data was taken at t ≈ 2000 M, before accretion-driven turbulence dies down. At this point, we used the HARM output as input to the MC spectral modeling. The particle densities chosen for models are based on accretion rates suggested in literature. When the maximum particle density is $n = 1 \times 10^{7}$ cm^{-3}, the maximum accretion rate within the simulation volume is $\dot{m}_{max} \approx 10^{-4}$. This is the case for all spin rates, while the accretion rate through the horizon ranges from $\dot{m}_{H} \approx 2 \times 10^{-6}$ up to $\dot{m}_{H} \approx 2 \times 10^{-5}$, depending on the specific model -- higher spin rates have correspondingly lower horizon accretion rates, due to outflows. As the maximum matches the accretion

estimates of recent work, this was chosen as a benchmark for our models. For the rest of the paper, accretion rates will be given as maximum values as these are similar between models with differing spin rates. In order to evaluate the impact of a higher or lower accretion rate, two other maximum densities were chosen: $n = 3 \times 10^6$ cm^{-3} and $n = 3 \times 10^7$ cm^{-3}, for maximum accretion rates of $\dot{m}_{max} \approx 3 \times 10^{-5}$ and $\dot{m}_{max} \approx 3 \times 10^{-4}$, respectively. Full trials were then performed using these three densities, leaving two parameters for adjustment: electron temperature and magnetic field.

As the main interest in fitting spectra is to evaluate the origin of flaring mechanisms, runs are chosen for their fits to x-ray data. The starting point for each density is then to fit the average x-ray spectrum, whose flux and index are averaged over all *Chandra* x-ray data, not including those with possible pile-up.

Figure 4.6 shows the effect of changing each parameter (density, temperature, and magnetic field) by a factor of two. Obviously, temperature and density have a significant impact on the spectral shape at the x-ray spectrum, each hardening the spectrum when raised. Conversely, the magnetic field, in general, uniformly changes the flux throughout the x-ray spectrum, without changing the x-ray spectral index considerably. This is because increasing the magnetic field increases the flux of the synchrotron curve at the same rate it increases that of the Compton components, as the upscattered photons are synchrotron in origin.

As the density in each trial is fixed, this means that the obvious method of fitting spectra is to vary temperature to fit spectral index while varying magnetic field to fit flux, until the average x-ray bow-tie is satisfactorily fit. It should be noted that, in general, higher black hole spin rates lead to higher densities at small radii, where velocities of the

accreting matter are much greater. Higher velocities lead to harder spectra due to Doppler boosting, so higher spin trials have lower indices, for similar parameters.

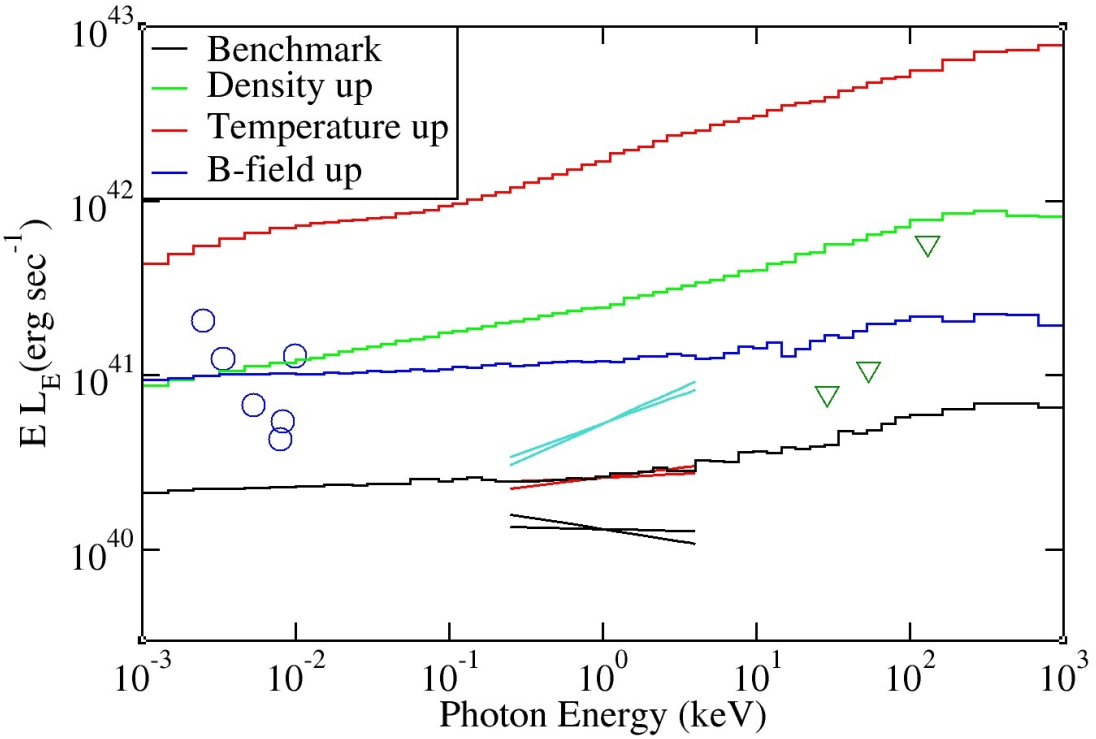

Figure 4.6: A benchmark fit at a/M = 0.9, n = 1 x 10^7 cm^{-3}, and three spectra generated by alternately raising a single parameter by a factor of two. This is shown in EL_E, to better depict index changes in x-ray. As three trial densities have been chosen, this leaves temperature changes to fit index, while magnetic field can be scaled for overall normalization.

Once full trials were completed to fit the average x-ray spectrum -- for each of the three density points, and for each of the four black hole spins -- the quiescent and flaring spectra needed consideration. Given that the flaring mechanism is unknown, the simplest changes to interpret involve varying a single parameter each time. Specifically, if a change in accretion rate is responsible for the flaring behavior, we approximate it by a global density change at fixed temperature. If an increase in electron heating is responsible, we model this by a global temperature change at fixed density. For this reason, a full suite of trials has been done which fit the quiescent and flaring x-ray spectra

by changing merely one of these (maximum density, maximum electron temperature) from the benchmark model which fit the average x-ray spectrum.

Since the n = 1 x 10^7 cm^{-3} runs have the closest accretion rate to that suggested in literature ($\dot{m}_{max} = 10^{-4}$) these runs were evaluated first. The fits for each spin rate are normalized to match the flux of the average x-ray spectrum. In general, these are poor fits to radio, IR, and optical data. Because the higher spin rates lead to larger densities at higher accretion velocities, and therefore harder spectra, the a/M = 0.99 trial had to use the lowest temperature value, and, conversely, the 0.65 trial the highest, to fit the slope of the x-ray data. This leads to the lower spin rates providing better fits at low energies, as the synchrotron flux is higher. However, none of these adequately fit any of the low energy spectrum, so the quiescent and flaring fits are not considered.

The fits for the n = 3 x 10^6 cm^{-3} runs, which yields an accretion rate lower than suggested by literature, are qualitatively similar to those discussed above. They fall short at the radio-IR range; therefore, quiescent and flaring trials are again not considered.

4.4.2 Fits using a density of 3x10^7 cm^{-3}

The third set of fits uses a density of n = 3 x 10^7 cm^{-3}. This corresponds to an accretion rate above the recently quoted value, but still well below the Bondi accretion rate which has been suggested as an upper limit to the level of accretion. The Bondi accretion rate defines spherical accretion onto a compact object, $\dot{M} = \pi R^2 \rho v$, where ρ and v are the density and sound speed, respectively, of accreting matter, and R is the characteristic radius found by equating the object's escape velocity and relevant sound speed (Di Matteo et al. 2003).

As seen in Figure 4.7, these spectra offer good fits to radio, IR, and optical data, unlike lower density trials. The second big change is the visibility of the shoulder of the bremsstrahlung emission in hard x-ray, above *Chandra* energies. This is the first time here the upper limits from *Swift* data (Ajello et al. 2008, 2009) require consideration. As *Swift* data are averaged limits over several years, they only restrict fits to the average *Chandra* x-ray spectrum, but they are still right at the edge of all the spectra with this density. Essentially, as bremsstrahlung emission scales as density squared, this puts a limit on maximum model density at $n = 3 \times 10^7$ cm^{-3}.

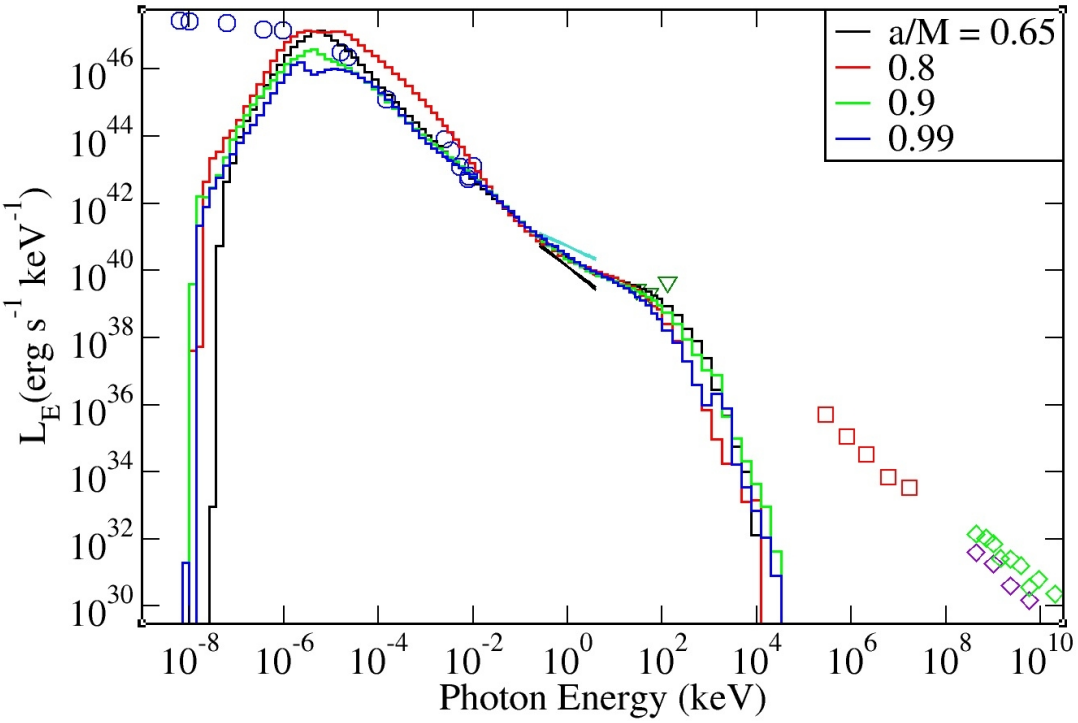

Figure 4.7: n = 3 x 10^7 cm^{-3} runs. Lower density trials were unable to fit lower energy data. Shown below are quiescent and flaring fits, with parameters scaled from these benchmark runs.

While the a/M = 0.8 trial overestimates much of the low energy data, three of the four fits shown above are approximately equally good through the radio, IR, and optical bands. All also fit with a nearly pure power-law at the average x-ray spectrum, and come

close to the *Swift* x-ray upper limits. The only fit which lies comfortably beneath the *Swift* upper limits is the a/M = 0.99 run. This is due again to the fact that with higher spin runs, the emitting/scattering electron populations are moving with higher maximum bulk velocities. This means that the maximum temperature can be turned down considerably while still maintaining the appropriate x-ray index, thereby moving the bremsstrahlung cut-off to a substantially lower energy than the other trials.

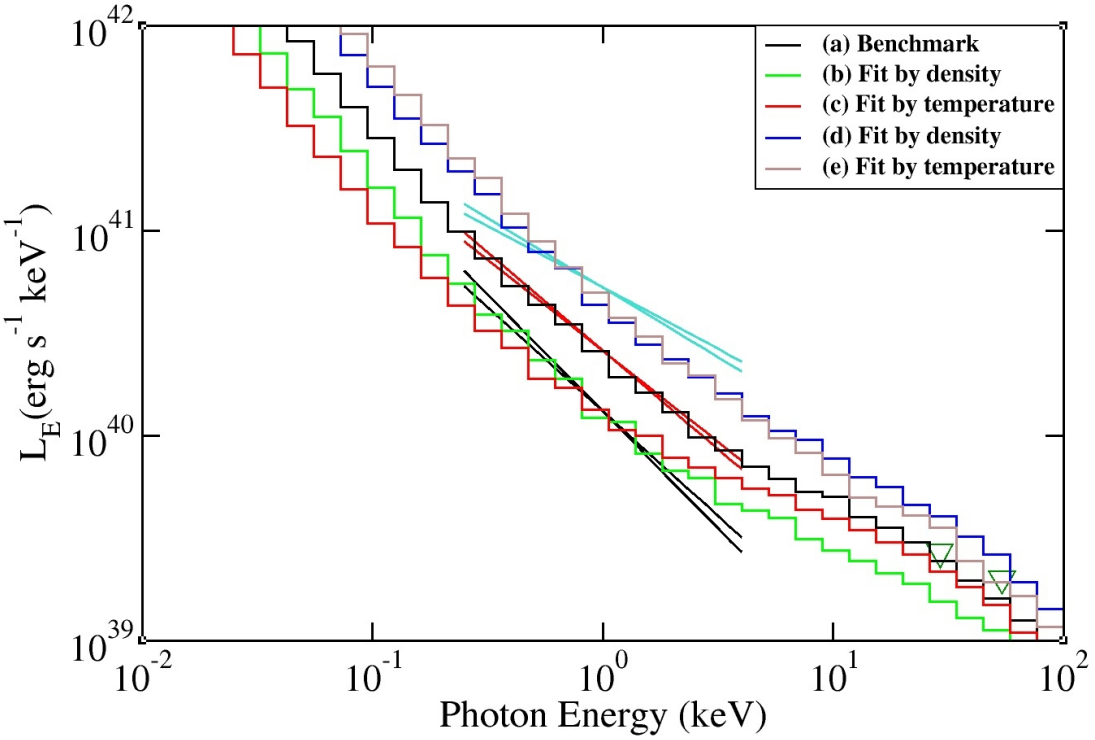

Figure 4.8: a/M = 0.9, with n = 3 x 10^7 cm^{-3}. These views are zoomed in to focus on the x-ray spectra, to better show changes in index here. (a) is the average fit shown above. Fits to quiescent data, (b) and (c) are varied from (a) in density and temperature, respectively. Flaring fits (d) and (e) are varied in density and temperature, respectively. That is, (c) and (e) are changed only in temperature from (a), and similarly for (b) and (d) in density.

The quiescent and flaring fits shown in Figure 4.8 are for the runs with a/M = 0.9. Shown as (a) is the average fit shown in the zoomed out image above (Figure 4.7). As detailed in the fitting methodology, the quiescent and flaring fits are changed from the average data fit in only one parameter: either temperature or density. Spectra (c) and (e)

are changed only in temperature from the benchmark (a), while (b) and (d) are changed only in density.

Either quiescent trial could be seen to fit the quiescent spectrum reasonably; its index is quite similar to the average spectrum. The bremsstrahlung shoulder is more visible at this energy than for the average trial, and because the density fit drops this a bit lower than the temperature fit, it maintains the quiescent slope better.

The flaring trials are, at first glance, quite poor. The amount of change in index to the flaring spectrum is much more noticeable than to the quiescent spectrum. Again, the bremsstrahlung cut-off plays a large role in these fits. Turning up the temperature does not get the bremsstrahlung slope up to the flaring spectrum, but turning up the density does. Because of this, it can be seen that a small change in density can yield a large change in x-ray spectral index. Specifically, the lower energy spectrum for the flaring x-ray density fit has a much higher index, while the higher energy portion has an index quite close to the flaring spectrum.

In general, the fits by changing density are better at fitting the quiescent and flaring data spectra, largely due to the fact that the extreme index change to the flaring spectrum can be explained by the presence of the bremsstrahlung bump. The other spin values considered, a/M = 0.65, 0.8, and 0.99, yielded similar results to the previous trials. Most noticeable in each case is that the density fits are significantly better than the temperature fits, suggesting again that accretion rate variations may be more reasonable to suggest as the dominant flaring mechanism.

4.5 Discussion

The sample fits immediately suggest that a density higher than n = 1 x 10^7 cm^{-3} is necessary to yield an adequate fit to the radio, IR, and optical spectra. The n = 3 x 10^7 cm^{-3} runs have some conflict with the Swift upper limits in the hard x-ray regime, which restricts the accretion rate to $\dot{m}_{max}$ = 3 x 10^{-4}. These upper limits are only considered for the average *Chandra* x-ray data fits, as they are essentially averages over a number of years.

TABLE 4.2
TABLE OF MODEL AVERAGE X-RAY FITS FOR $n = 3 \times 10^7$ CM^{-3}

Label	Spin (a/M)	Magnetic Field	Field Scaling[a]	Temperature	Density	Fit to:	*Chandra* Index[b]	Model Index[b]
1	0.65	2000 G	62.5	15 MeV	3×10^7 cm^{-3}	Average	0.92±0.044	0.90
2	0.8	2600 G	47.3	20 MeV	3×10^7 cm^{-3}	Average	0.92±0.044	0.85
3	0.9	500 G	6.1	22 MeV	3×10^7 cm^{-3}	Average	0.92±0.044	0.92
4	0.99	460 G	2.9	7 MeV	3×10^7 cm^{-3}	Average	0.92±0.044	0.86

NOTE.—The indices shown are in the energy band from 0.2 to 6 keV, both for *Chandra* data and model fits. Magnetic field, electron temperature, and electron density values given are the maximum for each within the simulation grid, which all other cells scale to.

[a]This value is the factor the GRMHD MRI-saturated magnetic field had to be scaled by to appropriately normalize MC output, as discussed in the text.

[b]Index α for a power-law fit: $F_\nu \propto \nu^{-\alpha}$

As it is expected that a larger simulation volume for the accretion flow would only add significantly to the bremsstrahlung flux, n = 3 x 10^7 cm^{-3} can be seen as an upper limit to the density maximum. This is because of the artificial initial condition of a small-radius torus, rather than near Bondi-scale accretion.

The details of the average x-ray fit benchmark MC trials are shown in Table 4.2. These include the physical parameters of the runs (electron temperature, density, and magnetic field), *Chandra* spectrum fit to, and data and model spectral indices.

As discussed above, we focus on the n = 3 x 10^7 cm^{-3} trials as these gave the best fits to radio-IR-optical data. There are four different spin rates to consider: a/M = 0.65, the lower limit suggested in literature, 0.8, 0.9, and 0.99, a near-maximally rotating black hole. The fits to *Chandra* spectra don't allow much differentiation between these trials, as they yield very similar results. Spectral indices range from α = 0.85 to 0.92, close fits to

the *Chandra*-given 0.92.

Also of interest in Table 4.2 are the specific parameters required for fits. The general trend is that lower spin runs require higher electron temperatures and magnetic fields to match appropriate spectral properties. HARM runs conducted to test the response of the simulation to additional primordial toroidal fields have shown the MRI development is approximately the same (with higher final field values) for field scaling up to an order of magnitude. Beyond this, the large magnetic pressure dominates the simulation, inhibiting accretion. This allows an easy evaluation of the average fit models, as the 0.65 and 0.8 spin runs require much higher field scaling, while the 0.9 and 0.99 trials are more reasonable.

TABLE 4.3
TABLE OF MODEL FLARING/QUIESCENT X-RAY FITS FOR $n = 3 \times 10^7$ CM^{-3}

Label	Spin (a/M)	Scaling factor	Fit to:	Fit by:	*Chandra* Index[a]	Model Index[a]
5	0.65	0.87	Quiescent	Temperature	1.08±0.062	0.67
6	0.8	0.75	Quiescent	Temperature	1.08±0.062	0.55
7	0.9	0.86	Quiescent	Temperature	1.08±0.062	0.70
8	0.99	0.80	Quiescent	Temperature	1.08±0.062	0.64
9	0.65	0.83	Quiescent	Density	1.08±0.062	0.80
10	0.8	0.77	Quiescent	Density	1.08±0.062	0.99
11	0.9	0.83	Quiescent	Density	1.08±0.062	0.88
12	0.99	0.77	Quiescent	Density	1.08±0.062	0.87
13	0.65	1.13	Flaring	Temperature	0.64±0.035	0.99
14	0.8	1.25	Flaring	Temperature	0.64±0.035	1.00
15	0.9	1.14	Flaring	Temperature	0.64±0.035	1.02
16	0.99	1.19	Flaring	Temperature	0.64±0.035	1.03
17	0.65	1.22	Flaring	Density	0.64±0.035	0.93
18	0.8	1.33	Flaring	Density	0.64±0.035	0.84
19	0.9	1.20	Flaring	Density	0.64±0.035	0.94
20	0.99	1.27	Flaring	Density	0.64±0.035	0.89

NOTE.—The scaling factor given is the factor either the electron temperature or electron density is multiplied by from the average benchmark fit (see Table 2) to get a new value for the quiescent or flaring fit presented.

[a]Index α for a power-law fit: $F_\nu \propto \nu^{-\alpha}$

4.5.1 Flaring and Quiescent Fits

Table 4.3 details quiescent and flaring spectral fits, as well as describing the

change necessary for each fit, from the benchmark average fits, for each spin value. The 0.65 and 0.8 trials details are included for completeness, but will not be discussed extensively. As mentioned previously, their magnetic field scaling values suggests they may not be reasonable spin values, and the qualitative analysis is very similar to that of higher spin rate trials.

The quiescent spectrum is very close in spectral index to the average spectrum. It can be fairly easily fit by decreasing density from the average fit's parameters. Lowering temperature yields a slightly less satisfactory fit at the quiescent spectrum, with a spectral index too low, and spectrum too hard. For every trial conducted, regardless of spin, the density fits showed closer fits to *Chandra* data (with quiescent spectral index $\alpha = 1.08$) than the temperature fits. Specifically, the 0.99 spectrum (benchmark $\alpha = 0.86$) became slightly softer ($\alpha = 0.87$) as expected for the density adjustment, while scaling temperature led to a harder spectrum ($\alpha = 0.64$). The 0.9 spectrum (benchmark $\alpha = 0.92$) became harder with density scaling ($\alpha = 0.88$), but this is still significantly better than the temperature-adjusted trial ($\alpha = 0.70$).

Flaring fits are more complicated to achieve. Because the spectral index is quite a bit lower than that of the average fit -- and the change between indices is much greater than between the average and quiescent -- it is nearly impossible to fit the flaring spectrum by simply adjusting one parameter. However, the fact that the bremsstrahlung emission is visible here, whereas it wasn't in the lower density trials, means that density changes can have a large impact on where in the energy band the change from Compton spectrum to bremsstrahlung spectrum occurs. At this density, $n = 3 \times 10^7$ cm^{-3}, the bremsstrahlung spectrum dominates at an energy around several keV. Therefore, when

the density is increased, and the bremsstrahlung component is increased more than the Compton component, the bremsstrahlung emission is visible down closer to 1 keV.

To demonstrate, the bremsstrahlung spectrum above 1 keV (for the run with $n = 3 x 10^7 cm^{-3}, a/M = 0.9, average fit) much better describes the hard index at the flaring spectrum than the softer Compton spectrum. Specifically, a power law fit from 0.2 to 1 keV has an index $\alpha = 1.13$, while a fit from 1 to 6 keV has an index $\alpha = 0.69$. Fitting the full range from 0.2 to 6 keV yields an index $\alpha = 0.92$. These compare to *Chandra* x-ray spectral indices of 1.08 for the quiescent spectrum, 0.64 for flaring, and 0.92 for average. As the *Chandra* x-ray data ranges from 0.2 to 6 keV, it is clear that small changes in parameters could lead to any of the three of these fits being appropriate throughout the range.

None of the fits shown exactly traces the flaring spectrum, but it is simple to see that the density variations work better than temperature variations, and the density fits show promise at slightly higher energies to fitting the flare spectral index. Quantitatively, the *Chandra* flaring data (with spectral index $\alpha = 0.64$) is better fit by density changes ($\alpha = 0.94, 0.89$ for spin 0.9, 0.99) than by temperature changes ($\alpha = 1.02, 1.03$ for spin 0.9, 0.99). For both spin rates, density fits are more consistent with data.

4.5.2 Model Tests and Evaluation

With both flaring and quiescent spectra better fit from the average spectrum by density changes, it is worth considering how much the density has to be changed for these fits. From the starting density of $n = 3 x 10^7 cm^{-3}$, the quiescent spectrum was best fit with an average of $n = 2.4 x 10^7 cm^{-3}$. Similarly for the flaring spectrum, an average of n = 3.7

x 10^7 cm^{-3} was required. This suggests changes in accretion rate, from the average fit, of about 20-25%. As discussed previously in Hilburn et al. (2010), mass accretion rates vary in HARM trials by about a factor of two. Similarly, Dexter et al. (2009, 2010) suggest variability up to about 50% for both 2D and 3D Sagittarius A* models. Both of these examples comfortably allow for the density variations required for fits.

Following Moscibrodzka et al. (2011), we consider the size of the 230 GHz photosphere from our models, to compare to VLBI measurements by Fish and Doeleman (2010) which found structure at this frequency on the scale of several Schwarzschild radii. All four spin trials had photospheres within 10M, with higher spin trials having smaller photospheres, as expected. Clearly, accretion flow models are consistent with current VLBI results.

The assumption that radiative cooling is unnecessary in the GRMHD calculation is motivated by the flow being radiatively inefficient. The typical 0.9 spin average run has a radiative efficiency of $\eta \approx 10^{-2}$, an order of magnitude less than the canonical value $\eta \approx 10^{-1}$ for an efficient thin disk.

Based on the trials done, there is little to choose between the different spin rates considered. The 0.9 and 0.99 runs are more likely than lower spin trials due to the primordial magnetic fields required. Of these, the 0.9 run may be marginally better at low energies, but not definitively so. On the other hand, the density changes are definitely better than the temperature changes, suggesting that changes in accretion rate are most likely to explain flaring behavior, based on these trials.

4.6 Summary and Conclusions

To explore flaring mechanisms at play in M87's core, full trials have been conducted using a GRMHD accretion evolution scheme, to solve for global physical parameters, and a novel MC radiation transport code, to generate spectra from these parameters. The flaring data being displayed is in the *Chandra* x-ray band. Trials are fit to an average x-ray spectrum, and then changes necessary to fit quiescent and flaring x-ray spectra are discussed, along with ramifications of specific changes.

To evaluate likely spin rates, with literature suggesting $a/M \geq 0.65$, four different GRMHD runs are used, with $a/M = 0.65$, 0.8, 0.9, and 0.99. Articles also suggest an accretion rate under $\dot{m} = 1.6 \times 10^{-3}$, but above or around $\dot{m} = 1 \times 10^{-4}$. To take this into account, the maximum density assigned was adjusted to provide sets of runs at $\dot{m}_{max} \approx 3 \times 10^{-5}$, 1×10^{-4}, and 3×10^{-4}.

Only the highest accretion rate trials, which correspond to a maximum density of $n = 3 \times 10^{7}$ cm^{-3}, manage to fit lower energy data adequately, and so were focused upon for fitting the flaring x-ray spectrum. This density also shows that higher average accretion rates are unlikely, as the bremsstrahlung emission is very close to upper limits provided by the Swift hard x-ray data. As including larger volumes can only maintain or raise the bremsstrahlung flux, this places an upper limit on maximum density and accretion rate.

Quiescent and flaring fits were presented which require only changing density or temperature from the average fits. This can simulate either a global accretion rate change, or a global electron temperature change -- indicative of more efficient electron heating. During none of these trials was the magnetic field changed in fitting quiescent and flaring spectra, in order to isolate the parameter changes.

The quiescent x-ray spectrum has a very similar spectral index to the average x-ray spectrum. Because of this, it is fairly simple to get a close fit by simply dropping either temperature or density from the average spectrum. In general, no spin rate stands out as having outstanding quiescent fits. They all exhibit similar behavior: the density-changed trials have a slightly better index, while the temperature-changed trials are a bit too hard at the quiescent spectrum.

The flaring spectrum is more difficult to explain. Unlike the quiescent spectrum, the flaring spectrum's index is substantially harder than that of the average spectrum, suggesting a much harder spectrum. Again, no spin rate displays perfect fits. These actually look worse than the quiescent fits, because in order to explain both the slope and flux changes, the bremsstrahlung bump has to be enhanced. This leads to a transition between Compton and bremsstrahlung dominance essentially right at the x-ray data, so that small changes can lead to the x-ray points falling on either side of this transition. In general, the higher energy (bremsstrahlung) side of the x-ray runs seems to adequately describe the index at the flaring spectrum, while the lower energy (Compton bumps) side traces the average and quiescent spectra well, but this is very parameter-sensitive.

Overall, the a/M = 0.9 and 0.99 spin runs are marginally better than lower spins at fitting all three x-ray spectra considered, and the $n = 3 \times 10^{7}$ cm^{-3} trials were the only ones which provided a good fit to radio-IR data at all. This suggests that a maximum accretion rate $\dot{m}_{max} \leq 3 \times 10^{-4}$ and spin of a/M > 0.8, both well within limits established in literature, are the most appropriate for the core of M87. Scaling between the average x-ray spectrum and flaring and quiescent spectra requires only simple changes in accretion rate (≈ 20%).

It may be important to note that the higher spin trials have the most prominent

polar outflows and show significantly more emission from this assumed jet base than lower spin rates. These trials are entirely thermal, though jet emission is likely to be non-thermal, and as Dexter et al. (2011) show, the core spectrum can also be fit with non-thermal jet-dominated or jet-and-disk models.

Future modeling work on this source will focus both on more detailed fits of the data already considered, as well as fits including Fermi and VHE data, which was not used in this paper. Continued observations of M87 by *Chandra* and *Swift*, which can be used to confirm the trend seen in flux vs. index, can help to prove the validity of this work. Specifically, observation of two clear trends can show that the bremsstrahlung and Compton components do both need to be included to fit the flaring spectrum depicted.

Furthermore, more accurate and consistent electron heating mechanisms, involving particle-in-cell simulation results, should lead to better-described electron distributions. Recent results have suggested that particle acceleration by magnetic reconnection in similar situations to MRI disks display a dual Maxwellian nature -- with one major population at a low energy, and a higher temperature second population. As the spectral indices already considered should be fairly appropriate extended to the VHE regime, this seems quite promising to describe the spectrum more completely. However, since the Fermi-VHE spectral index is softer than the *Chandra* x-ray index, any additional nonthermal electron component invoked to model those high energy data will not impact the thermal spectral fitting to the lower energy data performed here.

4.7 Monte Carlo Code Modifications

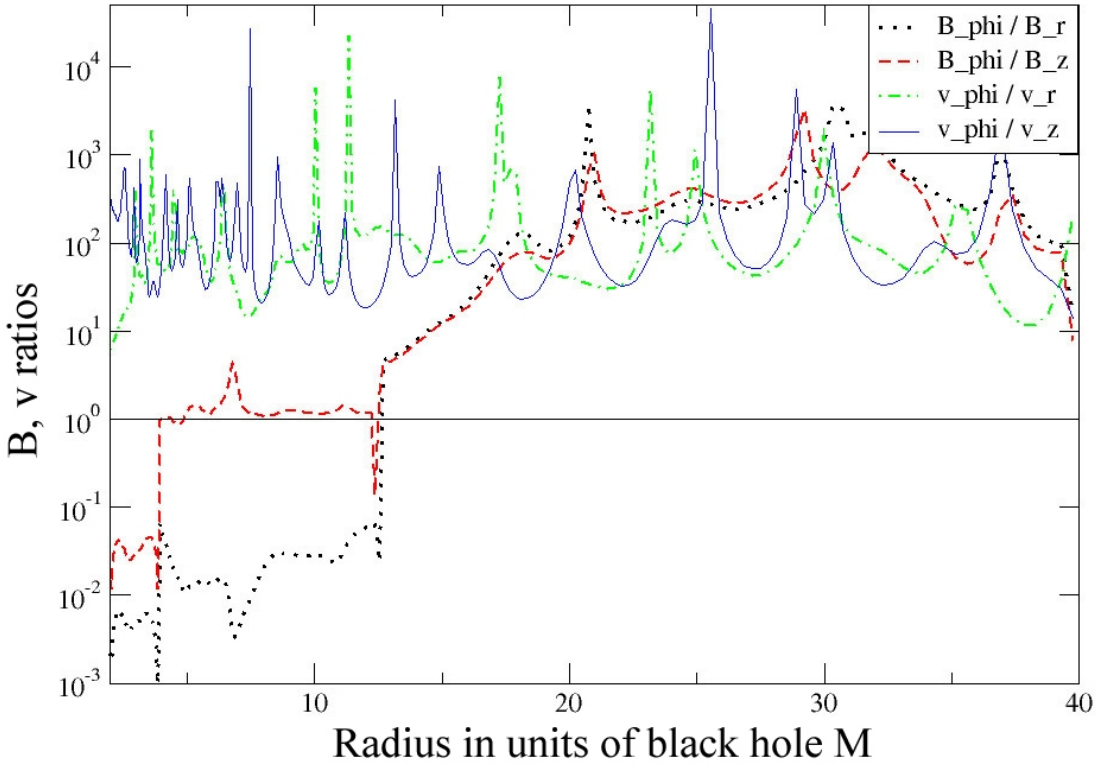

Figure 4.9: Ratios of components of magnetic field and velocity for a HARM GRMHD run of black hole spin a/M = 0.99. The line at unity emphasizes the high degree of anisotropy in these components.

Data from HARM suggest two shortcomings to the MC code, namely the anisotropy in velocity and magnetic field. As shown in Figure 4.9, for a typical run of a/M = 0.99, the components of these parameters are usually very disparate. This will obviously lead to highly anisotropic synchrotron radiation and scattering characteristics, for adequately high fields and velocities. The MC code previously considered synchrotron emission as angle-independent and did not allow for relativistic beaming, boosting, and scattering. In order to create a tool as consistent as possible for a number of astrophysical sources, these issues needed to be addressed in the MC code.

4.7.1 Anisotropic Magnetic Field

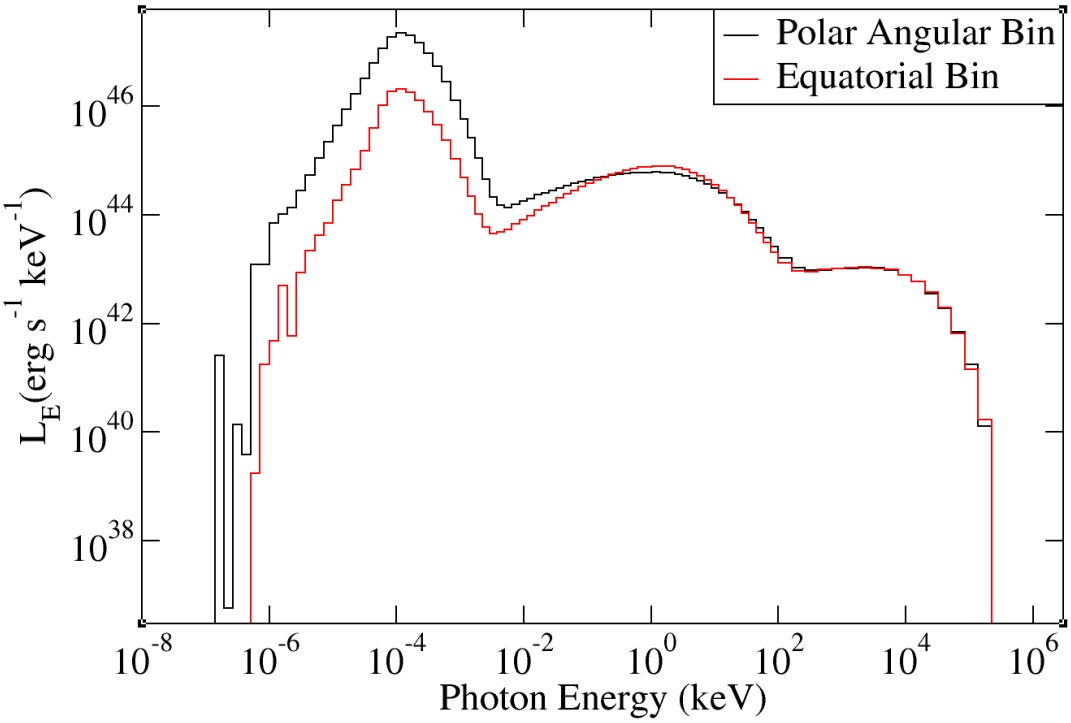

Figure 4.10: Trial of the anisotropic magnetic field modifications. This is a single zone run with nearly purely radial field, to best show the effect of the changes. As expected, the synchrotron emission is strongly biased toward the polar direction, which is always perpendicular to the radial magnetic field, while the Compton components are much more isotropized.

For fields of the magnitude expected in AGN accretion disks, the dominant effect is on the direction of emission of synchrotron radiation. By Petrosian (1981), for semi-relativistic temperatures, the emission scales as:

$$j_\nu(\theta) \propto \exp\{-\frac{\nu}{\nu_b}[\frac{4.5}{\sin\theta}(\frac{\nu_b}{\nu kT})^{2}]^{1/3}\}$$

while for non-relativistic temperatures, emission scales as:

$$j_\nu(\theta) \propto (\frac{1+\cos^2\theta}{\sin^2\theta}) \exp[-(\nu/\nu_b)\ln(2\nu_b/e\nu kT\sin^2\theta)]$$

where ν is the photon frequency, $\nu_b = eB/2\pi m_e c$ is the gyrofrequency, B is the magnetic field, T is the electron temperature, and θ is the angle between photon travel and field direction. In an accretion disk, the toroidal magnetic field is often highly dominant.

The impact is that photons are emitted strongly perpendicular to this direction.

To best depict the effect, Figure 4.10 shows a run with a nearly purely radial magnetic field. This results in a much larger number of photons emitted perpendicular to rather than parallel to fields, which leads to a greater flux in the polar direction than the equatorial direction.

4.7.2 Anisotropic Velocity Field

As the impact will be seen in both emission and scattering events, the process of including plasma flow velocity requires changes to several of the MC code's routines:

1) All emission is beamed in the direction of relativistic plasma flow, and Doppler boosted, by the usual formulae:

$$\cos\theta = \frac{\cos\theta' + \beta}{1 + \beta\cos\theta'} \quad \text{and} \quad \omega = \omega'\gamma(1 + \beta\cos\theta')$$

where θ is the angle between the photon and bulk flow directions, ω is the photon frequency, β is the bulk flow magnitude as a fraction of the speed of light, and ' represents the bulk flow frame.

2) Compton scattering frequency increases when photons travel against the flow of particles (head-on), and decreases when moving with the flow (tail-on), as $f' = f(1 - \beta\cos\theta)$, with f representing the scattering frequency.

3) Change in photon energy and direction for scattering events are significantly greater for head-on photons, and vice versa, as the electron distribution isn't isotropic in the BH rest frame, by:

$$\tan\theta = \frac{u'\sin\theta'}{\gamma(u'\cos\theta' + v)}$$

where γ represents Lorentz factor and θ is the respective electron angle of travel.

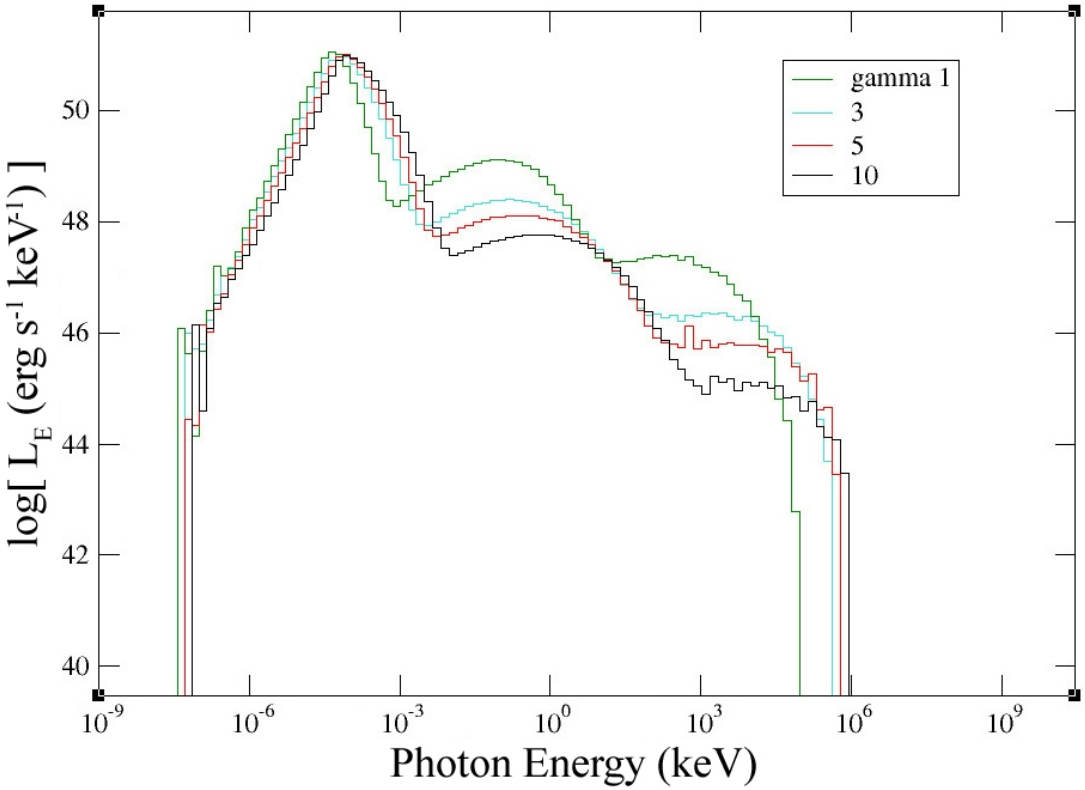

Figure 4.11: A single zone trial to illustrate the effects of the suite of velocity modifications. The general effects of higher Lorentz factor (γ) can be seen in the boosting to higher energies, the loss of scattering frequency, as photons are beamed in the direction of electron travel, and a possible increase in scattered energy.

These effects, taken together, typically result in emissions that are stronger when initially emitted, but have somewhat lower scattering luminosities, as most photons will be beamed in a similar direction to the bulk flow, so will scatter less frequently and with less change in angle. This can be seen in Figure 4.11, which depicts single zone trials.

Chapter 5

Studies of the Applicability and Capability of Shearing Box Simulations for Accretion Disk Particle Energization

This chapter describes and depicts localized shearing box simulations using the Athena MHD code, in the interest of investigating the simulation space between global MHD trials and particle-in-cell simulations, to study particle energization in accretion disks. The 2D HARM code described in Chapters 3 and 4 is extremely powerful for producing models to study global properties, such as spectra and accretion rates. To closely study properties which require resolving smaller scales, the 3D Athena code is ideal. In this case, focus is on determining the capability of an MRI-governed accretion disk to generate collisionless heating of electrons, for eventual application to spectral studies. As models of this sort have not been used for this purpose previously, these initial trials are used to investigate current sheet and turbulence formation, which are likely sources of energization, and determine at what model resolutions these structures can be considered to be converged. With fully 3D models being computationally expensive, attention is also paid to methods of minimizing the computing time necessary to provide meaningful results, as well as measurements of a completed trial. Results suggest that the azimuthal dimension can be compressed significantly to save on processing time, and that power spectra of current and magnetic field components suggest similar levels of saturation due to resolution for the two highest level trials.

5.1 Introduction

To study local phenomena in accretion flows, many, perhaps most, studies use an

approximation termed the "shearing box", first theorized by Hill (1878), and introduced in studies of MHD turbulence and the MRI by Hawley, Gammie, and Balbus (1995). This approximation considers the motions of gas within a box considered to be co-rotating with the disk at some radius r_0. Regev and Umurhan (2008) considered a number of limitations to the shearing box approach, which are mainly that it cannot be used to calculate global disk properties, such as accretion rates or parameter profiles. It is, however, useful to study local gas properties, particularly MHD turbulence (Balbus 2003), and, therefore, current sheet formation and dissipation processes at higher resolutions. In order to maintain the validity of the approximation, the linear extent of the box, L, must be much smaller than r_0.

To modify a current MHD model for the shearing box approximation, specific source terms need to be added to the MHD equations, to simulate the co-rotating frame of the approximation, and a variation of the periodic boundary condition needs to be applied in the radial direction. Athena is a modern 3D MHD code by Stone et al. (2008) based on higher-order Godunov and constrained transport methods. Stone and Gardiner (2010) described the implementation of the Athena-based shearing box approximation, which will be used for this study, as well as the development of an orbital advection algorithm which can speed up co-rotating calculations. This model has been used to study the MRI previously (Davis et al. 2010).

The interest in applying the shearing box approximation to study turbulence and current sheets in this situation is to determine whether it is appropriate to use an MHD shearing box to model parameters for input to particle-in-cell simulations of particle energization. The scales on which energization occurs in model accretion disks is likely

less than about 10^2 cm, based on the gyroradius of particles and the folding length of current sheets. Typical plasma skin depths in LLAGN accretion disks are also on this order, up to about 10^2 cm. In comparison, the full scale of the preceding chapters' MC and GRMHD simulations can be ~ 10^{16} to 10^{20} cm, and even individual cell size can be ~ 10^{10} to 10^{16} cm. Clearly, it is not a given that turbulence parameters for global simulations will extend down to the scales on which energization can occur. Localized simulations, therefore, can be used to span a vast amount of this gap in length scales. The intent here is to use global GRMHD parameters to motivate the input parameters for local shearing box trials, which may provide appropriate parameters to then input into PIC simulations, which have demonstrated that magnetic reconnection and current sheet dissipation can be responsible for energizing particles (Zenitani and Hoshino 2005, 2007; Liang 2009; Liu et al. 2011).

Section 5.2 will briefly describe the shearing box modifications to the MHD equations and the method used in this project. Section 5.3 discusses the results obtained, and Section 5.4 summarizes the conclusions from this study.

5.2 Method

5.1 Shearing Box Math

Athena has been used by a number of studies of MRI turbulence. Soon after the initial introduction of the new code, Gardiner and Stone (2005) tested Athena's algorithms by matching MRI-driven turbulence development to published results. Simon, Hawley, and Beckwith (2009) analyzed the development of MHD turbulence in order to compare Reynolds and Prandtl numbers between runs of differing parameters.

Guan et al. (2009) then studied the locality of MHD turbulence in shearing box simulations, determining that fields in general decorrelate over about a scale height, making turbulence a localized phenomena. Sorathia et al. (2012) interestingly compared results from Athena between localized and global trials and analyzed saturation predictors to demonstrate that in particular circumstances, the larger-scale models could present solutions quantitatively similar to those of local shearing box models. Recently, Lemaster and Stone (2010) published results of a study of energy dissipation and heating by supersonic turbulence.

Converting an MHD model to the shearing box approximation involves fairly simple modifications to the usual MHD equations. In the co-rotating frame, which is assumed to rotate with the disk at an orbital frequency $\Omega_0 = \Omega(r_0)$, the MHD equations are written in Cartesian coordinates (x, y, z) with unit vectors $\hat{i}, \hat{j}, \hat{k}$, which represent the radial, azimuthal, and vertical directions, respectively. The application of the shearing velocity takes the form $\boldsymbol{v_k} = -q\,\omega_0 x\,\hat{\boldsymbol{j}}$, so the velocity is only in the azimuthal direction and varies according to the radius, with the velocity at $r = r_0$ being 0 (with $x = 0$ at $r = r_0$). The shear factor q is defined as:

$$q = \frac{-1}{2}\frac{d \ln \Omega^2}{d \ln r}$$

For Keplerian flow, q = 3/2.

To reflect the shearing nature of the flow, the boundary conditions (BC) are different for the radial faces of the boxes than the others. For the vertical and azimuthal faces, the boundaries have traditional periodic BC's. The shearing periodic BC's for the radial faces are similar, but in effect, allow the "images" of the original simulation box to slide according to the shear velocity at that face.

The remaining changes to the MHD equations involve the inclusion of source terms related to the gravitational force in the rotating frame, and the Coriolis force, as seen in the formats chosen for the compressible, ideal MHD equations:

$$\partial_t \boldsymbol{v} + \boldsymbol{v}\cdot\nabla\boldsymbol{v} = -\frac{1}{\rho}\nabla\left(P + \frac{B^2}{8\pi}\right) + \frac{(\boldsymbol{B}\cdot\nabla)\boldsymbol{B}}{4\pi\rho} - 2\boldsymbol{\Omega}\times\boldsymbol{v} + 2q\Omega^2 x\hat{\boldsymbol{x}} - \Omega^2 z\hat{\boldsymbol{z}}$$

$$\frac{\partial \boldsymbol{B}}{\partial t} = \nabla\times(\boldsymbol{v}\times\boldsymbol{B}) \qquad\qquad \frac{\partial\rho}{\partial t} + \nabla\cdot(\rho\boldsymbol{v}) = 0$$

These are combined with the internal energy equation and equation of state, respectively:

$$\frac{\partial\rho\epsilon}{\partial t} + \nabla\cdot(\rho\epsilon\boldsymbol{v}) + P\nabla\cdot\boldsymbol{v} = 0 \qquad\qquad P = \rho\epsilon(\gamma - 1)$$

Together, these form a set of equations to be solved for the behavior of the plasma within the shearing box. As it is not necessary to fully document this to understand the function of the model, Stone and Gardiner (2010) can be consulted for specific information on how these terms are considered in the simulation.

Athena has been developed to provide very low numerical viscosity, and studies have confirmed this for a number of situations, which are in the range of the resolutions considered here. Furthermore, analysis of data for the variety of resolutions used in this project suggest little difference in the rate of decay of turbulence parameters between different trials, suggesting that numerical dissipation is not unduly affecting runs differently (Stone and Gardiner 2005, 2010; Lemaster and Stone 2009).

5.2.2 Modeling Approach

In order to calculate appropriate parameters for input into the local shearing box simulation, typical output from the GRMHD HARM models discussed in Chapter 4 are considered. The inner radius of the initial torus is ~ 12 M. To avoid gathering data which

may be strongly influenced by the original parameters, the grid is sampled around $r_0 = 10$ M, along the equator. Around this point, averaged values from the HARM run which were used as local uniform shearing box parameters are $\Omega_0 = 2 \times 10^{-3}$, $q = 1.9$, $\beta = 500$, $\rho = 1$, and $P = c_s^2 = 10^{-3}$, where β is the ratio of gas pressure to magnetic pressure, P is pressure, c_s^2 is the square of the sound speed, and ρ is a dimensionless density based on $P = \rho c_s^2$.

To ensure the box contains the fastest growing modes for the development of turbulence, trials were conducted which suggested the box should have side lengths of at least 0.2 scale heights ($H \sim c_s/\Omega$). Box edges were therefore chosen to be $L_x = L_y = L_z = 0.5$ H.

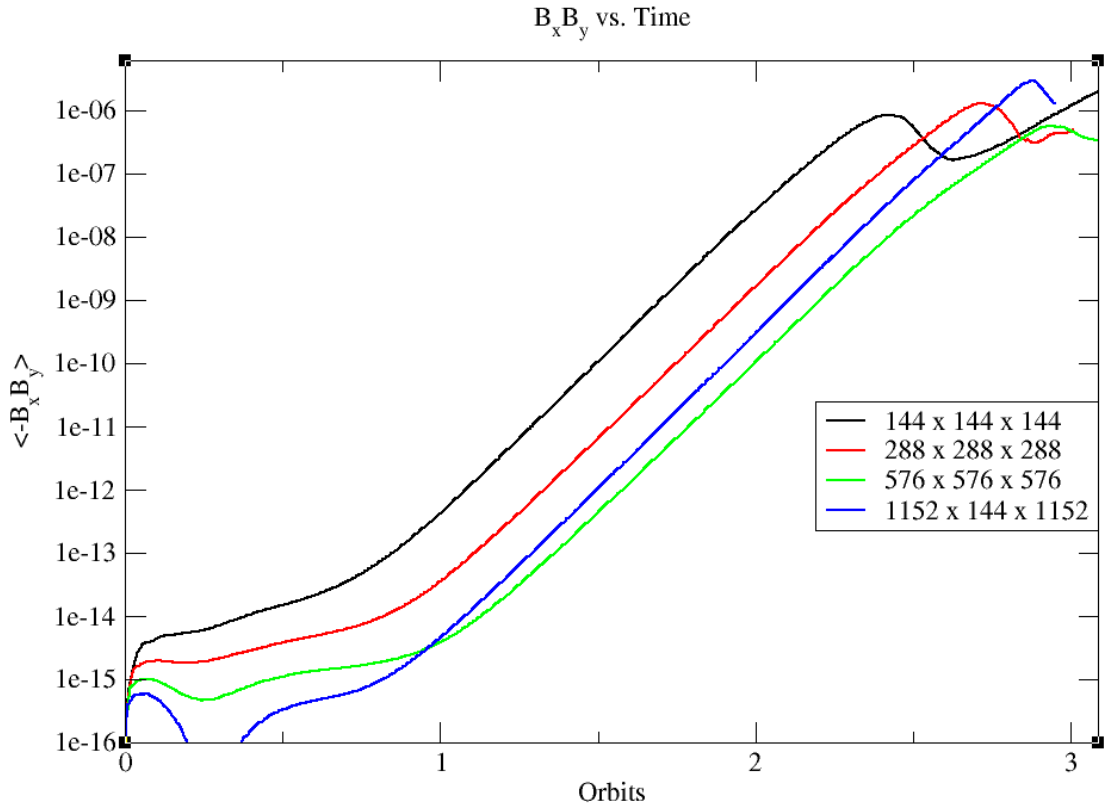

Figure 5.1: Value of $<-B_xB_y>$ plotted against the number of orbits. Of interest is the "saturation" point, which shows the time at which the simulations reach a quasi-steady state. Data is taken following this time, as it marks the point where accretion and angular momentum transport become kinematically important.

Based on these parameters, three trials were conducted initially. The only difference between these was resolution. The resolutions which were considered, assuming a shearing box with cubic dimensions and grid spacing, were 144^3, 288^3, and 576^3 (at the same resolution for each dimension). These values were chosen because the cluster performing the calculations has twelve processors per node, and in order to split the volume into equal blocks for multi-processor calculations, the dimensions had to be multiples of twelve. Trials all started with an initially vertical magnetic field based on plasma $\beta = 500$, and to perturb the plasma to cause the development of turbulence, the density, pressure, and velocity for each cell was randomly varied up to 2.5%. With only these few initial parameters set, runs were begun on 288 processors each.

To evaluate whether trials had evolved to a pseudo-steady state, the average value of B_xB_y was tracked until it saturated. Early in the runs, this value goes through exponential growth, shown in Figure 5.1, as the MRI twists the initially, purely vertical field to develop radial and azimuthal fields. After the saturation point, reached around three orbits, the simulations go through episodes of inflow and outflow, but magnetic field, velocity, and density values only oscillate around some average levels.

Following the three initial trials, results suggested that a higher resolution needed to be considered to determine numerical convergence. As the 576^3 trial had taken a considerable amount of computing time, a trial was conducted to determine the impact of changing the azimuthal dimension without changing the radial and vertical dimensions. Turbulence development was shown to proceed in exactly the same manner, and so a fourth trial with grid dimensions 1152 x 144 x 1152 ($L_x = L_z = 0.5$ H, $L_y = 0.0625$ H). This gave a total number of cells equal to that of the 576^3 trial, but to speed up results,

576 processors were used.

At this point, several methods are considered to attempt to evaluate the convergence of results.

1) Simple images of current magnitude throughout the simulation volume could reveal significant differences between resolutions.

2) Plots of the power spectrum of magnetic field and current should reveal whether changing resolution is having a significant impact on the shape and size of turbulence eddies and current sheet formations.

3) Correlation measurements between the radial and azimuthal velocities and magnetic fields may suggest a trend indicative of convergence. As these are likely to range over a variety of values, plots over time will be necessary to evaluate the likelihood of being a convergence measure.

In the future, wavelet and fractal analyses may be useful to analyze and characterize current sheet structures, which are most relevant for bridging with PIC simulations.

5.3 Results

5.3.1 Current Images

Figure 5.2 shows the square of the current magnitude through the simulation volume for the four resolutions considered, in a slice along the radial-vertical plane. This is depicted on a logarithmic scale, to enhance contrast at lower levels. These images should be evaluated for general changes in shape and size of the specific current sheet formations, rather than the general shape which is largely influenced by transient inflow

and outflow events.

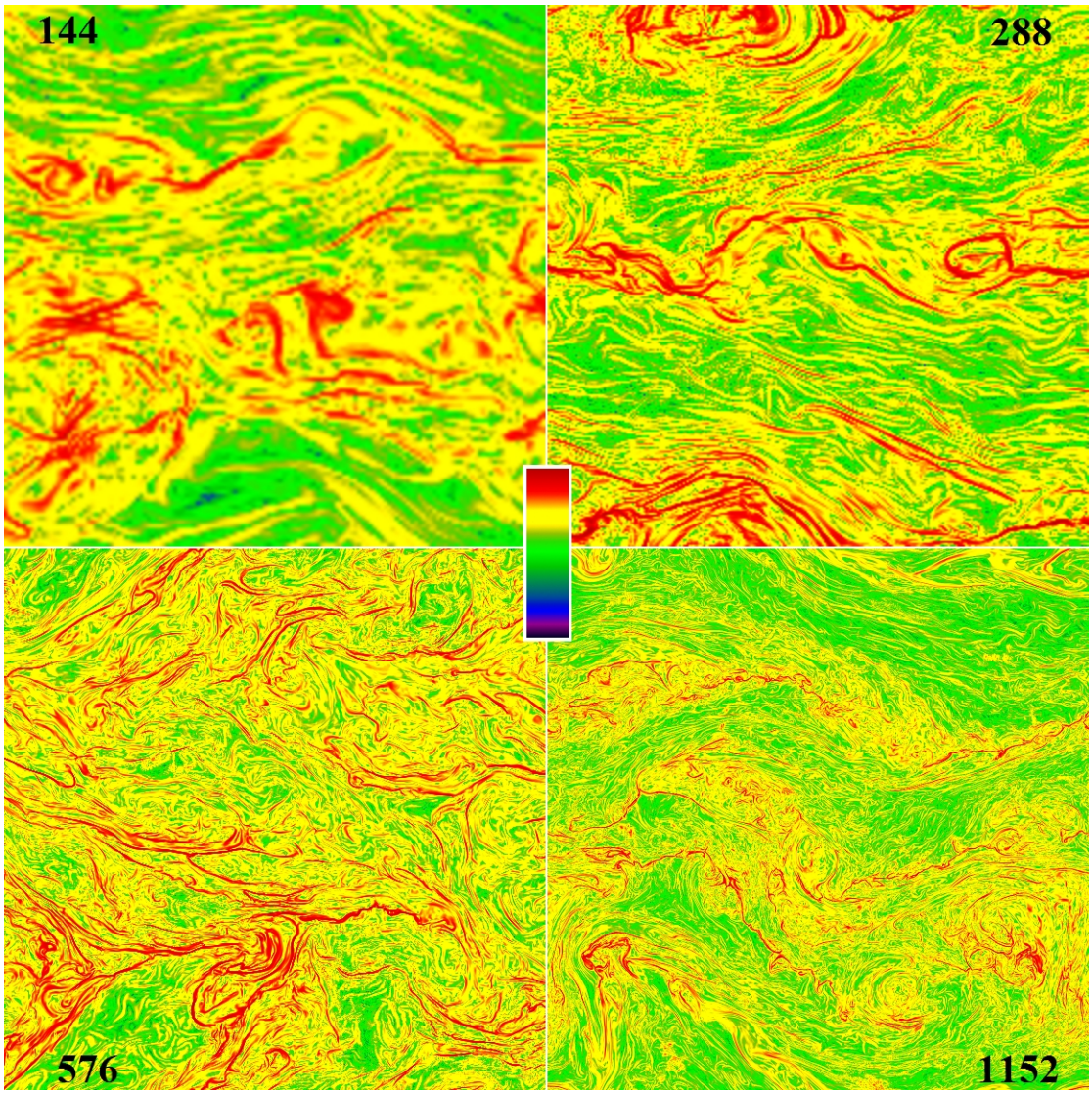

Figure 5.2: Squared current magnitude in radial-vertical plane for all resolutions. Shown on a logarithmic scale based on the color map in the center. This can be used for visual examination of current sheet width and curvature.

The changes from the two lower resolutions to the higher resolution trials are clear, with current sheets becoming much thinner and more concentrated, as well as displaying a larger degree of twisting, suggesting that the inclusion of shorter length grid scales have an important effect on the generation of turbulence and, therefore, current sheets. There are also variations between the two high resolution trials, though they are

not as obvious or, perhaps, significant as those from the lower resolutions. The small-scale structures display better with the 1152 resolution, but seem to generally follow the same trends as the 576 run. The current sheets may be thinner for 1152, but the difference is much less obvious than the previous changes, suggesting that this may be due to transient effects in the trial, or impacted heavily by the scaling values of the images. Higher resolution runs tend to have higher maximum current values, which will cause a seeming "lack" of higher-valued currents, due to the images being scaled to the maximum level for each.

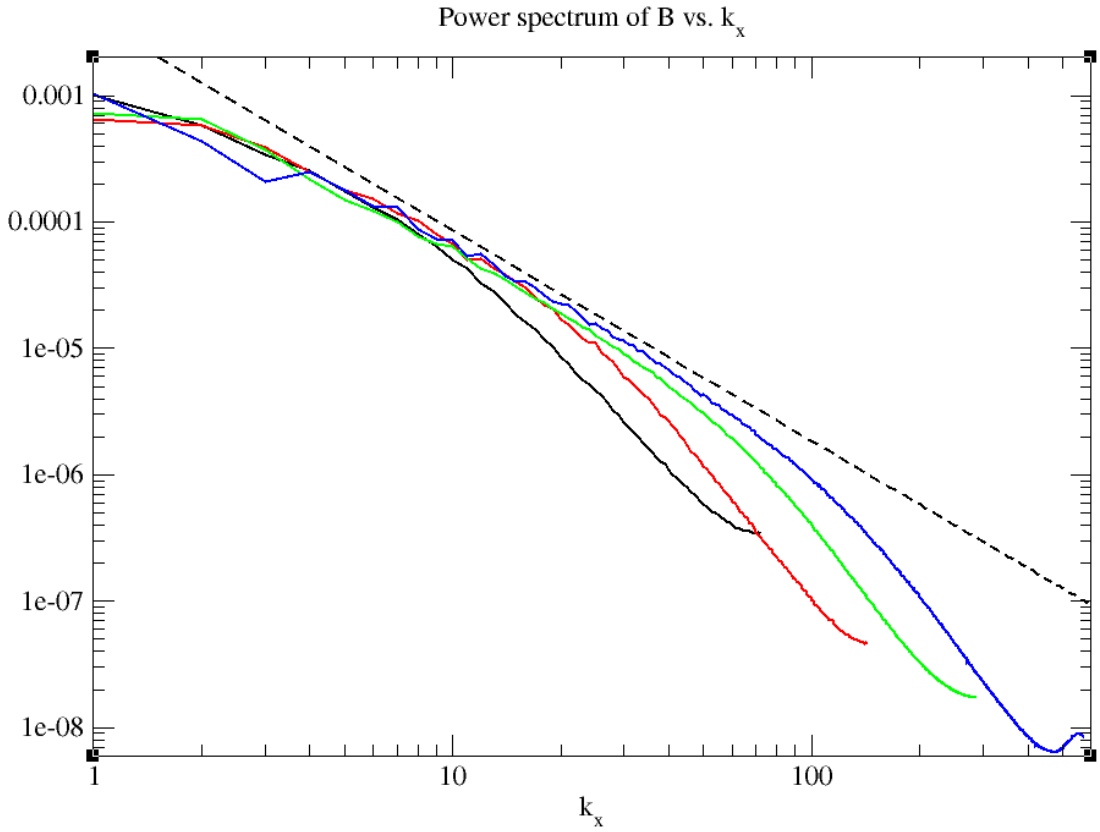

Figure 5.3: Power spectrum of the magnitude of the magnetic field, taken in the radial direction. The four curves are for the four resolution trials, with the curves' extent in k representative of their resolution. The dashed line depicts a power-law with index 5/3, consistent with the Kolmogorov turbulence spectrum.

5.3.2 Power Spectra

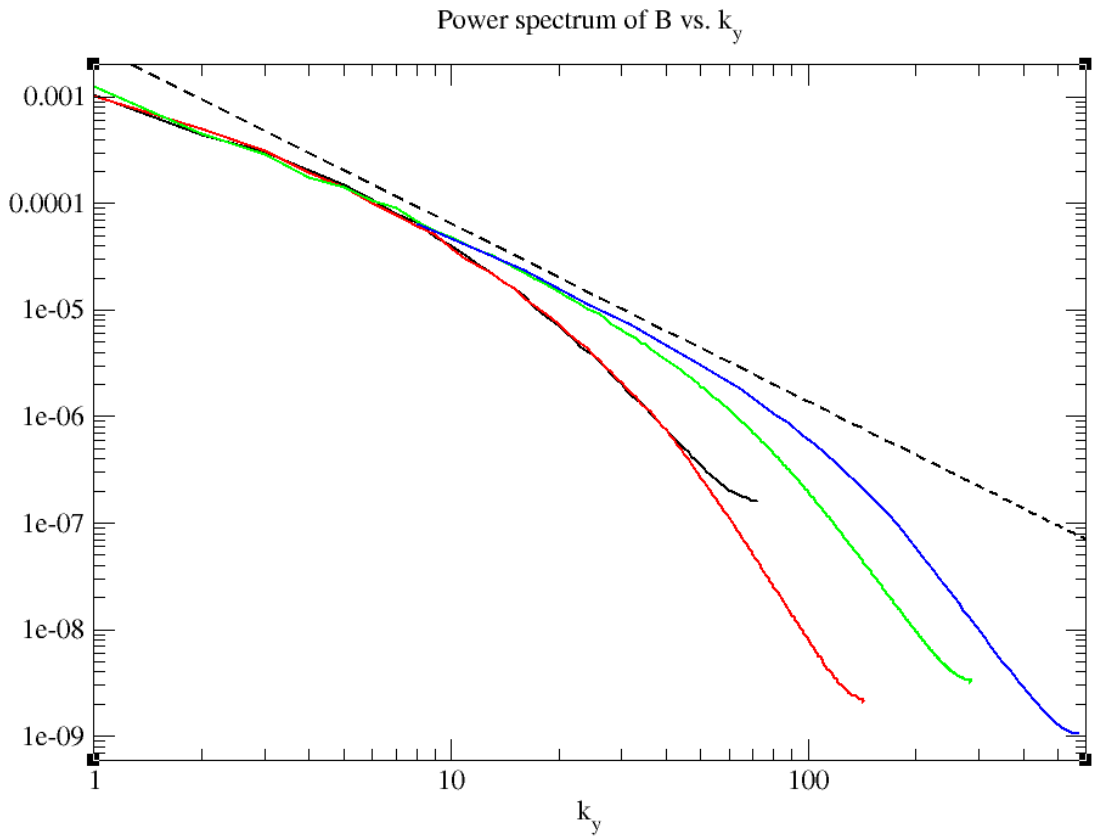

Figure 5.4: As in Figure 5.3, for the azimuthal direction.

The most telling signs of convergence are likely to be seen in the power spectra for the magnetic field and current. Figures 5.3 through 5.8 show these for the magnetic field and current magnitude, in each of the three directions.

The power spectra range from k = 1, a wavelength equal to the box length, to k = 576, a wavelength equal to two radial or vertical cell lengths in the highest resolution trial.

The three magnetic field spectra plots include a line $\propto k^{-5/3}$, a representation of the expected Kolmogorov turbulence spectrum. All four trials show agreement at long wavelengths, but deviate and turnover as their maximum resolutions are approached. Of interest in Figure 5.4 is that the highest resolution trial adheres to turbulence theory

despite the total length in the azimuthal direction being 1/8th that of lower resolution runs.

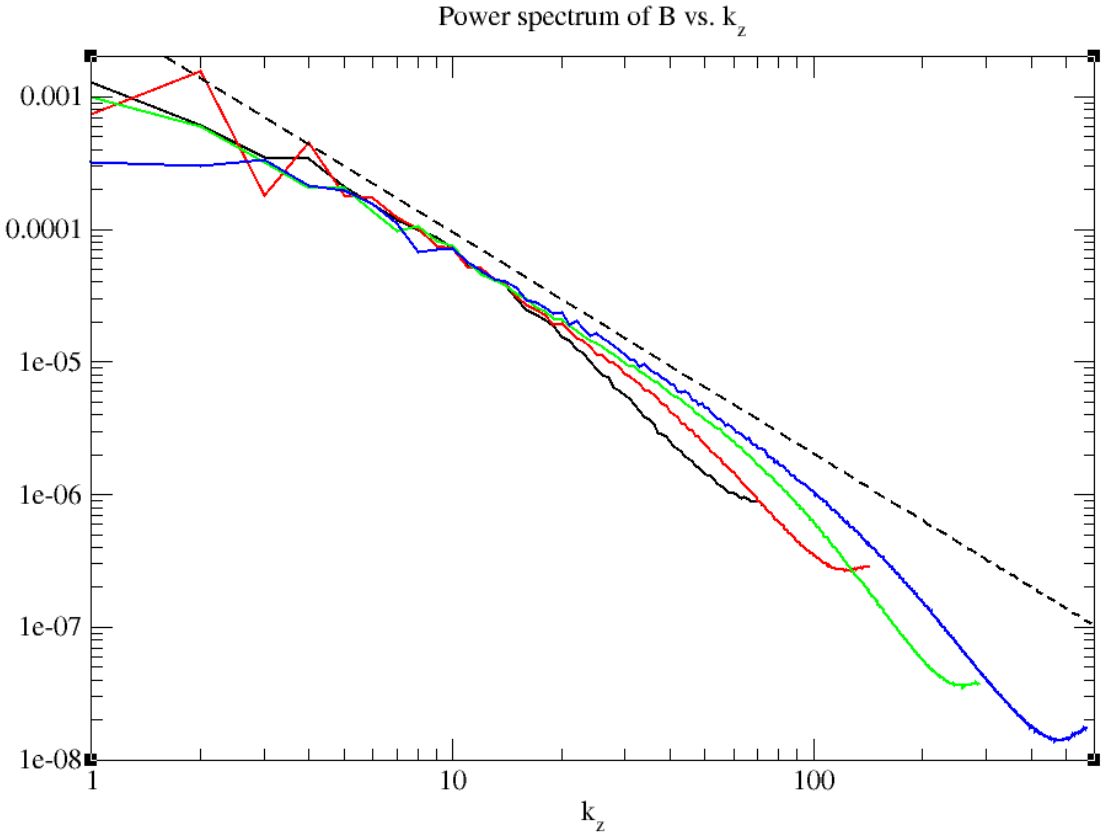

Figure 5.5: As in Figure 5.3, for the vertical direction.

The overall shape of the power spectra for these four trials seems to show that the two highest resolution runs, 576 and 1152, have very similar trends, with turnover shape, spectral index throughout, and general adherence to theory for the majority of the curve. These two, of the four, best show specific indices for the portions of the spectra which may be related to the inertial portion of the curve, the "eddy" region, and then, at high frequencies, a cut-off which could be indicative of the point at which grid-length viscosity becomes important. For this reason, one higher resolution trial, to determine if this is based on overall resolution or may start to converge (that is, that the cut-offs would come together, regardless of resolution) would be helpful.

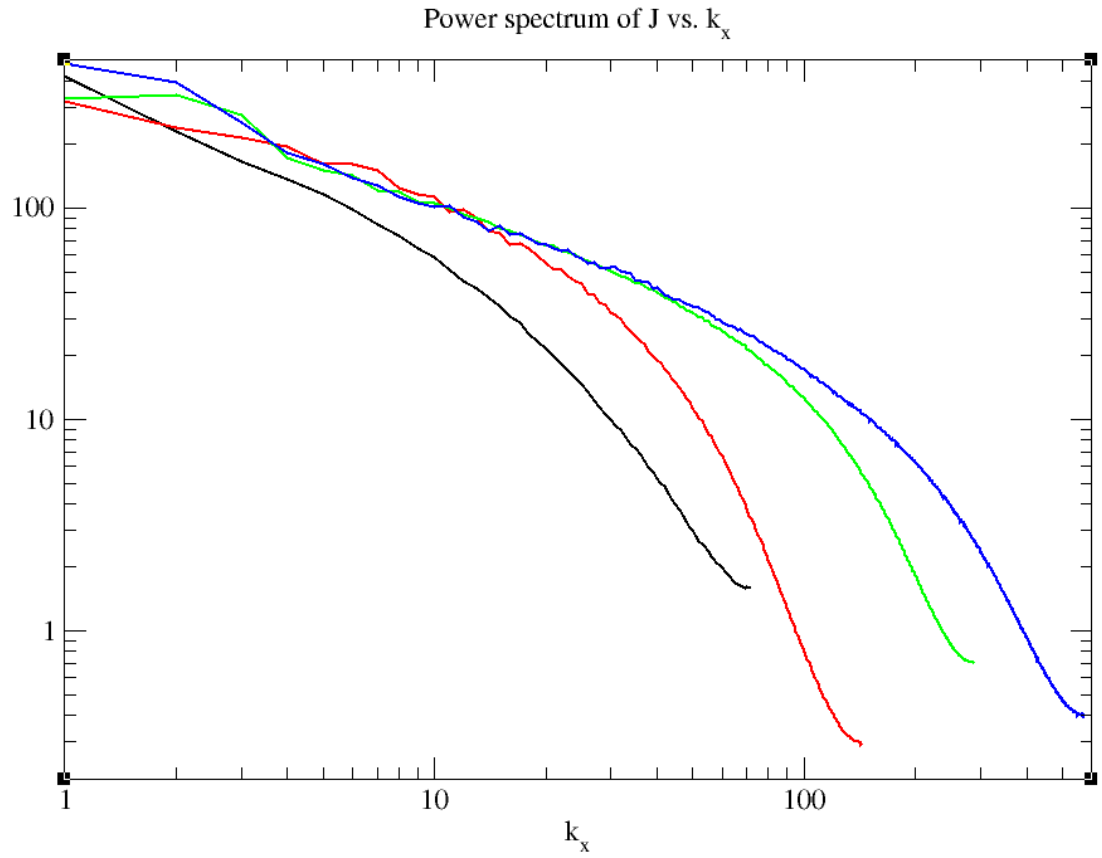

Figure 5.6: Power spectrum of the magnitude of the current, taken in the radial direction.

In general, there is little to obviously separate the lower resolution runs, 144 and 288, from the higher, aside from the clear issue with the 144 run in k_y, where it seems to have too much power at high frequencies to match the trend of the other three.

The power spectra for current show trends similar to those for magnetic field. In Figure 5.6, for k_z, the 144 resolution trial deviates from the others very early. The shape of the cutoffs and indices for the 576 and 1152 runs are very nearly identical.

As with the magnetic field, the 144 run looks most unlikely in the k_y plot. The 288 run is similar in shape to the higher resolutions, but has a more gradual turnover which begins at a very low frequency. 576 and 1152 again show indices and turnover shapes which suggest that 576 is very close in terms of convergence to 1152.

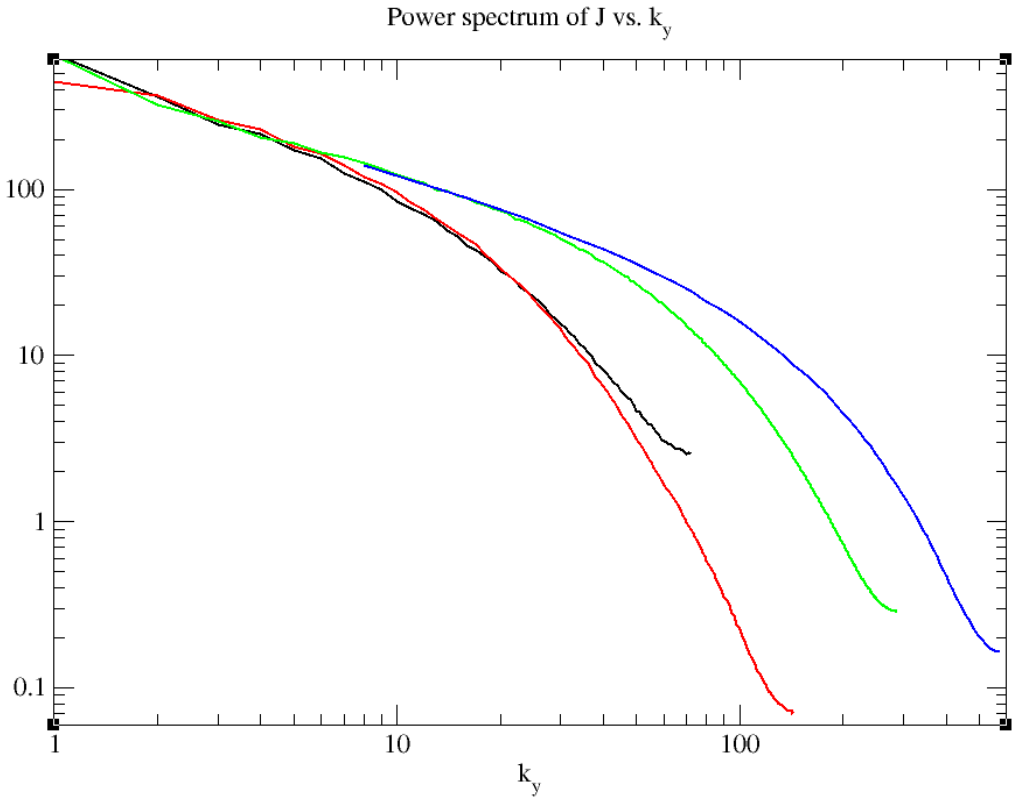

Figure 5.7: As in Figure 5.6, for the azimuthal direction.

All the trials in the k_z current plot look quite similar. The spectral indices in the intermediate region differ somewhat between the two lower and two higher resolution trials. Specifically, the 144 run has a higher index than the 288 run, which similarly has a higher index than the 576 and 1152 runs, which seem to follow each other quite closely. As before, their cutoffs have a very similar shape which somewhat separate them from the lower resolution runs.

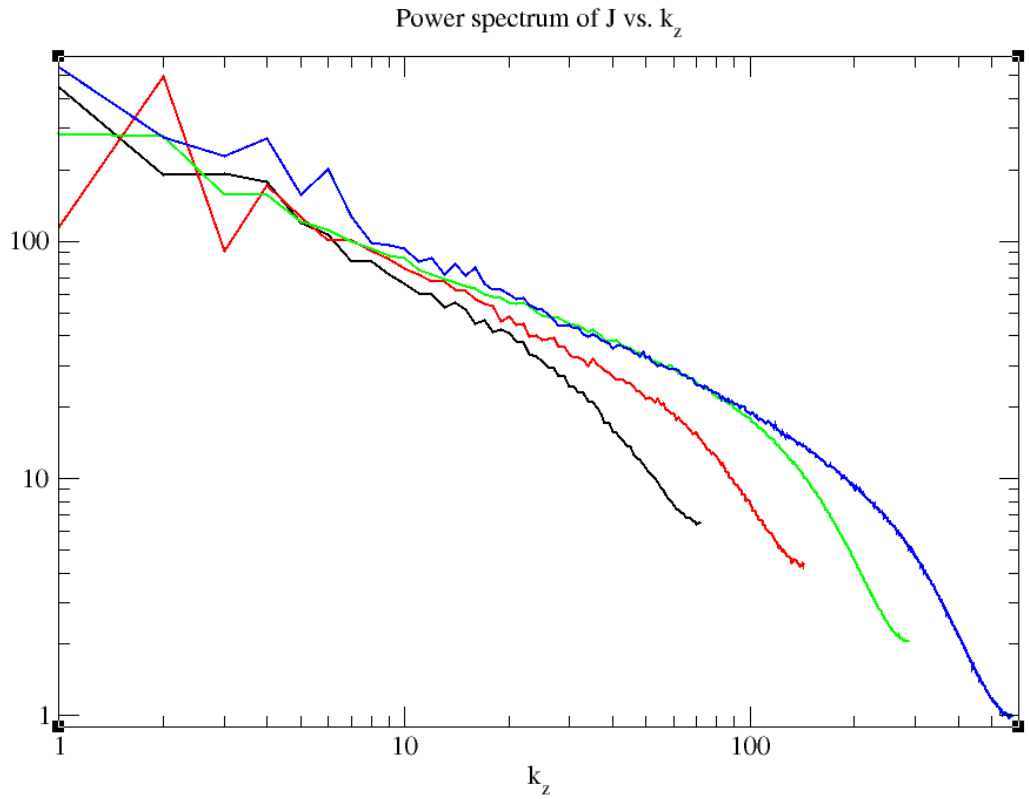

Figure 5.8: As in Figure 5.6, for the vertical direction.

5.3.3 Correlation Coefficients

A correlation coefficient r is evaluated between two parameters x and y based on the formula

$$r_{xy} = \frac{\Sigma(x_i - \bar{x})(y_i - \bar{y})}{\sqrt{\Sigma(x_i - \bar{x})^2 \Sigma(y_i - \bar{y})^2}}$$

where Σ indicates a summation over x and y for all i values, and $\bar{x}$ and $\bar{y}$ are the average x and y values. This coefficient therefore ranges between -1 and 1. Values of -1 or 1 would indicate the two parameters are completely linearly correlated, while a value of 0 indicates they are completely uncorrelated.

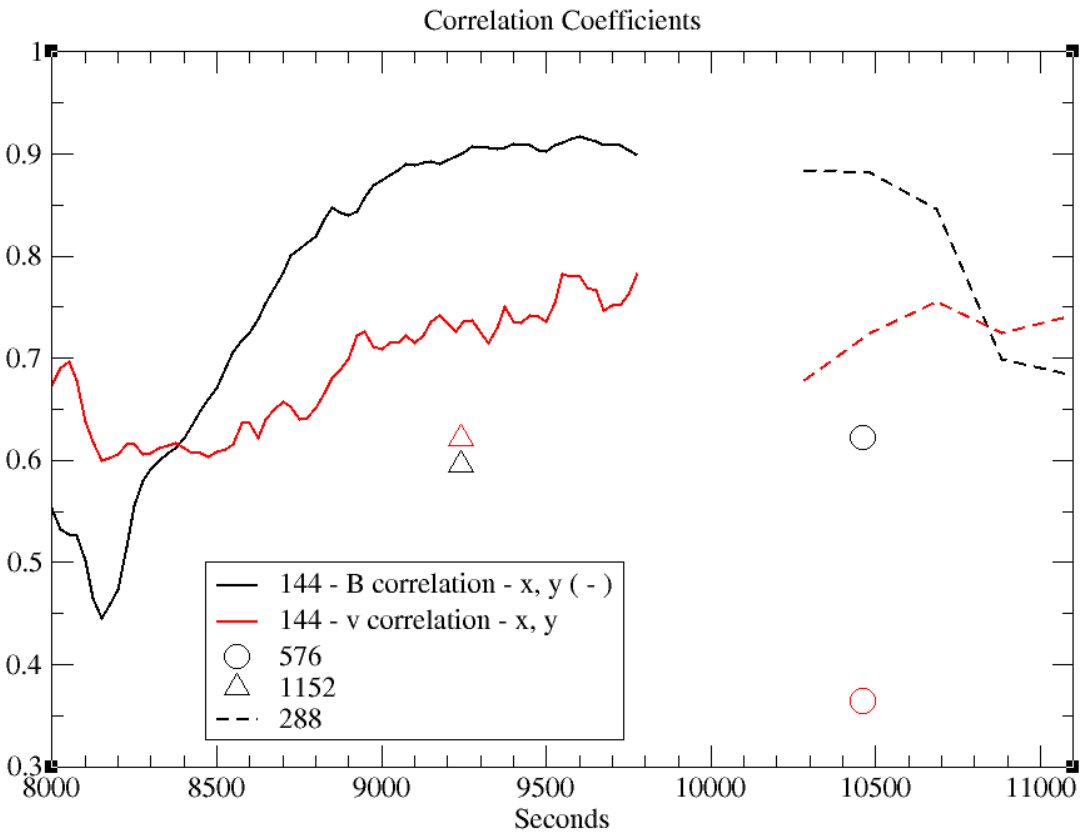

Figure 5.9: Correlation coefficients between B_x and B_y, as well as v_x and v_y, for all four runs. A value of one would indicate that the two components are purely linearly correlated.

Figure 5.9 shows correlation coefficients between Bx and By, and vx and vy, for all four runs. The lower resolution runs have more data due to the time it takes to generate these coefficients for the higher resolutions. These data are all taken during the quasi-steady state for each run, and as the runs reach this point at different times, the lack of contemporaneous data is not an issue. The magnetic field correlations have been multiplied by -1, to enable plotting on the same graph.

In general, the coefficients do not suggest trends to rule out trials regarding convergence or not. It remains to be seen whether variations over time, such as rise/fall time for coefficients may be more telling. A large amount of calculation time must be dedicated to the task of processing the higher resolution trials' data to enable a more full

analysis, particularly due to the v correlation for the 576 run being lower than any other. These data are presented here for completeness, and to allow use by others undertaking similar projects, despite the lack of conclusions which can be drawn.

5.4 Conclusions

The first significant result of the trials presented is the suggestion that runs can be compressed dramatically in the azimuthal direction and still provide extremely pertinent results for analyzing current sheet and magnetic turbulence formation. The trial with resolution 1152 x 144 x 1152, whose length dimensions were then 0.5 H x 0.0625 H x 0.5 H, developed in the same manner as runs whose dimensions were cubic in both resolution and physical dimension.

Analysis of end-of-run outputs generally then suggested that the 576 and 1152 runs were returning extremely similar data. They were separated from the lower resolution runs in a number of ways, which may be a first indication that the 576 run is converged, as far as current sheet and turbulence development is considered. A higher resolution run could help to confirm or disprove this contention.

In current magnitude images, the 576 and 1152 runs were very qualitatively similar, showing development of structures whose curvature and thinness was well-matched between the two trials. Conversely, the lower resolution runs' current structures were dissimilar, being substantially thicker and less contorted than the higher resolutions.

Power spectra of magnetic fields and currents returned generally similar results, with the 576 and 1152 runs consistently showing shapes and spectral indices very close to one another. These higher resolution trials followed a Kolmogorov spectrum closely for

magnetic power spectra, in the intermediate-k regime, while both lower resolution runs tended to diverge early. For both magnetic field and current plots, the 144 trial tended to be significantly different from the other three, while the 288 run was typically closer, but did not show the same similarities in index and turnover shape that the higher resolution runs did to one another. Based on the indices for each segment of the spectra, and the very similar cut-off shapes, the 576 run seems to be close to converged to the results returned by the higher resolution 1152 trial.

Correlation coefficient studies are incomplete and will require more processing time to determine if they will be useful in providing a measure of convergence.

Based on images and power spectra, it seems reasonable to suggest that the 576 run is close to convergence in its development of magnetic turbulence and current sheet formations, as its similarities to the 1152 run vastly outweigh their differences. A higher resolution run, as well as more complete analysis of correlation coefficient data may provide a better indication of this suggestion. The low resolution 144 and 288 trials present data which is quantitatively and qualitatively different in several significant respects to the higher resolution runs, so it seems safe to suggest that they are not at an adequate resolution for convergence in this manner.

Chapter 6

Discussion and Conclusions

The work depicted in this dissertation has been undertaken with the intent of first providing an AGN modeling suite which endeavors to avoid most of the simplifications which create inconsistencies and, therefore, uncertainties in the final results. Modifications to calculations have made for more accurate tools, and analysis of the process has led to a more in-depth study of localized processes and the results important for particle energization.

Chapter 3 details a study of Sgr A* with the HARM GRMHD code coupled with an MC code for radiation transport, as described by Hilburn et al. (2010, 2011). This technique eliminates much of the uncertainty involved with the typical methods of spectral modeling, by ensuring that each step benefits from the most advanced tools available, rather than settling for analytic calculations for either physical or radiative determinations. The goal of this study was to assess the parameter space which allows fits to *Chandra* x-ray data, with various spectral components. The results show that while the flaring x-ray spectrum can be fit by either bremsstrahlung or Compton components, only the fits based on Compton components can then be varied in a single physical parameter to fit the quiescent x-ray spectrum. By far, the best fits were offered by the second Compton bump component. With this spectral component, the variation required to fit the quiescent spectrum was a simple decrease of particle density from the value used for the flaring fit. Therefore, the results suggest that global accretion rate changes (modeled by density changes) are more likely to be responsible for the variation in flux and spectral index observed in x-ray bands than an energization event represented

by a large scale temperature change.

Following this first project, a closer examination of HARM data suggests several shortcomings to the MC code method which oversimplify important nuances and are addressed in the code modifications detailed in Chapter 2. These lay in the consideration of magnetic fields as isotropic, and the bulk plasma as static, though hot. Magnetic fields in GRMHD-modeled accretion disks show very strong biases, usually in the azimuthal or radial directions, which should cause synchrotron emission to be strongly orthogonal to these directions. Similarly, plasma bulk flow tends to be mildly relativistic and largely confined to the equatorial plane. The orbital motion of the plasma as it sheds gravitational energy and transports angular momentum swamps motions in the vertical or radial directions. This leads to emissions being beamed in the direction of motion and boosted upward in energy. Scattering calculations are changed, as photons traveling against the bulk flow will scatter more frequently, and vice versa, and photons undergoing scattering will not do so from an isotropic population.

Chapter 4 presents a study of M87, as detailed by Hilburn and Liang (2012), with similar techniques to those used in Chapter 3, but with the changes described above. Consideration of M87 requires the addition of a separate fitting free parameter, black hole spin, as the spin of M87 is expected to be very high, unlike that of Sgr A*. A library of results was compiled around several spin rates and densities, again with the purpose of fitting flaring and quiescent x-ray spectra, to attempt to comment on likely flaring mechanisms. Results suggest a narrow range of possible particle densities, just below theoretical upper limits based on mass accretion rate. Spin rates are also restricted to $a/M > 0.8$, expectedly high for M87. Parameter variation trials then universally point to

density changes yielding more likely spectral fits than temperature changes, again suggesting that global mass accretion variation is more likely to explain flares than energization events. As the interplay between emissions from M87's disk and jet are of great interest in the community, it is important to point out that this model shows that an entirely accretion-based model (with GRMHD-generated outflows) of the region immediately around the black hole is adequate to describe the core emissions.

The most glaring assumption used within the projects of Chapters 3 and 4 is that of thermalized electrons. This has been invoked due to uncertainties in the energization mechanisms at play in accretion disks, but is likely to be an oversimplification. Moreover, the lack of energization knowledge requires scaling of electron temperature with ion temperature, based on the expectation that their respective heating processes are related to similar physical parameters. Being able to accurately model electron distributions undergoing heating within an accretion disk is clearly the greatest hurdle to more accurate LLAGN modeling. As energization will happen on scales which can be a dozen orders of magnitude smaller than the shortest length scales in global trials, the GRMHD-produced parameters may not translate well to particle-in-cell simulations which actually determine magnetically- and wave-induced heating. Therefore, Chapter 5 discusses a project to generate appropriate PIC input parameters from localized MHD shearing box simulations within a small region of an accretion disk. These models are vastly smaller than global HARM runs and help determine whether global models can be interpolated or interpreted to directly yield PIC input. These recent results suggest that convergence of magnetic field and current sheet geometries has been observed, ensuring that greater resolution is not required.

Extensions to these projects could cover a variety of topics or approaches. Chapter 5 directly sets up the possibility to conduct linked MHD and PIC runs. From these, it would be most interesting to see a library of Fokker-Planck coefficients compiled for various conditions appropriate to LLAGN accretion disks. Taking advantage of the coupled MC-FP code as intended would provide an unrivaled laboratory for investigation of the topics explored here. Even if FP description of accretion disk conditions is too involved a task, it should be possible to analyze the distributions created to suggest whether, for instance, a thermal population with a well-defined high energy non-thermal tail is appropriate.

Very high energy data is readily available for M87, as shown in Chapter 4, and is about as prolific for Sgr A*. Inclusion of the gamma-ray regime in producing model fits could extend the believability of these global types of codes extensively. The electrons producing such high-energy photons at such low fluxes would necessarily be both very hot and very diffuse. A reasonable expectation is that this population could be the aforementioned non-thermal tail to a thermal distribution, so this approach may depend upon the PIC project reaching fruition. A combination of these methods would yield the most powerful tool available for calculating radiation transport in LLAGN disks.

The projects undertaken in this dissertation fulfill their goals of advancing knowledge of both global and local properties of accretion disks in LLAGN. Possible flaring mechanisms were investigated for Sgr A* and M87, and data from both sources yielded results strongly suggestive of accretion rate variation to produce observed spectral transients. The project for M87 successfully demonstrated that an external jet model is not necessary to fit data well and describe variability. The fledgling shearing

box project has been successfully created as a resource to further modeling pursuits, particularly those involving PIC simulations investigating accretion disk particle energization. Beyond simply generating adequate fits to data, these projects have advanced the community's understanding of the capabilities of modeling, have delivered code which will continue to be of use for more consistent simulations of a variety of astrophysical sources, and have increased knowledge of physical processes in LLAGN.

Appendix

Monte Carlo Code User's Manual - Sample Input Files, User-changeable Settings, and Code Use

This appendix is being constructed to allow a user to be up and running with the MC code as quickly as possible. Section A.1 details the basic input files which the code reads at the beginning of each run, and Section A.2 discusses more of the in-depth settings, whose modification requires a code re-compile. The actual process of compiling and running the code is discussed in Section A.3.

A.1 Sample Input Files

The main input file read by the MC code is titled 'input.dat'. A sample file is shown below, with some changes to format to fit the page.

```
NUMBER OF Z BOUNDARIES                                  nz = 4
NUMBER OF R BOUNDARIES                                  nr = 4
Upper z boundary [cm]                       z(nz) = 4.9620e+16
Lower r boundary [cm]                        rmin = 0.0000e+00
Upper r boundary [cm]                       r(nr) = 2.4810e+16
Let upper surface source be a star?
          (1=star, 0=no star)                  star_switch = 0
Time to stop simulation [s]:                     tstop = 2.e10
Maximum time step [s]:                           dtmax = 1.d8
Number of time steps for boundary
          temperature inputs:                       ntime = 1
Beginning of time step 1 [s]:                     t0(1) = 0.d0
End of time step 1 [s]:                           t1(1) = 1.d0
Boundary temp. of the upper boundary,
          radial zone  1, time 1:              tbbu( 1,1) = 0.
Boundary temp. of the lower boundary,
          radial zone  1, time 1:              tbbl( 1,1) = 0.
Boundary temp. of the upper boundary,
          radial zone  2, time 1:              tbbu( 2,1) = 0.
Boundary temp. of the lower boundary,
          radial zone  2, time 1:              tbbl( 2,1) = 0.
```

```
Boundary temp. of the upper boundary,
          radial zone  3, time 1:           tbbu( 3,1) = 0.
Boundary temp. of the lower boundary,
          radial zone  3, time 1:           tbbl( 3,1) = 0.
Boundary temp. of the upper boundary,
          radial zone  4, time 1:           tbbu( 4,1) = 0.
Boundary temp. of the lower boundary,
          radial zone  4, time 1:           tbbl( 4,1) = 0.
BOUNDARY TEMPERATURE OF THE OUTER BOUNDARY
          vert zone  1, time 1:             tbbo( 1,1) = 0.
BOUNDARY TEMPERATURE OF THE INNER BOUNDARY
          vert zone  1, time 1:             tbbi( 1,1) = 0.
BOUNDARY TEMPERATURE OF THE OUTER BOUNDARY
          vert zone  2, time 1:             tbbo( 2,1) = 0.
BOUNDARY TEMPERATURE OF THE INNER BOUNDARY
          vert zone  2, time 1:             tbbi( 2,1) = 0.
BOUNDARY TEMPERATURE OF THE OUTER BOUNDARY
          vert zone  3, time 1:             tbbo( 3,1) = 0.
BOUNDARY TEMPERATURE OF THE INNER BOUNDARY
          vert zone  3, time 1:             tbbi( 3,1) = 0.
BOUNDARY TEMPERATURE OF THE OUTER BOUNDARY
          vert zone  4, time 1:             tbbo( 4,1) = 0.
BOUNDARY TEMPERATURE OF THE INNER BOUNDARY
          vert zone  4, time 1:             tbbi( 4,1) = 0.
Spectra incident on upper and lower
          boundaries? (0=no,1=yes)          spec_switch = 0
Number of photon regions                         nphreg = 3
Minimum Energy of the photon in region 1
                                           Ephmin(1) = 1.d-9
Maximum Energy of the photon in region 1
                                           Ephmax(1) = 1.d-3
Number of photon energy bins in region 1
                                            nphbins(1) = 42
Minimum Energy of the photon in region 2
                                           Ephmin(2) = 1.d-3
Maximum Energy of the photon in region 2
                                            Ephmax(2) = 1.d2
Number of photon energy bins in region 2
                                            nphbins(2) = 43
Minimum Energy of the photon in region 3
                                            Ephmin(3) = 1.d2
Maximum Energy of the photon in region 3
                                           Ephmax(3) = 1.d11
Number of photon energy bins in region 3
                                             nphbins(3) = 43
Observation angle (number of mu-bins)                nmu = 1
Number of energy bins in for light curves        nph_lc = 5
```

```
Lower boundary of Light Curve Energy Bin
                                                Elcmin(1) = 0.1
Upper boundary of the Light Curve Energy Bin
                                               Elcmax(1) = 1.d0
Lower boundary of Light Curve Energy Bin
                                               Elcmin(2) = 1.d0
Upper boundary of the Light Curve Energy Bin
                                               Elcmax(2) = 3.d0
Lower boundary of Light Curve Energy Bin
                                               Elcmin(3) = 3.d0
Upper boundary of the Light Curve Energy Bin
                                               Elcmax(3) = 1.d1
Lower boundary of Light Curve Energy Bin
                                               Elcmin(4) = 1.d1
Upper boundary of the Light Curve Energy Bin
                                               Elcmax(4) = 5.d1
Lower boundary of Light Curve Energy Bin
                                               Elcmin(5) = 5.d1
Upper boundary of the Light Curve Energy Bin
                                               Elcmax(5) = 5.d2
File name for time-integrated
          energy spectra:    spname = output/sp_harm_01.dat
File name for time-integrated
          photon spectra:    phname = output/ph_harm_01.dat
File name for light curves in angular
          bin no. 1:      lcname(1) = output/lc_harm_01.dat
File name for census file 1:         census(1) = census1.dat
File name for census file 2:         census(2) = census2.dat
File name for event file:         eventfile = ev_harm_01.dat
File name for electron temperature
          history:      temp_file = output/temp_harm_01.dat
Particle number per photon cycle:              nst = 10000000
Number of initial calls to random
          number generator                      rseed = 10000
Type of rand. number gen. (1 = lag. fib.,
          2 = lin. cong.)                    rand_switch = 2
Compton refl. sentinel (0 = none, 1 = lower,
          2 = outer, 3 = both)                   cr_sent = 0
Upper Boundary Reflection Sentinel (0 = none,
          1 = refl. )                          upper_sent = 0
Disk heating on (1) / off (0)                dh_sentinel = 0
Pair processes on (1) / off (0)              pair_switch = 0
Constant temperature (electron spectrum)
          switch on (1) / off (0)                T_const = 1
Coronal heating flare on (1) / off (0)       cf_sentinel = 0
Center of coronal heating flare,
          radius [cm]:                          r_flare = 0.d0
```

```
Center of coronal heating flare,
          height [cm]:                          z_flare = 0.d0
Center of coronal heating flare,
          time [s]:                             t_flare = 0.d0
Radial width of flaring region [cm]:          sigma_r = 0.d0
Vertical width of flaring region [cm]:        sigma_z = 0.d0
Time width of flaring region [s]:             sigma_t = 0.d0
Flare amplitude: (delta B / B_0)^2_max;
          (delta T_p)/T_p:                  flare_amp = 0.d0
```

Starting at the top, `nz` and `nr` represent the total number of cells in each direction. For the runs described in this dissertation, these values were both set to 95, to allow for maximum resolution of the simulation volume. The code has a soft cap on the grid resolution, though it is a trivial matter to redefine this. It was determined throughout these trials that the results converged at grid sizes around 50x50, suggesting that there is little need to extend these parameters further for these types of studies.

The next three parameters, `z(nz)`, `rmin`, and `r(nr)` describe the total volume size, in cm. The minimum r value is shown to be 0, but this can be changed to reflect a hollow cylindrical, or ring-shaped volume. If `star_switch` is set to 1, the upper boundary source photons, rather than being randomly distributed over 2π steradians, will be parallel to one another.

The time parameters set the ending time for the simulation (`tstop`) and maximum time step (`dtmax`), both in seconds. The next values may be used to set a number of time regions, where surface sources may change their properties. One is specified initially, though there are no surface sources set. Continuing in a similar process can set multiple time regions. The next block of code sets boundary temperatures, with `tbbu`, etc., if the desired boundary source is a Planck spectrum. To use specific spectra from files, these temperatures should be set to less than 0, and then

the input file must be specified.

The `spec_switch` parameter may be turned on (to 1) so that the output spectra will be calculated based on photons incident on the upper and lower boundaries, rather than all photons which leave the simulation volume. To specify how many energy binning regions are considered for the photons, `nphreg` can be adjusted. The next lines then specify the energy range for each bin (`Ephmin` and `Ephmax`) in keV and the number of bins within that region, `nphbins`, with the total number of bins equal to or less than 128. These bins are spaced evenly in logarithmic space. To setup numerous angular bins for photons, `nmu` can be set greater than 1. Spectra will then be separated equally in angular space by the cosine of the inclination angle, to allow for differences in viewing angle. Similarly, multiple light curve bins can be set by `nph_lc`, which is followed by definitions of each bin, by `Elcmin` and `Elcmax`. which are specified in keV.

Names of the output files are specified next, including photon spectrum, energy spectrum, light curves, and census files which, if enabled, are used to keep track of photon information between time steps. The temperature file records a thermally-fit temperature for the zones at each time step, and the event file records all pertinent information (energy, time, location, and angle of emission) for escaped photons.

The total number of MC photons in the volume at any given time is set by `nst`. Random number properties are included in `rseed`, which will change the initial number of calls to the random number generator, and `rand_switch`, which sets the type of random number generator used by the code. In general, the linear congruent generator of Press et al. (2001) is much faster, without having a significant statistical disadvantage to

the lagged Fibonacci generator from Knuth (1997). More specific details on the generators can be found in Finke (2007).

The final block of input contains settings for specific problems. The Compton reflection sentinel, `cr_sent`, can be set to 1 for lower boundary, 2 for outer boundary, 3 for both, or 4 for the inner disk, which makes those surfaces purely Compton reflecting. To set the lower boundary to be heated by reflection, `dh_sentinel` can be turned on. Pair annihilation and creation can be turned on by `pair_switch`. If `T_const` is turned off, the FP process will be allowed to evolve the electron distributions. The last few lines then detail, first, whether there is a flaring region within the volume, and then set its location, size, time, and amplitude.

After reading in the main input file, *reader* looks for separate files for each zone in the grid. The first of these would be titled 'input_01_01.dat'. with each subsequent vertical row of zones incrementing the first number, and radial column the same for the second. For instance, the second vertical and fourth radial zone would have a file named 'input_02_04.dat'. A sample zone input file is shown below, for the most recent edition of the MC code.

```
1. Electron temperature in zone [keV]      tea = 4.88238e+02
2. Proton temperature in zone [keV]        tna = 4.88238e+02
3. Particle density in zone [cm^(-3)]      n_e = 9.80350e+01
4. Magn. field sent. (0 = spec.,
          1 = ep. w. el., 2 = ep. w. pr.)     ep_switch = 0
5a. Magnetic field [G]                     B_r = -2.11960e+01
5b.                                        B_z = -1.98549e+01
5c.                                      B_phi = -1.95332e+01
6.a Cell's Z Lorentz factor          z_cell_vel = 1.18324e+00
6.b Velocity rho (radial) component
          (positive outward)          rho_unit = 2.47987e-02
6.c Velocity phi component             phi_unit = 9.97190e-01
6.d Velocity z component                 z_unit = 7.06895e-02
7. Maxwellian fraction in zone           amxwl = 1.000000e+00
```

```
8. Low-energy cut-off of nonthermal
          electron population:           gmin = 1.00000e+01
9. High-energy cut-off of nonthermal
          electron population:           gmax = 1.00000e+02
10. Non-thermal electron
          spectral index:              p_nth = 2.00000e+00
11. Turbulence sp.index           q_turb(j,k) = 1.666667e+00
12. Turbulence Level
          (deltaB/B0)^2        turb_lev (j,k) = 1.000000e-20
```

The first two lines specify electron and proton temperature for this zone, with `tea` and `tna`, respectively, in keV, and `n_e` sets the particle number density, in particles per cubic centimeter. The next setting, `ep_switch`, determines whether the magnetic field magnitude is set by equipartition with electrons (1) or protons (2), which suggests that magnetic energy density is equivalent to particle thermal energy density, or simply specified by this input file (0). If this parameter is set to 0, the next 3 lines define the magnetic field radial, vertical, and azimuthal components in Gauss. Parameter 6 specifies the bulk flow Lorentz factor (`z_cell_vel`), and the three components of a unit vector describing the direction of bulk flow (`rho_unit`, `phi_unit`, and `z_unit`). The next three lines explain the non-thermal portion of the electron distribution, by setting the Maxwellian fraction (`amxwl`), high- and low-energy cut-offs (`gmin` and `gmax`) in units of γ, and the non-thermal power-law spectral index (`p_nth`). The final two parameters set the spectral index of magnetic turbulence (q_turb), which would usually be 5/3, for a Kolmogorov turbulence spectrum, and the level of turbulence (turb_lev) in units of $(\delta B/B_0)^2$. If the FP routine is turned on, the electron temperature, magnetic field (if set to be in equipartition with electron temperature), and Maxwellian fraction may all evolve with time.

All of the input files are handled by reader.f, so please see this file for more

specificity regarding some of the components which are not covered in detail. It is laid out in a fairly self-explanatory manner.

A.2 User-adjustable Settings within the Monte Carlo Code

There are a number of parameters and settings which pop up at various points within the code, which may be useful to adjust for consideration of certain problems. Some of the major global parameters include `num_nt`, which is the number of bins in the electron energy grid, `n_vol`, which is the number of bins in the photon energy grid, and `nphfield`, which is the number of bins in the Compton loss calculation grid. Another useful option is to change the emission energy range, at lines 65 and 115 in volume2d.f. Line 115 sets the beginning of the range of energy (in keV) considered by the volume emission routine, while line 65 sets the total range by the only value in the calculation for dE. For the trials shown in this dissertation, the emission range is from 10^{-8} to 10^{7} keV.

A.3 Running the Monte Carlo Code

Compiling and running the MC code is a very straightforward process, if a user has experience with MPI programs. On a system with an appropriate MPI Fortran compiler installed, the Makefile will automatically compile all of the necessary code files when called with the 'make' command. This generates an executable named compton2d. Depending on your MPI environment, the code can then be run using the 'mpiexec' or 'mpirun' commands. In order to run properly, the code will need to be in a folder with its input files contained in a folder named 'Input', an 'Output' folder, if

The job scheduling system in place on Rice's clusters uses PBS job scripts to set

up jobs. An example script to run a job is shown below.

```
#PBS -q compute
#PBS -l nodes=4:ppn=8,walltime=08:00:00
#PBS -M user@rice.edu
#PBS -m bae
#PBS -o /shared.scratch/user1/c2d
#PBS -e /shared.scratch/user1/c2d
#PBS -V
echo 'My job ran on:'
cat $PBS_NODEFILE
cd /shared.scratch/user1/c2d
mpiexec ./compton2d > /shared.scratch/user1/c2d/cmptrun.log
```

In the above example, the first line specifies the queue on the cluster to apply for time in. The next line tells the scheduler how many nodes, with how many processors per node, for how much time, this job is requesting. The next two lines specify an email address to send job status to, and to notify the user when the job begins, aborts, or exits. The following two lines specify the paths for the standard output and standard error files. The -V setting exports all environment variables to the job. Then the 'echo' and 'cat' lines send that sentence and the pertinent node information to the job's output file. The final two lines then navigate to the appropriate directory, where the executable is, and call for it to run with 'mpiexec', also specifying a log file within that same directory.

For further information on using Rice's clusters, visit http://rcsg.rice.edu .

Bibliography

A. A. Abdo et al. Fermi Large Area Telescope Gamma-Ray Detection of the Radio Galaxy M87. *ApJ*, 707:55-60, November 2009.

M. A. Abramowicz, X. Chen, S. Kato, J.-P. Lasota, O. Regev. Thermal equilibria of accretion disks. *ApJ*, 438:L37-L39, January 1995.

V. A. Acciari et al. Observation of Gamma-Ray Emission from the Galaxy M87 above 250 GeV with VERITAS. *ApJ*, 679:397-403, May 2008.

V. A. Acciari et al. Veritas 2008-2009 Monitoring of the Variable Gamma-ray Source M 87. *ApJ*, 716:819-824, June 2010.

F. Aharonian et al. Is the giant radio galaxy M 87 a TeV gamma-ray emitter? *A&A*, 403:L1-L5, May 2003.

F. Aharonian et al. Observations of 54 Active Galactic Nuclei with the HEGRA system of Cherenkov telescopes. *A&A*, 421:529-537, July 2004.

F. Aharonian et al. Fast Variability of Tera-Electron Volt γ Rays from the Radio Galaxy M87. *Science*, 314:1424-1427, December 2006.

M. Ajello, A. Rau, J. Greiner, G. Kanbach, M. Salvato, A. W. Strong, S. D. Barthelmy, N. Gehrels, C. B. Markwardt, and J. Tueller. The Swift BAT X-Ray Survey. III. X-Ray Spectra and Statistical Properties. *ApJ*, 673:96-113, January 2008.

M. Ajello, L. Costamante, R. M. Sambruna, N. Gehrels, J. Chiang, A. Rau, A. Escala, J. Greiner, J. Tueller, J. V. Wall, and R. F. Mushotzky. The Evolution of Swift/BAT Blazars and the Origin of the MeV Background. *ApJ*, 699:603-625, July 2009.

R. R. Antonucci and J. S. Miller. Spectropolarimetry and the nature of NGC 1068. *ApJ*, 297:621-632, October 1985.

W. Baade and R. Minkowski. Identification of the Radio Sources in Cassiopeia, Cygnus a, and Puppis a. *ApJ*, 119:206-214, January 1954.

D. C. Backer and R. A. Sramek. Apparent proper motions of the galactic center compact radio source and PSR 1929+10. *ApJ*, 260:512-519, September 1982.

F. K. Baganoff, M. W. Bautz, W. N. Brandt, G. Chartas, E. D. Feigelson, G. P. Garmire, Y. Maeda, M. Morris, G. R. Ricker, L. K. Townsley, and F. Walter. Rapid X-ray flaring from the direction of the supermassive black hole at the Galactic Centre. *Nature*, 413:45-48, September 2001.

F. K. Baganoff, Y. Maeda, M. Morris, M. W. Bautz, W. N. Brandt, W. Cui, J. P. Doty, E. D. Feigelson, G. P. Garmire, S. H. Pravdo, G. R. Ricker, and L. K. Townsley. Chandra X-Ray Spectroscopic Imaging of Sagittarius A* and the Central Parsec of the Galaxy. *ApJ*, 591:891-915, July 2003.

S. A. Balbus. Enhanced Angular Momentum Transport in Accretion Disks. *ARA&A*, 41:555-597, January 2003.

S. A. Balbus and J. F. Hawley. A powerful local shear instability in weakly magnetized disks. I - Linear analysis. II - Nonlinear evolution. *ApJ*, 376:214-233, July 1991.

B. Balick and R. L. Brown. Intense sub-arcsecond structure in the galactic center. *ApJ*, 194:265-270, December 1974.

G. Bélanger, A. Goldwurm, F. Melia, P. Ferrando, N. Grosso, D. Porquet, R. Warwick, and F. Yusef-Zadeh. Repeated X-Ray Flaring Activity in Sagittarius A*. *ApJ*, 635:1095-1102, December 2005.

J. A. Biretta, W. B. Sparks, and F. Macchetto. Hubble Space Telescope Observations of Superluminal Motion in the M87 Jet. *ApJ*, 520:621-626, August 1999.

J. A. Biretta, C. P. Stern, and D. E. Harris. The radio to X-ray spectrum of the M87 jet and nucleus. *AJ*, 101:1632-1646, May 1991.

R. D. Blandford and M. J. Rees. Some comments on radiation mechanisms in Lacertids. *Pittsburgh Conference on BL Lac Objects*, ed. A. M. Wolfe. Pittsburgh, Pennsylvania, University of Pennsylvania, p. 328-341, April 1978.

J. G. Bolton. Discrete Sources of Galactic Radio Frequency Noise. *Nature*, 162:141-142, July 1948.

J. G. Bolton, G. J. Stanley, and O. B. Slee. Positions of Three Discrete Sources of Galactic Radio-Frequency Radiation. *Nature*, 164:101-102, July 1949.

M. Böttcher. Coronal Cooling and Its Signatures in the Rapid Aperiodic Variability of Galactic Black Hole Candidates. *ApJ*, 553:960-967, June 2001.

M. Böttcher, D. R. Jackson, and E. P. Liang. Two-dimensional Monte Carlo/Fokker-Planck Simulations of Flares in Accretion Disk Corona Models. *ApJ*, 586:389-402, March 2003.

M. Böttcher and E. P. Liang. Comptonization Signatures in the Rapid Aperiodic Variability of Galactic Black Hole Candidates. *ApJ*, 506:281-288, October 1998.

M. Böttcher and E. P. Liang. A New Model for the Hard Time Lags in Black Hole X-Ray Binaries. *ApJ*, 511:L37-L40, January 1999.

M. Böttcher and E. P. Liang. Monte Carlo Simulations of Thermal-Nonthermal Radiation from a Neutron Star Magnetospheric Accretion Shell. *ApJ*, 552:248-258, May 2001.

M. Böttcher, E. P. Liang, and I. A. Smith. Radiation feedback in hot accretion-disk corona models and application to GX 339-4. *A&A*, 339:87-94, November 1998.

C. S. Bowyer, M. Lampton, J. Mack, and F. de Mendonca. Detection of X-Ray Emission from 3C 273 and NGC 5128. *A&AA*, 161:L1, July 1970.

G. R. Burbidge. The theoretical explanation of radio emission. *Paris Symposium on Radio Astronomy*, ed. R. N. Bracewell. Stanford, California: Stanford University Press, p. 541, 1959.

E. Canfield, W. M. Howard, and E. P. Liang. Inverse Comptonization by one-dimensional relativistic electrons. *ApJ*, 323:565-574, December 1987.

S. Chandrasekhar. The Stability of Non-Dissipative Couette Flow in Hydromagnetics. *PNAS*, 46:253-257, February 1960.

X. Chen, G. Fossati, E. P. Liang, and M. Böttcher. X-ray Time Lags in TeV Blazars. *JAp&A*, 32:185-188, June 2011.

X. Chen, G. Fossati, E. P. Liang, and M. Böttcher. Time-dependent simulations of multiwavelength variability of the blazar Mrk 421 with a Monte Carlo multizone code. *MNRAS*, 416:2368-2387, September 2011.

X. Chen. Understanding the Nature of Blazars High Energy Emission with Time Dependent Multi-zone Modeling. Ph.D. Dissertation, Rice University, 2012.

C. C. Cheung, D. E. Harris, and L. Stawarz. Superluminal Radio Features in the M87 Jet and the Site of Flaring TeV Gamma-Ray Emission. *ApJ*, 663:L65-L68, July 2007.

S. W. Davis, J. M. Stone, and M. E. Pessah. Sustained Magnetorotational Turbulence in Local Simulations of Stratified Disks with Zero Net Magnetic Flux. *ApJ*, 713:52-65, April 2010.

D. S. De Young and W. I. Axford. *Nature*, 216:129, 1967

C. D. Dermer and E. P. Liang. Electron thermalization and heating in relativistic plasmas. *ApJ*, 339:512-528, April 1989.

V. Despringre, D. Fraix-Burnet, and E. Davoust. First millimeter mapping of the jet and nucleus of M 87. *A&A*, 309:375-380, May 1996.

J. Dexter, E. Agol, and P. C. Fragile. Millimeter Flares and VLBI Visibilities from Relativistic Simulations of Magnetized Accretion Onto the Galactic Center Black Hole. *ApJ*, 703:L142-L146, October 2009.

J. Dexter, E. Agol, P. C. Fragile, and J. C. McKinney. The Submillimeter Bump in Sgr A* from Relativistic MHD Simulations. *ApJ*, 713:1092-1104, July 2010.

J. Dexter, J. C. McKinney, and E. Agol. The size of the jet launching region in M87. *MNRAS*, 421:1517-1528, April 2012.

T. Di Matteo, S. W. Allen, A. C. Fabian, A. S. Wilson, and A. J. Young. Accretion onto the Supermassive Black Hole in M87. *ApJ*, 582:133-140, January 2003.

K. Dodds-Eden et al. Evidence for X-Ray Synchrotron Emission from Simultaneous Mid-Infrared to X-Ray Observations of a Strong Sgr A* Flare. *ApJ*, 698:676-692, June 2009.

A. Eckart, F. K. Baganoff, M. Morris, M. W. Bautz, W. N. Brandt, G. P. Garmire, R. Genzel, T. Ott, G. R. Ricker, C. Straubmeier, T. Viehmann, R. Schödel, G. C. Bower, and J. E. Goldston. First simultaneous NIR/X-ray detection of a flare from Sgr A*. *A&A*, 427:1-11, November 2004.

A. Eckart, F. K. Baganoff, R. Schödel, M. Morris, R. Genzel, G. C. Bower, D. Marrone, J. M. Moran, T. Viehmann, M. W. Bautz, W. N. Brandt, G. P. Garmire, T. Ott, S. Trippe, G. R. Ricker, C. Straubmeier, D. A. Roberts, F. Yusef-Zadeh, J. H. Zhao, and R. Rao. The flare activity of Satittarius A*. New coordinated mm to X-ray observations. *A&A*, 450:535-555, May 2006.

R. A. Edelson and M. A. Malkan. Far-infrared variability in active galactic nuclei. *ApJ*, 323:516-535, December 1987.

E. A. Fath. The spectra of some spiral nebulae and globular star clusters. *Lick Observatory bulletin*, 149:71-77, January 1909.

J. D. Finke. Monte Carlo/Fokker-Planck Simulations of Accretion Phenomena and Optical Spectra of BL Lacertae Objects. Ph.D. Dissertation, Athens, Ohio, Ohio University, August 2007.

J. D. Finke and M. Böttcher. A Library of Fokker-Planck Coefficients for Coulomb Scattering. *PASP*, 117:483-484, May 2005.

J. D. Finke and M. Böttcher. X-Ray Spectral Signatures of the Photon Bubble Model

for Ultraluminous X-Ray Sources. *ApJ*, 667:395-403, 2007.

V. Fish and S. Doeleman. Imaging the Very High Energy Emitting Region in M87. *38th COSPAR Scientific Assembly*, Bremen, Germany, p. 3, 2010.

L. G. Fishbone and V. Moncrief. Relativistic fluid disks in orbit around Kerr black holes. *ApJ*, 207:962-976, August 1976.

A. D. Fokker. Die mittlere Energie rotierender elektrischer Dipole im Strahlungsfeld. *Annalen der Physik*, 348:810-820, 1914.

K. Fricke. Stability of Rotating Stars II. The Influence of Toroidal and Poloidal Magnetic Fields. *A&A*, 1:388, April 1969.

H. Friedman and E. T. Byram. X-rays from Sources 3C 273 and M 87. *Science*, 158:257-259, October 1967.

C. F. Gammie, J. C. McKinney, and G. Toth. HARM: A Numerical Scheme for General Relativistic Magnetohydrodynamics. *ApJ*, 589:444-457, May 2003.

T. A. Gardiner and J. M. Stone. Energetics in MRI driven Turbulence. *AIP Conference Proceedings*, 784:475-588, September 2005.

K. Gebhardt and J. Thomas. The Black Hole Mass, Stellar Mass-to-Light Ratio, and Dark Halo in M87. *ApJ*, 700:1690-1701, August 2009.

A. M. Ghez, G. Duchêne, K. Matthews, S. D. Hornstein, A. Tanner, J. Larkin, M. Morris, E. E. Becklin, S. Salim, T. Kremenek, D. Thompson, B. T. Soifer, G. Neugebauer, and I. McLean. The First Measurement of Spectral Lines in a Short-Period Star Bound to the Galaxy's Central Black Hole: A Paradox of Youth. *ApJ*, 586:L127-L131, April 2003.

S. Gillessen, F. Eisenhauer, S. Trippe, T. Alexander, R. Genzel, F. Martins, and T. Ott. Monitoring Stellar Orbits Around the Massive Black Hole in the Galactic Center. *ApJ*, 692:1075-1109, February 2009.

J. Goldston, E. Quataert, and I. Igumenshchev. Synchrotron Radiation from Radiatively Inefficient Accretion Flow Simulations: Applications to Sagittarius A*. *ApJ*, 621:785-792, March 2005.

A. Goldwurm, B. Cordier, J. Paul, J. Ballet, L. Bouchet, J.-P. Reques, G. Vedrenne, P. Mandrou, R. Sunyaev, E. Churazov, M. Gilfanov, A. Finogenov, A. Vikhlinin, A. Dyachkov, N. Khavenson, and V. Kovtunenko. Possible evidence against a massive black hole at the Galactic Centre. *Nature*, 371:589-591, October 1994.

J. L. Greenstein and T. A. Matthews. Redshift of the Radio Source 3C 48. *AJ*, 68:280, 1963.

J. L. Greenstein and M. Schmidt. The Quasi-Stellar Radio Sources 3C 48 and 3C 273. *ApJ*, 140:1, July 1964.

J. L. Greenstein and M. Schmidt. The Two Absorption-Line Redshifts in Parkes 0237-23. *ApJ*, 148:L13, April 1967.

X. Guan, C. F. Gammie, J. B. Simon, and B. M. Johnson. Locality of MHD Turbulence in Isothermal Disks. *ApJ*, 684:1010-1018, April 2009.

H. Gursky, E. M. Kellogg, C. Leong, H. Tananbaum, and R. Giacconi. Detection of X-Rays from the Seyfert Galaxies NGC 1275 and NGC 4151 by the UHURU Satellite. *ApJ*, 165:L43, April 1971.

R. Hanbury Brown. The distribution and indentification of the sources. *Paris Symposium on Radio Astronomy*, ed. R. N. Bracewell. Stanford, California: Stanford University Press, p. 471, 1959.

R. Hanbury Brown, R. C. Jennison, and M. K. Das Gupta. Apparent Angular Sizes of Discrete Radio Sources: Observations at Jodrell Bank, Manchester. *Nature*, 170:1061-1063, December 1952.

P. Hardee. M87 and the Dynamics and Microphysics inside the Blazar Zone. *arXiv e-prints*, 1007.0426, July 2010.

D. E. Harris, C. C. Cheung, L. Stawarz, J. A. Biretta, and E. S. Perlman. Variability Timescales in the M87 Jet: Signatures of E^2 Losses, Discovery of a Quasi Period in HST-1, and the Site of TeV Flaring. *ApJ*, 699:305-314, July 2009.

J. F. Hawley. Global Magnetohydrodynamic Simulations of Cylindrical Keplerian Disks. *ApJ*, 554:534-547, June 2001.

J. F. Hawley and S. A. Balbus. The Dynamical Structure of Nonradiative Black Hole Accretion Flows. *ApJ*, 573:738-748, July 2002.

J. F. Hawley, C. F. Gammie, and S. A. Balbus. Local Three-dimensional Magnetohydrodynamic Simulations of Accretion Disks. *ApJ*, 440:742, February 1995.

C. Hazard, M. B. Mackey, and A. J. Shimmins. Investigation of the Radio Source 3C 273 by the Method of Lunar Occultatious. *Nature*, 197:1037-1039, March 1963.

G. L. Hilburn, E. P. Liang, S. Liu, and H. Li. Monte Carlo simulations of the broad-

band spectra of Sagittarius A* through the use of general relativistic magnetohydrodynamics. *MNRAS*, 401:1620-1627, January 2010.

G. L. Hilburn, E. P. Liang, S. Liu, and H. Li. General relativistic magnetohydrodynamic and Monte Carlo modeling of Sagittarius A*. *Ap&SS*, 336:145-149, November 2011.

G. L. Hilburn and E. P. Liang. Numerical Modeling of Multi-wavelength Spectra of M87 Core Emission. *ApJ*, 746:87, February 2012.

G. W. Hill. Researches in the Lunar Theory. *American Journal of Mathematics*, 1:5-26, 1878.

L. C. Ho. The Spectral Energy Distributions of Low-Luminosity Active Galactic Nuclei. *ApJ*, 516:672-682, May 1999.

F. Hoyle, G. R. Burbidge, and W. L. W. Sargent. On the Nature of the Quasi-Stellar Sources. *Nature*, 209:751-753, February 1966.

F. Hoyle and W. Fowler. On the nature of strong radio sources. *MNRAS*, 125:169, 1963.

F. Hoyle and W. Fowler. Nature of Strong Radio Sources. *Nature*, 197:533-535, February 1963.

E. P. Hubble. Extragalactic nebulae. *ApJ*, 64:321-369, December 1926.

S. Ichimaru. Bimodal behavior of accretion disks - Theory and application to Cygnus X-1 transitions. *ApJ*, 214:840-855, June 1977.

I. V. Igumenshchev, R. Narayan, and M. A. Abramowicz. Three-dimensional Magnetohydrodynamic Simulations of Radiatively Inefficient Accretion Flows. *ApJ*, 592:1042-1059, August 2003.

K. G. Jansky. Directional studies of atmospherics at high frequencies. *Proc. IRE*, 20:1920, 1932.

K. G. Jansky. Electrical disturbances apparently of extraterrestrial origin. *Proc. IRE*, 21:1387, 1933.

K. G. Jansky. A note on the source of interstellar interference. *Proc. IRE*, 23:1158, 1935.

R. C. Jennison and M. K. Das Gupta. Fine Structure of the Extra-terrestrial Radio

Source Cygnus I. *Nature*, 172:996, November 1953.

Y. Kato, S. Mineshige, and K. Shibata. Magnetohydrodynamic Accretion Flows: Formation of Magnetic Tower Jet and Subsequent Quasi-Steady State. *ApJ*, 605:307-320, April 2004.

E. Y. Khachikian and D. W. Weedman. An atlas of Seyfert galaxies. *ApJ*, 192:581-589, September 1974.

K. O. Kiepenheuer. Cosmic Rays as the Source of General Galactic Radio Emission. *Physical Review*, 79:738-739, August 1950.

D. E. Knuth. *Seminumerical Algorithms.* Addition Wesley, Reading, Massachusetts, 3rd edition, 1997.

J. H. Krolik. *Active Galactic Nuclei*, Princeton University Press, Princeton, New Jersey, 1999.

M. N. Lemaster and J. M. Stone. Dissipation and Heating in Supersonic Hydrodynamic and MHD Turbulence. *ApJ*, 691:1092-1108, February 2009.

A. Levinson and F. Rieger. Variable TeV Emission as a Manifestation of Jet Formation in M87? *ApJ*, 730:123, April 2011.

Y. Li, Y.-F. Yuan, J.-M. Wang, J.-C. Wang, and S. Zhang. Spins of Supermassive Black Holes in M87. II. Fully General Relativistic Calculations. *ApJ*, 699:513-524, July 2009.

E. P. Liang. Dissipation of Nonlinear Alfven Waves with Current Sheets in Relativistic Plasmas. *arXiv e-prints*, 0902.4740, February 2009.

E. P. Liang and C. D. Dermer. Interpretation of the gamma-ray bump from Cygnus X-1. *ApJ*, 325:L39-L42, February 1988.

S. Liu and F. Melia. New Constraints on the Nature of Radio Emission in Sagittarius A*. *ApJ*, 561:L77-L80, November 2001.

S. Liu, V. Petrosian, F. Melia, and C. L. Fryer. A Testable Stochastic Acceleration Model for Flares in Sagittarius A*. *ApJ*, 648:1020-1025, September 2006.

W. Liu, H. Li, L. Yin, B. Albright, K. Bowers, and E. P. Liang. Particle Energization in 3D Magnetic Reconnection of Relativistic Pair Plasmas. *Physics of Plasmas* 18:052105, May 2011.

D. Lynden-Bell. Galactic Nuclei as Collapsed Old Quasars. *Nature*, 223:690-694, August 1969.

S. Markoff, H. Falcke, F. Yuan, and P. L. Biermann. The Nature of the 10 kilosecond X-ray flare in Sgr A*. *A&A*, 379:L13-L16, November 2001.

N. Marshall, R. S. Warwick, and K. A. Pounds. The variability of X-ray emission from active galaxies. *MNRAS*, 194:987-1002, March 1981.

K. W. Martin, S. Liu, C. Fragile, C. Yu, and C. L. Fryer. Modeling Emission from the Supermassive Black Hole in the Galactic Center with GRMHD Simulations. *arXiv e-prints*, 0904.0118, April 2009.

T. A. Matthews, J. G. Bolton, J. L. Greenstein, G. Münch, and A. R. Sandage. *S&T*, 21:148, 1961.

S. Mei, J. P. Blakeslee, P. Côté, J. L. Tonry, M. J. West, L. Ferrarese, A. Jordán, E. W. Peng, A. Anthony, and D. Merritt. The ACS Virgo Cluster Survey. XIII. SBF Distance Catalog and the Three-dimensional Structure of the Virgo Cluster. *ApJ*, 655:144-162, January 2007.

F. Melia. *The Galactic Supermassive Black Hole*. Princeton University Press, Princeton, NJ, 2006.

M. Merck et al. Study of the spectral characteristics of unidentified galactic EGRET sources. Are they pulsar-like? *A&A Supp.*, 120:465-469, December 1996.

M. Moscibrodzka, C. F. Gammie, J. C. Dolence, H. Shiokawa, and P. K. Leung. Radiative Models of Sgr A* from GRMHD Simulations. *ApJ*, 706:497-507, November 2009.

M. Moscibrodzka, C. F. Gammie, J. C. Dolence, and H. Shiokawa. Pair Production in Low-luminosity Galactic Nuclei. *ApJ*, 735:9, July 2011.

M. Moscibrodzka, C. F. Gammie, J. C. Dolence, H. Shiokawa, and P. K. Leung. Numerical Models of Sgr A*. *ASPC*, 439:358, May 2011.

R. Narayan and I. Yi. Advection-dominated accretion: A self-similar solution. *ApJ*, 428:L13-L16, June 1994.

R. Narayan, I. Yi, and R. Mahadevan. Explaining the spectrum of Sagittarius A* with a model of an accreting black hole. *Nature*, 374:623-625, April 1995.

S. Nayakshin and F. Melia. Self-consistent Fokker-Planck Treatment of Particle Distributions in Astrophysical Plasmas. *ApJS*, 114:269, February 1998.

A. Neronov and F. Aharonian. Production of TeV Gamma Radiation in the Vicinity of the Supermassive Black Hole in the Giant Radio Galaxy M87. *ApJ*, 671:85-

96, December 2007.

S. C. Noble, C. F. Gammie, J. C. McKinney, and L. Del Zanna. Primitive Variable Solvers for Conservative General Relativistic Magnetohydrodynamics. *ApJ*, 641:626:637, April 2006.

S. C. Noble, P. K. Leung, C. F. Gammie, and L. G. Book. Simulating the emission and outflows from accretion discs. *CQG*, 24:S259-S274, June 2007.

M. L. Norman. Introducting ZEUS-MP: A 3D, Parallel, Multiphysics Code for Astrophysical Fluid Dynamics. *Astrophysical Plasmas: Codes, Models, and Observations*, Conference Proceedings, 9:66-71, May 2000.

K. Ohsuga, Y. Kato, and S. Mineshige. Spectral Properties of Three-dimensional Magnetohydrodynamic Accretion Flows. *ApJ*, 627:782-789, July 2005.

J. B. Oke. Absolute Energy Distribution in the Optical Spectrum of 3C 273. *Nature*, 197:1040-1041, March 1963.

D. E. Osterbrock and G. J. Ferland. *Astrophysics of Gaseous Nebulae and Active Galactic Nuclei*, University Science Books, Herndon, VA, September 2005.

E. S. Perlman, J. A. Biretta, W. B. Sparks, F. D. Macchetto, and J. P. Leahy. The Optical-Near-Infrared Spectrum of the M87 Jet from Hubble Space Telescope Observations. *ApJ*, 551:206-222, April 2001.

E. S. Perlman, D. E. Harris, J. A. Biretta, W. B. Sparks, and F. D. Macchetto. Month-Timescale Optical Variability in the M87 Jet. *ApJ*, 599:L65-L68, December 2003.

E. S. Perlman, R. E. Mason, C. Packham, N. A. Levenson, M. Elitzur, J. J. Schaefer, M. Imanishi, W. B. Sparks, and J. Radomski. The Mid-Infrared Emission of M87. *ApJ*, 663:808-815, July 2007.

B. M. Peterson. *An Introduction to Active Galactic Nuclei*, Cambridge University Press, Cambridge, NY, February 1997.

V. Petrosian. Synchrotron emissivity from mildly relativistic particles. *ApJ*, 251:727-738, December 1981.

M. Planck. Über einen Satz der statistichen Dynamik und eine Erweiterung in der Quantumtheorie. *Sitzungberichte der Preussischen Akadademie der Wissenschaften*, 24:324-341, May 1917.

L. A. Pozdnyakov, I. M. Sobol, and R. A. Syunyaev. Comptonization and the shaping of X-ray source spectra - Monte Carlo calculations. *ASPR*, 2:189-331, 1983.

W. Press, S. Teukolsky, W. Vetterling, and B. Flannery. *Numerical Recipes in Fortran*. Cambridge University Press, Cambridge, 2nd edition, 2001.

G. Reber. *Proc. IRE*, 28:68, 1940.

G. Reber. Notes: Cosmic Static. *ApJ*, 91:621-624, June 1940.

G. Reber. Cosmic Static. *ApJ*, 100:279, November 1944.

M. J. Rees. Black Hole Models for Active Galactic Nuclei. *ARA&A*, 22:471-506, 1984.

M. J. Rees, M. C. Begelman, R. D. Blandford, and E. S. Phinney. Ion-supported tori and the origin of radio jets. *Nature*, 295:17-21, January 1982.

O. Regev and O. M. Umurhan. On the viability of the shearing box approximation for numerical studies of MHD turbulence in accretion disks. *A&A*, 481:21-32, April 2008.

F. Rieger and F. Aharonian. Particle Acceleration Close to the Supermassive Black Hole Horizon: the Case of M87. *IJMPD*, 17:1569-1575, 2008.

A. E. E. Rogers, S. Doeleman, M. C. H. Melvyn, G. C. Bower, D. C. Backer, S. Padin, J. A. Philips, D. T. Emerson, L. Greenhill, J. M. Moran, and K. I. Kellermann. Small-scale structure and position of Sagittarius A(*) from VLBI at 3 millimeter wavelength. *ApJ*, 434:L59-L62, October 1994.

M. Rowan-Robinson. On the unity of activity in galaxies. *ApJ*, 213:635-647, May 1977.

G. B. Rybicki and A. P. Lightman. *Radiative Processes in Astrophysics*. Wiley-Interscience, New York, 1979.

M. Ryle, F. G. Smith, and B. Elsmore. A preliminary survey of the radio stars in the Northern Hemisphere. *MNRAS*, 110:508, 1950.

E. E. Salpeter. Accretion of Interstellar Matter by Massive Objects. *ApJ*, 140:796-800, August 1964.

A. R. Sandage. The Existence of a Major New Constituent of the Universe: the Quasistellar Galaxies. *ApJ*, 141:1560, May 1965.

M. Schmidt. 3C 273 : A Star-Like Object with Large Red-Shift. *Nature*, 197:1040, March 1963.

R. Schödel et al. A Star in a 15.2-year orbit around the supermassive black hole at the centre of the Milky Way. *Nature*, 419:694-696, October 2002.

C. K. Seyfert. Nuclear Emission in Spiral Nebulae. *ApJ*, 97:28, January 1943.

N. I. Shakura and R. A. Sunyaev. Black holes in binary systems. Observational appearance. *A&A*, 24:337-355, 1973.

R. Shcherbakov and F. Baganoff. Inflow-Outflow Model with Conduction and Self-consistent Feeding for Sgr A*. *ApJ*, 716:504-509, June 2010.

R. Shcherbakov and R. F. Penna. Constraining the Accretion Flow in Sgr A* by GR Dynamical and Radiative Modeling. *ASPC*, 439:372, May 2011.

G. A. Shields. A Brief History of Active Galactic Nuclei. *PASP*, 760:661-678, June 1999.

J. B. Simon, J. F. Hawley, and K. Beckwith. Simulations of Magnetorotational Turbulence with a Higher-Order Godunov Scheme. *ApJ*, 690:974-997, January 2009.

V. M. Slipher. The spectrum and velocity of the nebula N.G.C. 1068 (M 77). *Lowell Observatory Bulletin*, 1:59-62, 1917.

F. G. Smith. An Accurate Determination of the Positions of Four Radio Stars. *Nature*, 168:555, September 1951.

K. A. Sorathia, C. S. Reynolds, J. M. Stone, and K. Beckwith. Global Simulations of Accretion Disks. I. Convergence and Comparisons with Local Models. *ApJ*, 749:189, April 2012.

J. M. Stone and T. A. Gardiner. A New Godunov Scheme for MHD, with Application to the MRI in disks. *AIPC*, 784:16-26, September 2005.

J. M. Stone and T. A. Gardiner. Implementation of the Shearing Box Approximation in Athena. *ApJS*, 189:142-155, July 2010.

J. M. Stone, T. A. Gardiner, P. Teuben, J. F. Hawley, and J. B. Simon. Athena: A New Code for Astrophysical MHD. *ApJS*, 178:137-177, September 2008.

J. M. Stone, D. Mihalas, and M. L. Norman. ZEUS-2D: A radiation magnetohydrodynamics code for astrophysical flows in two space dimensions. III - The radiation hydrodynamic algorithms and tests. *ApJ*, 80:819-845, June 1992.

J. M. Stone and M. L. Norman. ZEUS-2D: A radiation magnetohydrodynamics code

for astrophysical flows in two space dimensions. I - The hydrodynamic algorithms and tests. *ApJ*, 80:753-790, June 1992.

J. M. Stone and M. L. Norman. ZEUS-2D: A radiation magnetohydrodynamics code for astrophysical flows in two space dimensions. II - The Magnetohydrodynamic Algorithms and Tests. *ApJ*, 80:791, June 1992.

H. Tananbaum, Y. Avni, G. Branduardi, M. Elvis, G. Fabbiano, E. Feigelson, R. Giacconi, J. P. Henry, J. P. Pye, A. Soltan, and G. Zamorani. X-ray studies of quasars with the Einstein Observatory. *ApJ*, 234:L9-L13, November 1979.

V. Trimble. The AGN paradigm: Historical highlights. *AIPC*, 254:647-656, May 1992.

C. M. Urry and P. Padovani. Unified Schemes for Radio-Loud Active Galactic Nuclei. *PASP*, 107:803, September 1995.

J.-M. Wang, Y.-R. Li, J.-C. Wang, and S. Zhang. Spins of the Supermassive Black Hole in M87: New Constraints from TeV Observations. *ApJ*, 676:L109-L112, April 2008.

A. S. Wilson and Y. Yang. Chandra X-Ray Imaging and Spectroscopy of the M87 Jet and Nucleus. *ApJ*, 568:133-140, March 2002.

M. C. H. Wright, R. Genzel, R. Güsten, and D. T. Jaffe. 86 GHz aperture synthesis observations of the Galactic center. *AIPC*, 155:133-137, April 1987.

Y.-D. Xu, R. Narayan, E. Quataert, F. Yuan, and F. K. Baganoff. Thermal X-Ray Iron Line Emission from the Galactic Center Black Hole Sagittarius A*. *ApJ*:640:319-326, March 2006.

F. Yuan. Advection-dominated Accretion: From Sgr A* to Other Low-luminosity AGNs. *ASPC*, 373:95, October 2007.

F. Yuan, E. Quataert, and R. Narayan. Nonthermal Electrons in Radiatively Inefficient Accretion Flow Models of Sagittarius A*. *ApJ*, 598:301-312, November 2003.

F. Yusef-Zadeh, M. Morris, and R. D. Ekers. New structures near the compact radio source at the Galactic Centre. *Nature*, 348:45-47, November 1990.

Y. B. Zel'Dovich. The Fate of a Star and the Evolution of Gravitational Energy Upon Accretion. *Soviet Physics Doklady*, 9:195, September 1964.

S. Zenitani and M. Hoshino. Relativistic Particle Acceleration in a Folded Current Sheet. *ApJ*, 618:L111-L114, January 2005.

S. Zenitani and M. Hoshino. Particle Acceleration and Magnetic Dissipation in Relativistic Current Sheet of Pair Plasmas. *ApJ*, 670:702-726, November 2007.

J. Zhao, R. D. Ekers, W. M. Goss, K. Y. Lo, and R. Narayan. Long-Term Variations of the Compact Radio Source SGR a at the Galactic Center. *IAUS*:136:535, 1989.